The Thesis Committee for Şeyma Keskin
Certifies that this is the approved version of the following thesis:

Conducting Metallopolymers with Tridentate Ligands and Coordination Chemistry with Corresponding Model Compounds

APPROVED BY
SUPERVISING COMMITTEE:

Supervisor:

Eric V. Anslyn

Ananth Dodabalapur

Conducting Metallopolymers with Tridentate Ligands and Coordination Chemistry with Corresponding Model Compounds

by

Şeyma Keskin, B.S., M.S.

Thesis

Presented to the Faculty of the Graduate School of

The University of Texas at Austin

in Partial Fulfillment

of the Requirements

for the Degree of

Master of Arts

The University of Texas at Austin

May 2013

Dedication

To my son,

For accompanying me during first nine months of his life in the chemistry laboratory.

Acknowledgements

I would like to express my sincere gratitude to Professor Eric V. Anslyn and Professor Ananth Dodabalapur as well as to Professor Jennifer S. Brodbelt and Professor Terry D. Kahn.

I would like to thank my co-workers for their help in my measurements: Michelle Mejia, Julie Wilkerson and Lauren Avery for X-ray crystallography, Sarah Stranahan (Willets research group) for Raman spectroscopy, Lauren Depue and Joe Rivers (Jones research group) for teaching me ATR-IR, Jeff McCarty (Jones research group) for teaching me Casa-XPS peak extrapolating technique and Nicholas Delone (Stevenson research group) for specular reflectance IR measurements.

I would like to thank my husband Tayfun Keskin as well as my parents, my sister and my brother for their never ending love, support, patience, understanding, and more importantly for their prayers. This work would not be possible without my family's support and sacrifice.

Abstract

Conducting Metallopolymers with Tridentate Ligands and Their Coordination Chemistry with Corresponding Model Complexes

Şeyma Keskin, M.A.

The University of Texas at Austin, 2013

Supervisor: Eric V. Anslyn

Conducting polymers that contain metals are remarkable materials, because they have the properties of both organic backbones and metals. Depending on the position of the metal relative to the conjugated backbone, i.e. attached to or directly in the backbone, these two can couple resulting in advancement of the functionality and therefore potential applications of these types of materials. Complexes of tridentate ligands with donor atoms such as phosphorus, nitrogen, and sulfur also have a wide variety of applications. In addition, complexes of tridentate ligands have advantages of stability and control of electron density by variation of donor atoms. Therefore, conjugated polymers with tridentate ligand units will have promise for various applications and advantages in their designs.

Complexes of PNP ligand with molybdenum and carbonyl ancillary ligands were synthesized and characterized. Isomerization and conversion reactions between them were investigated as well as the coordination modes. Many types of PNP ligands have

been studied in the literature because the hemilabile property of the nitrogen atom promotes some catalytic reactions and gives different coordination geometries.

Conducting polymers can be used as redox-active ligands and they can be used to control electron density on the metal attached to them. Synthesis and characterization of a novel polymerizable ligand 3,5-bis-EDOT-N,N-bis[2-diphenylphosphinoethyl]aniline was achieved. Related molybdenum complexes with ancillary ligands as carbonyls were also synthesized and characterized. Monomer complexes and the free ligand were electropolymerized and studied.

Tris(bipyridine)ruthenium(II) chloride and analogous complexes have been studied extensively in the literature due to their luminescent and photochemical properties, and excited state lifetimes. Conducting polymers with similar ruthenium groups have been investigated for various applications. Synthesis of four ruthenium complexes with the polymerizable ligand 2,6-Bis[4-[2-(3,4-diethylenedioxy)thiophene]pyrazol-1-yl]pyridine and four different bidentate ligands were reproduced; electropolymerizations of the complexes were achieved; electrochemical, UV-Vis and luminescence studies were performed and discussed.

Various complexes of copper, silver, platinum, and palladium with nitrogen and phosphorus donors have been reported for their luminescence behavior as well as their interesting structures. Model complexes of these metals with N,N-bis[2-(diphenylphosphino)ethyl]phenyl-amine (a PNP ligand) have been synthesized and characterized. Absorption and luminescence behaviors as well as the coordination modes were investigated.

Table of Contents

List of Tables xi

List of Figures xiii

List of Schemes xx

Chapter 1: Conducting Metallopolymers for Device Applications 1

Conducting Metallopolymers 1

Photoelectronic Devices. 5

Luminescence 7

Organic Light-Emitting Diodes (OLED) 11

Sensors 17

Electrocatalysis 20

Tridentate Ligands 21

Scope of Thesis 25

Chapter 2: Synthesis and Characterization of Molybdenum Carbonyl Complexes with Phosphorus/Nitrogen/Phosphorus Ligand as Bidentate and Tridentate Modes 28

Introduction 28

Experimental 31

Instrumentation 31

Spectroscopy 31

X-ray Crystal Structure Analysis 32

Synthesis 32

General Methods 32

Results and Discussion 39

Synthesis 39

Infrared and Raman Studies 42

Structure of the Complexes 43

Conclusions 57

Chapter 3: Polymerizable N,N-bis[2-(diphenylphosphino)ethyl]aniline Complexes of Molybdenum 58
Introduction 58
Experimental 65
Instrumentation 65
X-ray Crystal Structure Analysis 65
Electrochemistry 66
Synthesis 67
General Methods 67
Results And Discussion 76
Synthesis 76
Spectroscopic Properties of Monomer Complexes 77
Structure of Complex 15 78
Electrochemistry and Electropolymerization 81
Characterization of Polymers 86
Spectroscopic Properties of Polymers 89
Conclusions 90
Chapter 4: Polymerizable 2,6-bis(pyrazolyl)pyridine Complexes of Ruthenium 92
Introduction 92
Experimental 97
Instrumentation 97
Electrochemistry 97
Synthesis 98
General Methods 98
Results and Discussion 102
Synthesis 102
Electropolymerization of Ruthenium Complexes 103
UV-Visible Studies 107
Luminescence Studies 110
Conclusions 124

Chapter 5: Synthesis, Characterization, Coordination Chemistry, and Luminescence Studies of Copper, Silver, Palladium, and Platinum Complexes with a Phosphorus/Nitrogen/Phosphorus Ligand 125
Introduction 125
Experimental 130
Instrumentation 130
X-ray Crystal Structure Analysis 130
Synthesis 131
General Methods 131
Results and Discussion 138
Syntheses 138
NMR Studies of Complexes with Silver 145
Mass Spectrometry of Complexes 148
Crystal Structures of Complexes 148
UV-Vis and Luminescence Studies of Complexes and the Ligand 163
Conclusions 168
Appendix A: SNS Ligands 169
Syntheses 170
Crystal structures of SNS Ligands 42-44 172
Appendix B: Acknowledgements for the Measurements 174
References 179
Vita 190

List of Tables

Table 1. Crystal data and structure refinement for molybdenum complexes. 45

Table 2. Angles around O_h Mo atom and Mo-C-O for compound **4**.....52

Table 3. Angles around O_h Mo atom and Mo-C-O for compound **5**.....53

Table 4. Mo-C-O angles for compound **5**.....54

Table 5. Angles around O_h Mo atom and Mo-C-O for compound **6**.....54

Table 6. Bond lengths [Å] around Mo atom for compound **4**.....55

Table 7. Bond lengths [Å] around Mo atom for compound **5**.....55

Table 8. Bond lengths [Å] around Mo atom for compound **6**.....55

Table 9. Angles around O_h Mo atom for the compound *mer*-PNP-$MoCl_3$.[58] 56

Table 10. Bond lengths [Å] around Mo atom for compound *mer*-PNP-$MoCl_3$.[58] 56

Table 11. Crystal data and structure refinement of **15**.....79

Table 12. Selected bond lengths (Å) and angles (deg) of **15**. 80

Table 13. Photophysical data for the ruthenium complexes. 113

Table 14. Crystal data and structure refinement of platinum and palladium complexes. 156

Table 15. Crystal data and structure refinement of silver and copper complexes. 157

Table 16. Selected bond lengths (Å) and angles (deg) of **22**. 158

Table 17. Selected bond lengths (Å) and angles (deg) of **23**. 158

Table 18. Selected bond lengths (Å) and angles (deg) of **24**. 159

Table 19. Selected bond lengths (Å) and angles (deg) of **25**. 160

Table 20. Selected bond lengths (Å) and angles (deg) of **26**. 161

Table 21. Selected bond lengths (Å) and angles (deg) of **27**. 162

List of Figures

Figure 1. Structures of well-known conducting polymers. (Left to right) polyacetylene; poly(p-phenylene); polyphenylene vinylene; poly(3,4-ethylenedioxythiophene); polyaniline (X = NH/N) and polyphenylene sulfide (X = S); polypyrrole (X = NH) and polythiophene (X = S).....2

Figure 2. Initial steps in the electropolymerization of thiophenes. Illustration adapted from reference [2]. 3

Figure 3. Classification of metal incorporation into conducting polymers. Illustration adapted from reference [5]. 4

Figure 4. Examples of metal complexes incorporated into conjugated polymer systems for light-emitting diode applications.....6

Figure 5. Jablonski diagram showing the photophysical processes in a molecule. Diagram is adapted from reference [10].....9

Figure 6. Electronic transitions in transition metal complexes. 10

Figure 7. Set up of a typical OLED. Illustration is adapted from reference [12]. 13

Figure 8. Series of ligand substituted conjugated polymers for nitric oxide detection.... 19

Figure 9. Reversible metal-ion binding to rotaxane structure. 20

Figure 10. Palladium-containing conducting metallopolymer for electrocatalysis applications. 21

Figure 11. Cobalt-containing conducting metallopolymer for electrocatalysis applications. 21

Figure 12. Examples of the applications of complexes with tridentate ligands: a) catalysts, b) coordination polymer, c) solar cell material, d) chemosensor, e) biomimics. 22

Figure 13. Classes of tridentate ligands. a) crowns b) triskelions c) clamps d) ribbons.... 24

Figure 14. Structure and synthetic variability of pincer complexes. Illustration adapted from reference [49]. 25

Figure 15. Possible coordination geometries of PNP ligand: PNP – monomeric, PP – monomeric, PP – dimeric. Illustration adapted from reference [40]. 29

Figure 16. Coordination change by change in donor strength of hemilabile N. Illustration adapted from reference [62]..... 29

Figure 17. PNP-$Mo(CO)_n$, n = 3-4 complexes previously reported. Illustration adapted from references [63-65]..... 30

Figure 18. a) Solid state IR and Raman spectra of *fac*-PNP-$Mo(CO)_3$. b) Solid state IR and Raman spectra of *cis*-PNP-$Mo(CO)_4$..... 43

Figure 19. Crystal structure of *cis*-PNP-$Mo(CO)_4$ (**4**) showing the labeling of selected atoms. Hydrogen atoms have been omitted for clarity. Displacement ellipsoids are scaled to the 50% probability level..... 49

Figure 20. Crystal structure of *fac*-PNP-Mo(CO)$_3$ (**5**) showing the labeling of selected atoms. Hydrogen atoms have been omitted for clarity. Displacement ellipsoids are scaled to the 50% probability level. 50

Figure 21. Crystal structure of *mer*-PNP-Mo(CO)$_3$ (**6**) showing the labeling of selected atoms. Hydrogen atoms have been omitted for clarity. Displacement ellipsoids are scaled to the 50% probability level. 51

Figure 22. Molybdenum carbonyl containing polymers.[91, 96] 61

Figure 23. Change in electron density upon oxidation of the polymer. 64

Figure 24. a) ATR-IR spectra of the monomer complex **15**; b) ATR-IR spectra of the monomer complex **16**. 78

Figure 25. Crystal structure of the monomer complex **15** showing the labeling of selected atoms. Hydrogen atoms have been omitted for clarity. Displacement ellipsoids are scaled to the 50% probability level. 81

Figure 26. a) Polymerization profile b) scan rate dependence c) polymerization process for **poly-14**. 82

Figure 27. a) Polymerization profile b) scan rate dependence c) polymerization process for **poly-15**. 83

Figure 28. a) Polymerization profile b) scan rate dependence c) polymerization process for **poly-16**. 84

Figure 29. a) Polymerization profile b) scan rate of **poly-15** in a narrow window. 85

Figure 30. CV data of the model complex PNP-Mo(CO)$_3$. 86

Figure 31. High resolution XPS data (solid line) and peak fitting technique (dashed and dotted lines). a) **15** b) **16** c) **poly-15** d) **poly 16** e) attempt to make **poly 15** in $TBAClO_4$. 88

Figure 32. a) Molecular orbital diagram for $Ru(LL)_3^{2+}$ showing types of electronic transitions occurring b) detailed representation of the MLCT transition in D_3 symmetry. Diagram adapted from reference [53]. 93

Figure 33. Electropolymerization of a ruthenium-containing polymer in which the donor atoms are N. 95

Figure 34. Ruthenium-containing rod-like conducting polymer with bithiophene units... 95

Figure 35. Electropolymerization of ruthenium complexes, initial scans shown in red. Insets: Current vs. number of scans. a) **18** b) **19** c) **20** d) **21**. 106

Figure 36. Electrochemical scan rate dependance of a) **poly-20** b) **poly-21**. Insets: Current vs scan rate. 107

Figure 37. Molar extinction coefficient values vs wavelength for the complexes **18**, **19**, **20**, **21** and the ligand $EDOT_2NNN$. 108

Figure 38. Absorption spectrum of **poly-21** electropolymerized on ITO coated glass surface. 110

Figure 39. Excitation and emission spectra of the complexes a) **18**, b) **19**, c) **20**, d) **21** and $Ru(bpy)_3^{2+}$ as the standard in dry, air-free EtOH/MeOH (4:1) solution at RT and at 77 K in a quartz EPR tube. 116

Figure 40. Emission spectra of ^{3}MLCT phosphorescence of complexes **18** and **19** at RT and at 77 K in a dry, air-free EtOH/MeOH (4:1) solution in a quartz EPR tube. 118

Figure 41. Excitation and emission spectra of ^{3}MLCT phosphorescence of complex **20** and $Ru(bpy)_3^{2+}$ as the standard at RT and at 77 K in a dry, air-free EtOH/MeOH (4:1) solution in a quartz EPR tube. 118

Figure 42. Excitation and emission spectra of ^{3}MLCT phosphorescence of complex **21** and $Ru(bpy)_3^{2+}$ as the standard at RT and at 77 K in a dry, air-free EtOH/MeOH (4:1) solution in a quartz EPR tube. 119

Figure 43. Excitation and emission spectra of ^{3}MLCT phosphorescence of complex **20** and $Ru(bpy)_3^{2+}$ as the standard at RT in air-free and aerated EtOH/MeOH (4:1) solution in an airtight quartz cuvette. 120

Figure 44. Excitation and emission spectra of ^{3}MLCT phosphorescence of complex **21** at RT in air-free and aerated EtOH/MeOH (4:1) solution in an airtight quartz cuvette. 120

Figure 45. a) Emission spectrum of **poly-21** excited at 276 nm. b) Excitation (black) and emission spectra (red and blue) of **poly-21** in the visible region of the spectrum. 123

Figure 46. Binding modes of PNP ligand of the type $RN(CH_2CH_2PPh_2)_2$. 125

Figure 47. Examples of luminescent complexes of copper, silver, gold, platinum and palladium with phosphorus and nitrogen donating ligands. 127

Figure 48. $^{31}P\{^{1}H\}$ NMR spectra of a) **24** b) **25** taken at RT using a 300 MHz instrument. 146

Figure 49. $^{31}P\{^{1}H\}$ NMR spectra of **25** a) at RT b) at -40^{o}C c) at -80^{o}C taken by using a 500 MHz instrument. 147

Figure 50. View of a) **22** b) **23** showing the labeling of selected atoms. Hydrogen atoms have been omitted for clarity. Displacement ellipsoids are scaled to the 50% probability level. 152

Figure 51. View of a) **24** b) **25** showing the labeling of selected atoms. Hydrogen atoms have been omitted for clarity. Displacement ellipsoids are scaled to the 50% probability level. 153

Figure 52. View of **26** showing the labeling of selected atoms. Hydrogen atoms have been omitted for clarity. a) whole structure with two acetate groups b) only coordination environment with two acetate groups c) only coordination environment with one acetate and one chloride. Displacement ellipsoids are scaled to the 50% probability level. 154

Figure 53. View of **27** showing the labeling of selected atoms. Hydrogen atoms have been omitted for clarity. Displacement ellipsoids are scaled to the 50% probability level. 155

Figure 54. Absorption spectra of complexes **23**–**27**. 164

Figure 55. Excitation and emission spectra of ligand and metal complexes at RT. 165

Figure 56. Excitation and emission spectra of ligand and metal complexes at 77 K. . 166

Figure 57. Solid state excitation and emission spectra of **26**. 166

Figure 58. Excitation and emission spectra of ligand **3** in different solvents at RT (a-e). f) dielectric constant of the solvent vs wavelength of emission. 167

Figure A1. SNS ligands synthesized. 169

Figure A2. Structure of **42** showing the labeling of selected atoms. Hydrogen atoms have been omitted for clarity. Displacement ellipsoids are scaled to the 50% probability level. 172

Figure A3. Structure of **43** showing the labeling of selected atoms. Hydrogen atoms have been omitted for clarity. Displacement ellipsoids are scaled to the 50% probability level. 172

Figure A4. Structure of **44** showing the labeling of selected atoms. Hydrogen atoms have been omitted for clarity. Displacement ellipsoids are scaled to the 50% probability level. 173

List of Schemes

Scheme 1. Synthesis of the PNP pincer ligand.....40

Scheme 2. Synthesis of PNP-$Mo(CO)_n$ complexes and isomers.....41

Scheme 3. Reagents and conditions: a) i. $NaNO_2$, H_2SO_4, 0^oC, 2 hrs ii. $CuSO_4•5H_2O$, EtOH, reflux, 2hrs; b) $SnCl_2•2H_2O$, $NaBH_4$, EtOH, reflux, 30 min; c) Chloroacetylchloride, NEt_3, CH_2Cl_2, $0^oC \rightarrow RT$, 12 hrs; d) BH_3:THF, $0^oC \rightarrow RT$, 12 hrs; e) Chloroacetylchloride, NEt_3, CH_2Cl_2, $0^oC \rightarrow RT$, 12 hrs; f) BH_3:THF, $0^oC \rightarrow RT$, 12 hrs; g) 5-($SnBu_3$)-EDOT, $PdCl_2(PPh_3)_2$, DMF, 105^oC microwave, 45min; h) $KPPh_2$, THF, RT, 1 hr.....76

Scheme 4. Synthesis of $EDOT_2$PNP-$Mo(CO)_{3-4}$ complexes.....77

Scheme 5. Complex syntheses.....103

Scheme 6. Electropolymerization of $EDOT_2$NNN-Ru Complexes.....104

Scheme 7. Synthesis of silver, copper, platinum, and palladium complexes of PNP ligand. a) Pd_2dba_3, dry THF, RT, under N_2, 12 hrs; b) $(PhCN)_2PtCl_2$, dry benzene, reflux, under N_2, 1.5 hrs; c) $AgCF_3COO$, dry THF, RT, under N_2, 3hrs, dark; d) $AgCH_3COO$, dry THF, RT, under N_2, 3 hrs, dark; e) $Cu(CH_3COO)_2$, dry THF, reflux, under N_2, 3 hrs; f) $(PhCN)_2PdCl_2$, dry benzene, reflux, under N_2, 1 hr, or $PdCl_2$, dry CH_2Cl_2, RT, under N_2, 3 hrs. 140

Scheme 8. Proposed structures for iron (0) and ruthenium (0) complexes of **3**.....142

Scheme 9. Proposed structures for nickel (II) and ruthenium (II) complexes of **3**.....143

Scheme 10. Proposed structures for rhodium (I) and iridium (I) complexes of **3**..... 144

Chapter 1: Conducting Metallopolymers for Device Applications

CONDUCTING METALLOPOLYMERS

The discovery of conducting polymers dates back to 1970s. The intrinsically insulating organic polymer polyacetylene was reported to be conducting upon oxidation with chlorine, bromine, or iodine in 1977 by Shirakawa *et al.*[1] Discovery and development of conductive polymers were a major breakthrough, resulting in the awarding of the 2000 Nobel Prize in Chemistry to Alan J. Heeger, Alan G. MacDiarmid and Hideki Shirakawa. Since then, tremendous progress has been made in developing functional organic materials that conduct electricity.

Systems that are highly conjugated through π electrons are essential to conducting polymers. Polymers are intrinsically insulating, and the electrons in these delocalized orbitals have high mobility only when the material is "doped" through reaction with either oxidizing or reducing agents. Although the process is a redox reaction, it is often referred as “doping” in analogy with inorganic semiconductors. Adding electrons to the π system or removing them is relatively easy. Chemical or electrochemical doping produces charged species within the polymer backbone. The mobility of these charges defines the bulk conductivity of a given material. Oxidation removes some of these delocalized electrons and results in p-type doping. The radical cation formed is charge neutralized by the reduced form of the oxidizing agent. Thus, the conjugated p-orbitals form a one-dimensional electronic band, and the electrons within this band become mobile when it is partially emptied. On the other hand, n-type doping is achieved by reaction of the neutral polymer with a reducing agent. Common π-conjugated polymers are shown in **Figure 1**.

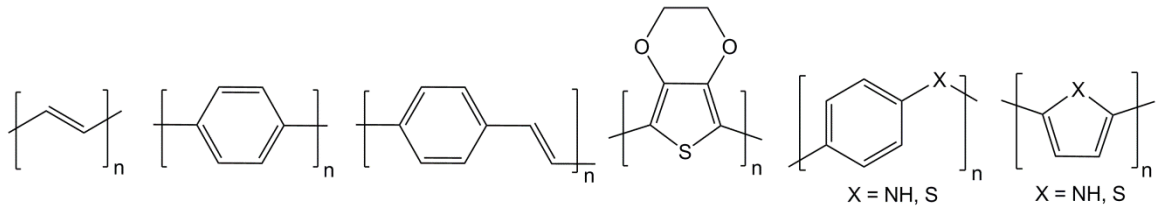

Figure 1. Structures of well-known conducting polymers. (Left to right) polyacetylene; poly(p-phenylene); polyphenylene vinylene; poly(3,4-ethylenedioxythiophene); polyaniline (X = NH/N) and polyphenylene sulfide (X = S); polypyrrole (X = NH) and polythiophene (X = S).

Conducting polymers can be synthesized either chemically or electrochemically. Electropolymerization is the technique that we use instead of chemical polymerization. This technique is convenient for bithiophene (BT) or 3,4-ethylenedioxythiphene (EDOT) groups and preferred, since there is no need to purify the polymer formed at the anode and there are no byproducts. Furthermore, the thickness of the film can be controlled by varying either the potential or the current during the electropolymerization process. An applied potential electrochemically oxidizes thiophene sites and forms radical cations, which couple to form a dication dimer that subsequently becomes a neutral dimer through the loss of two protons. This process continues until a polymer is deposited at the anode (**Figure 2**).[2] After polymerization, abstraction of electrons from the polymer backbone by electrochemical techniques results in a p-doped (or positively charged) semiconductor.

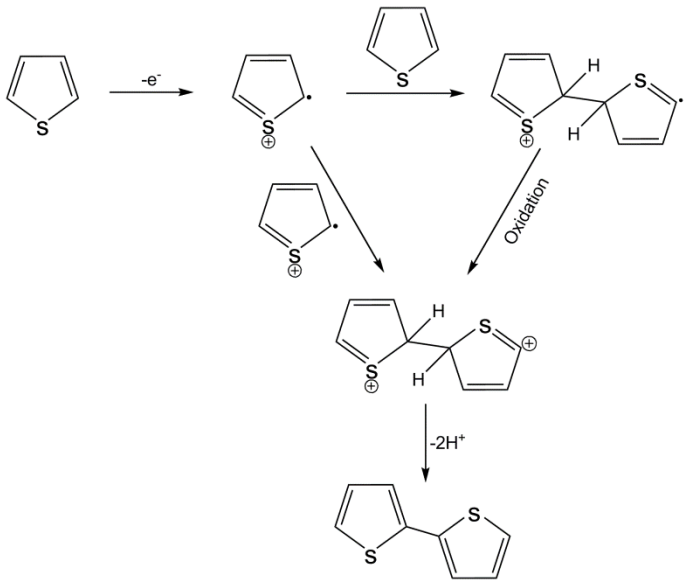

Figure 2. Initial steps in the electropolymerization of thiophenes. Illustration adapted from reference [2].

The incorporation of transition metals either attached to or directly in a π-conjugated polymer backbone has the potential to greatly increase the function and applications of conducting polymer systems.[3] Conducting metallopolymers are of particular interest since they allow having both properties of metal complexes and the organic polymers. The polymer films that can be deposited on specific locations are suitable for applications such as chemical sensors, electroluminescent devices, electrocatalysis, batteries, and memory devices.[3,4]

Metals can be incorporated into conducting polymer systems in a variety of different architectures. Wolf has classified conducting metallopolymers into three groups according to the location of the metal relative to the polymer backbone.[5] Categorized as type I are polymers that have a metal tethered to the backbone by a link such as an alkyl group. Since the metal is not in electronic communication with the backbone, properties of the metal group are similar to those of the untethered complex. In type II conducting

metallopolymers, metal complexes are next to the polymer backbone. Therefore, it is possible to have an electronic interaction/coupling between the metal and the backbone. Type III conducting metallopolymers are obtained when the metal located directly in the conjugated backbone (**Figure 3**) and electronic coupling is expected to be high.

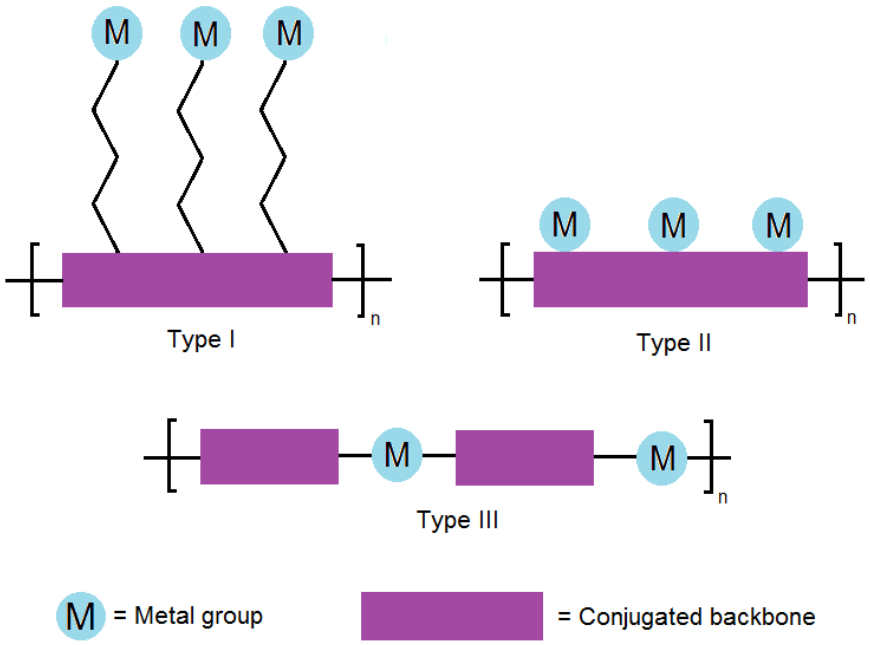

Figure 3. Classification of metal incorporation into conducting polymers. Illustration adapted from reference [5].

Two different redox conductivity mechanisms are observed in conducting metallopolymers: outer and inner sphere electron transfer mechanisms.[3] In the outer sphere mechanism, metal orbitals do not mix. On the contrary, in the inner sphere mechanism, two metal centers communicate by orbital overlap via a mutually bridging ligand. The rate of electron transfer by this mechanism depends on the nature of the bridging ligand and its orbital overlap with the two metal centers. In the outer sphere arrangement, there are redox-active metal centers or complexes that have no direct

interaction with the delocalized orbitals of the conducting organic polymer backbone and they can still provide important charge transfer mechanisms. Inner sphere architectures involve transition metal centers with strong coupling between the metal orbitals and the polymer strand. Additional charge transport pathways can be achieved when the energies of the orbitals are equivalent (same redox potential or redox matched) provided by strong coupling between the metal and the polymer. Highly conductive materials can therefore be obtained.

Conductivity is not the only interesting property in these materials. Electrochromism, electroluminescence, and high charge-carrier mobilities are some of the other useful properties of conducting metallopolymers.[6] These materials could therefore be used in energy harvesting devices such as solar cells or polymer-based light emitting devices. Properties of light-absorbing or emitting metal groups and high charge-carrier mobilities of the conjugated material may be combined, possibly resulting in enhanced device performance.[7] Consequently, the photophysics, specifically the singlet and triplet excited states of these materials, are of particular interest.

Photoelectronic Devices.

Many transition metal complexes have strong UV-Vis absorptions in charge transfer character such as, metal to ligand charge transfer (MLCT) or ligand to metal charge transfer (LMCT) that result in colorful emissions. When those metal complexes are incorporated in a π-conjugated system that has an efficient charge transfer, applications of these materials in photo electronic devices becomes very promising. Two examples from the literature are given in **Figure 4** for polymer light-emitting diode and photodetector applications. The first example uses an iridium complex. Zhang *et al.*

synthesized electrophosphorescent conjugated polyfluorenes (PFOPPyIr) based on (4,4'-dibromophenylpyridinato-*N,C* 2)bis(2-phenylpyridinato-*N,C* 2)iridium(III).[8] They reported a luminance efficiency of 3.80 cd/A and a luminance of 1248 cd/m^2. In the second example, an alternating layer-by-layer deposition of a conducting polymer that has ruthenium and SPAN has been made to create a photodetector. Functioning devices have exhibited short circuit currents and open circuit voltages in the 8.9–15.0 μA/cm^2 and 0.76–0.84 V ranges, under simulated solar illumination.[9]

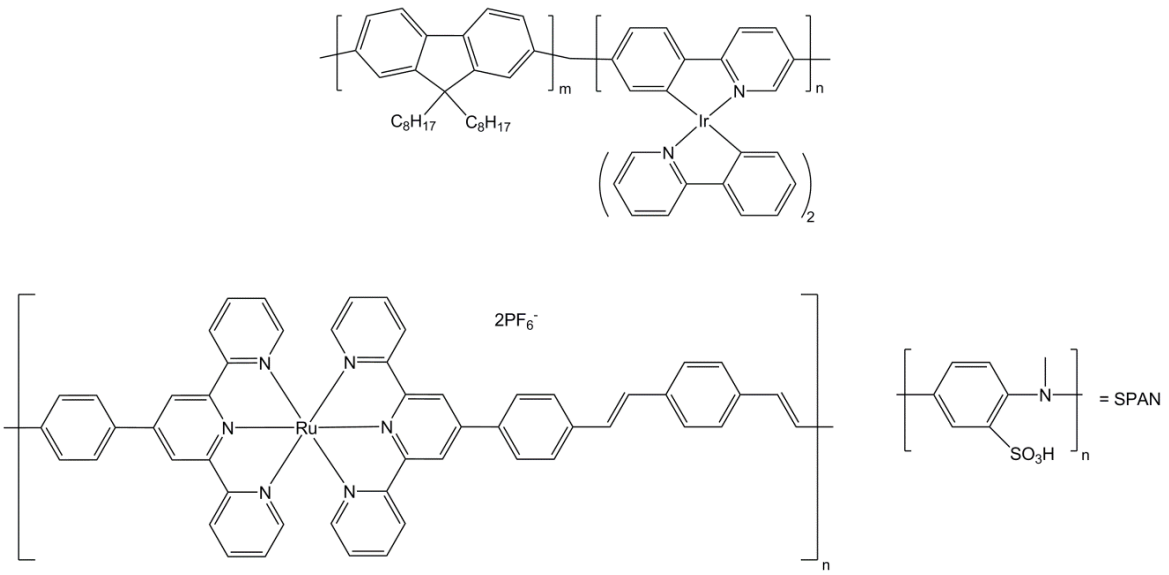

Figure 4. Examples of metal complexes incorporated into conjugated polymer systems for light-emitting diode applications.

Before designing such systems, one should know the luminescence properties of metal complexes and requirements for organic light-emitting diode materials.

Luminescence

Luminescence is a generic name for the emission of light from a substance whose electrons have been excited. It is a cold-body radiation and different from incandescence, which is the emission of light by a substance as a result of heating. Types of luminescence are named according to how the phenomenon is generated. For example, electroluminescence is the emission of light as a result of the flow of an electric current through a substance; photoluminescence occurs as a result of the excitation of an electron by irradiation of light; piezoluminescence is produced by the action of pressure on certain solids, etc.

Although there are various methods to induce excitation and subsequent emission, and therefore corresponding prefixes are used for luminescence, the generic term is sometimes used instead of photoluminescence. There are two forms of luminescence, which are fluorescence and phosphorescence. They differ both in spin state and in relaxation time. Fluorescence is a radiative relaxation of an electron from the singlet excited state to the singlet ground state and occurs on the order of nanoseconds, but phosphorescence is a radiative relaxation from a triplet excited state to a singlet ground state, with a lifetime on the order of microseconds. Because spin is not conserved in phosphorescence, it is a spin-forbidden transition, and relaxation takes longer than in fluorescence. When a molecule is said to be luminescent, no information about spin multiplicity is given.

A Jablonski diagram summarizes the photophysical processes that an electron can undergo in **Figure 5**.[10] Each column represents a specific spin multiplicity for a particular species. Within each column, horizontal lines represent the limits of electronic energy states (S_0, S_1, S_2…). Within each electronic energy state, there are multiple vibronic energy states. Each of these vibrational energy states can be subdivided even further into

rotational energy levels, but that level of detail has been omitted. As electronic energy states increase, the difference in energy decreases, eventually becoming a continuum.

The first transition is the absorption (A) of a photon. During absorption, the energy of the photon is transferred to a particular electron, resulting in the excitation of the electron to a higher energy level. The difference of energy levels corresponds to the energy of the photon and therefore to the wavelength of the light absorbed. Absorption generally occurs in ~ 10^{-15} seconds from the ground state since, as statistical mechanical calculations have shown, most electrons occupy the ground state at reasonable temperatures.

Once an electron is excited, there are different ways for it to return from the unstable excited state to the ground state.[10] Return processes can be referred to as relaxation, decay, or deactivation. If the relaxation is in the form of a photon, -in other words, if a photon is released-, then it is called emission or radiative relaxation, which can either be fluorescence (F) or phosphorescence (P), as described above. According to Kasha's rule, photon emission occurs in significant yield only from the lowest excited state of a given multiplicity.[11] So, an excited electron in a higher state relaxes to the first excited state before emitting light; even within the same excited state, the electron relaxes from the higher vibrational states to the ground vibrational state of an electronically excited state. Consequently, the emitted light has a lower energy than that of the absorbed light, and the emission wavelength is longer than the excitation wavelength. The difference between the positions of absorption and emission maxima is known as the Stokes shift.

Nonradiative decays happen through different mechanisms. Relaxation of an electron from the excited state to its lowest vibrational level is called vibrational relaxation, labeled VR in the diagram. In this process, energy dissipates from the

molecule to its surroundings; therefore, it does not occur in isolated molecules. A second type of nonradiative decay is internal conversion (IC), which occurs when an electron in the ground vibrational state of an electronically excited state passes into a high vibrational state of a lower electronic state without changing its spin. The third nonradiative process is called intersystem crossing (ISC), which occurs when an electron in the ground vibrational state of an electronically excited state passes into a high vibrational state of a lower electronic state in a different spin state. Intersystem crossing is most commonly observed in molecules with large spin-orbit coupling. This type of nonradiative transition leads to phosphorescence if the relaxation from T_1 to S_0 is radiative. The presence of a heavy metal atom especially facilitates high spin orbit coupling, in which case phosphorescence is observed.

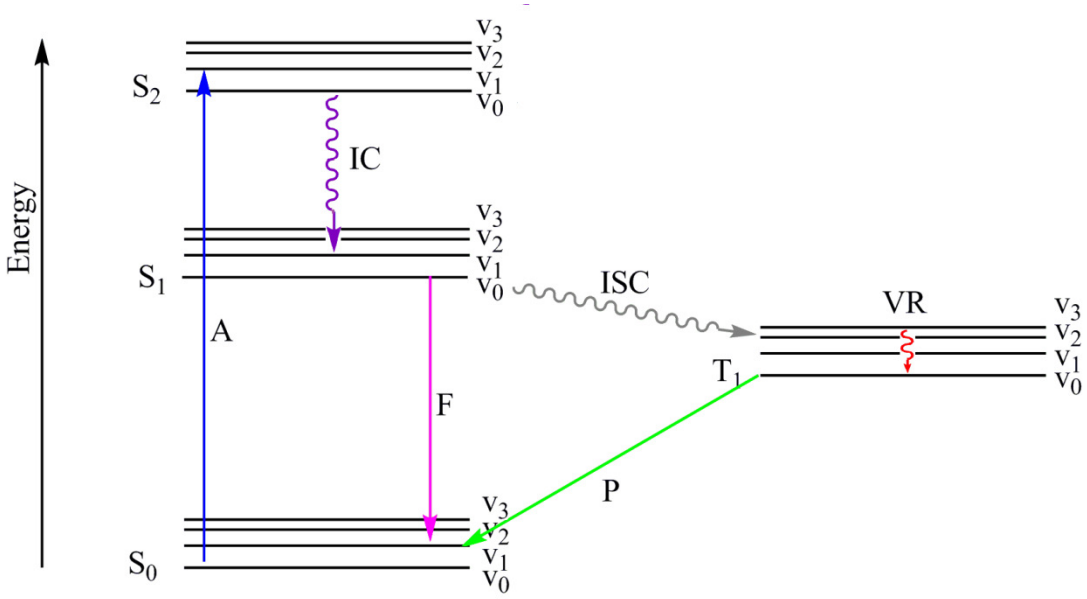

Figure 5. Jablonski diagram showing the photophysical processes in a molecule. Diagram is adapted from reference [10].

There are four types of electronic transitions in transition metal complexes. For all of these transitions, if the spin is conserved during emission, it is a fluorescence emission; if the spin changes, then the emission becomes phosphorescence (**Figure 6**).[12]

a) dd states (metal-centered (MC) transition): Metal d orbitals are split upon ligand coordination. Promotion of an electron within d orbitals results in excited dd states.

b) dπ* states (metal-to-ligand charge transfer (MLCT)): This transition is observed when an electron is promoted from a metal-centered d orbital to a ligand-centered π* antibonding orbital.

c) π, π* or n, π* states (intraligand (IL) transition): In this type of transition, electron is promoted from a bonding π or a nonbonding n orbital to an antibonding π* orbital. All are ligand-based orbitals.

d) πd states (ligand-to-metal charge transfer (LMCT)): This transition involves transfer of an electron from the ligand-based π orbital to a metal-based d orbital.

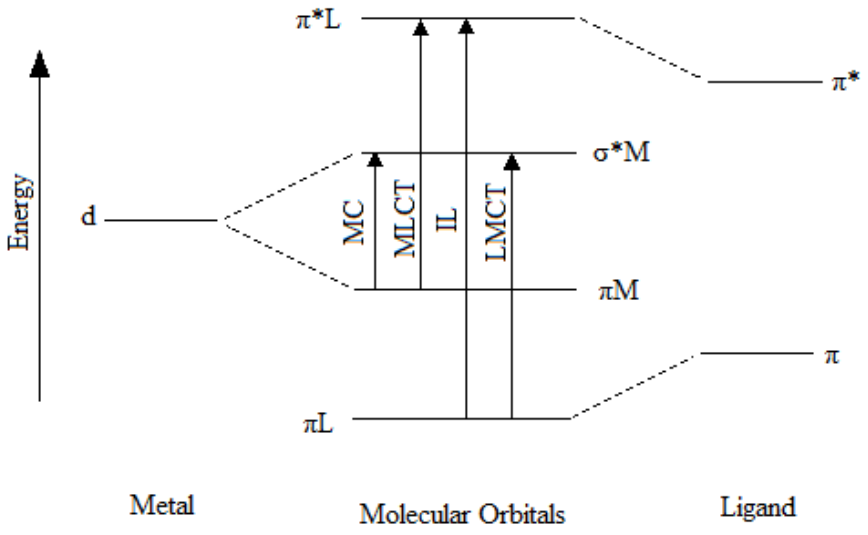

Figure 6. Electronic transitions in transition metal complexes.

The ordering of these four states depends on the metal, ligands, and geometry of the complex and can therefore be changed.[13] By a careful design of new complexes, the identity of the emitting state is predetermined for materials applications, especially in organic light emitting diodes, cell imaging, and photocatalysis.[13, 14]

Organic Light-Emitting Diodes (OLED)

After the first practical visible-spectrum LED (light-emitting diode) had been developed in 1962 by Nick Holonyak Jr. of General Electric, the first commercial LEDs were commonly used as replacements for incandescent and neon indicator lamps, and in seven-segment displays.[15] The commercial potential of OLEDs, in which the emissive electroluminescent layer is an organic-compound film that emits light in response to an electric current, was realized in 1987, when it was reported by Tang and VanSlyke of Kodak.[16]

OLEDs have many advantages over the existing technology both in solid state lighting and in displays. OLEDs illuminate a large area, since they constitute a surface light source; however, incandescent light bulbs and inorganic LEDs are point sources and illuminate small areas. Unlike in incandescent light bulbs, heat generation in OLEDs is minimal, making them energy efficient. The organic layers of an OLED are thinner, lighter, and more flexible than the crystalline layers in an LED or LCD (liquid crystalline display). OLEDs can be fabricated on flexible surfaces such as plastic, fabric, or clothing as well as on glass. Having flexible substrates, creates possibility of new applications, such as roll-up displays.[17] OLEDs generate light themselves, obviating the need for backlighting. For this reason, they consume much less power than LCDs. Reducing power consumption is especially important in battery operated devices, such as cell

phones. OLEDs can easily be produced in large thin films. Growing sufficient quantities of liquid crystals to make LCDs is difficult by comparison. For providing large viewing angle (about 170 degrees), brighter colors with higher contrast ratios, and faster response time and higher refresh rates, OLEDs are considered aesthetically superior to standard LCDs.

Although OLEDs have so many advantages over the existing technology, they do have some drawbacks, the most important one being a limited lifetime. Blue organics have considerably shorter lifetimes than red and green ones. That difference creates another problem, which is color balancing. Materials that produce blue light degrade more rapidly than the materials that produce green and red. Therefore, the color output of blue decreases, causing a change in the color balance of the display, which is more noticeable than a decrease in overall luminance. Efficiency of blue OLEDs are also low, reported as around 4 to 6%.[18] Cost is another drawback, as manufacturing processes are still expensive. Lastly, OLED displays are susceptible to water damage.

In a typical OLED device, thin organic films consisting of an electron-transport layer, an emissive layer, and a hole-transport layer are situated in between the anode, which is generally made up of transparent ITO (indium tin oxide), and the metallic cathode which uses a low work-function metal, such as magnesium, calcium, aluminum or lithium–aluminum (**Figure 7**).[12] During operation, the anode is positive with respect to the cathode. Under an applied electric field, electrons from the cathode are injected into the LUMO (lowest unoccupied molecular orbital) of the electron-transport layer, and electrons are withdrawn from the anode; in other words, holes from the anode are injected into the HOMO (highest occupied molecular orbital) of the hole-transport layer. Carriers are made to drift and approach each other by electrostatic forces. They finally meet in the emissive layer to form the exciton which is the bound state of an electron and

a hole. Both charges may arrive on a single molecule, or two molecules may form excited states. The radiative decay of this excited state results in the emission of light. The frequency of this radiation depends on the energy difference between the HOMO and LUMO levels of the emissive material.

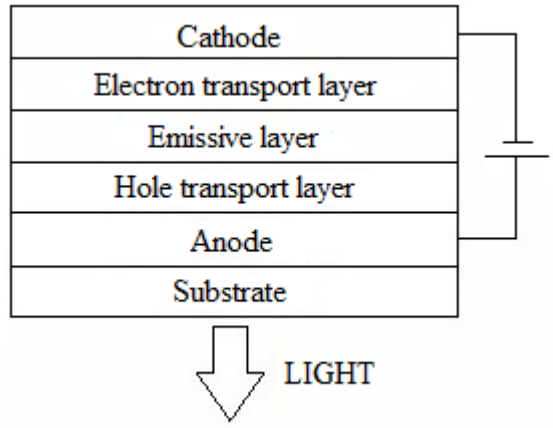

Figure 7. Set up of a typical OLED. Illustration is adapted from reference [12].

Theoretically, an OLED can function by having only an emissive layer between the electrodes.[19] In order to work efficiently by this configuration, the emissive layer should have a high quantum yield as well as, assist in the injection and transportation of charges. Fulfilling all of these requirements with a single material is difficult. Thus, single-layer OLEDs have poor efficiency and brightness.[20] OLEDs with a multilayer configuration, in which each layer fulfills a purpose, significantly improves the performance.[21]

The electron-transport layer (ETL) in OLEDs is used to remove electrons from the metal cathode and transport them. In addition, it plays a role in blocking holes. To serve as an efficient hole blocker, the material should have a wide band-gap energy with high ionization potential.[22] Furthermore, the cathodic reduction processes of ETL should

be reversible to form stable radical anions.[23] The ability to form homogeneous thin films with morphological and thermal stability is the other requirement for ETL materials. ETL materials contain electron-withdrawing groups on molecule. Heteroaromatic rings such as pyridine, triazine, 1,3,4-oxadiazole and benzothiadiazole are some examples of ETL materials.[22] Current examples include electron-withdrawing groups at the o-, m-, or p-positions of a centraltriphenylbenzene core, or at the 2,4,6-positions of a triazine or triphenyltriazine core to form nonplanar molecules.[24]

The hole-transport layer facilitates hole injection and transport from the anode into the emissive layer, as well as blocking escape of electrons from the emissive layer. Typical materials for HTL have low electron affinities and ionization potentials to promote electron removal, in addition to a reversible anode oxidation that yields a stable cationic radical.[22] The most impressive hole-transport materials are those with a truxene core consisting of three fluorenyl moieties fused together.[19]

There are two main classes of organic light emitting diodes: SMOLEDs (small-molecule based organic light-emitting diodes) and PLEDs (polymer light emitting diodes). PLEDs have advantages over the small molecule OLEDs, such as high charge carrier mobility, ease of fabrication, ability to cover a large area, and stability.[4,25]

Both singlet and triplet excitons are formed during electrical excitation. When an exciton is generated, there are four possible ways to combine the half integer spins of two charge carriers. Three of them are triplets; only one of them is a singlet state. As was mentioned in the previous section, fluorescence is the emission of light during relaxation from the singlet excited state to the singlet ground state; in other words, spin multiplicity does not change during the process. On the other hand, phosphorescence involves relaxation from the triplet excited state to the singlet ground state. The first OLED devices used fluorescent organic compounds.[12, 16] Devices using fluorescent materials

benefit only from singlet excitons and luminescence efficiency is limited. It has been found that luminous efficiency may be improved by a factor of four if phosphorescent materials are used as emitters. Although the decay of a triplet state is forbidden by the conservation of spin symmetry, complexes containing heavy metal atoms have spin orbit coupling, which mixes the singlet and triplet excited states, and both singlet and triplet states are utilized in emission; as a result, internal quantum efficiency is increased.

Efficient phosphorescence is rare at room temperature. In addition, few materials exhibit luminescence due to the quenching of emission by surrounding molecules. To solve the problem, luminescent materials are doped into the charge transport hosts.[16] There are three mechanisms for energy transfer from the host to the dopant molecule: Förster, Dexter, and charge trapping. Förster transfer[26] is a long-range (~ 40 – 100 Å), non-radiative, dipole-dipole coupling of donor (D) and acceptor (A) molecules. This mechanism transfers energy only to the singlet state of the acceptor molecule via:

$$^1D^* + {}^1A \rightarrow {}^1D + {}^1A^* \quad (1)$$

$$^3D^* + {}^1A \rightarrow {}^1D + {}^1A^* \quad (2)$$

Dexter transfer is a short-range process in which excitons diffuse from D to A sites via intermolecular electron exchange.[27] In contrast to Förster transfer, Dexter processes require only that the total spin of the D-A pair be conserved.

$$^1D^* + {}^1A \rightarrow {}^1D + {}^1A^* \quad (3)$$

$$^3D^* + {}^1A \rightarrow {}^1D + {}^3A^* \quad (4)$$

As a result, Dexter transfer permits both singlet-singlet and triplet-triplet transfers. Yet, due to the fact that Förster transfer is faster over long distances, it dominates singlet-singlet transfer at low acceptor concentrations. In charge trapping, the guest molecule traps the charge and generates an exciton by recombination with an opposite charge on a neighboring molecule.[28] The relative competition among these mechanisms of energy transfer depends on the lifetime of the exciton, its mobility within the film, and the thickness of the emissive film layer. For singlet–singlet modes, Förster energy transfer generally dominates, while all three mechanisms operate to some extent. Dexter and charge trapping mechanisms are the major modes for triplet exciton energy transfer, though all three energy transfer mechanisms are available.

External quantum efficiency $\Phi(ext)$ is one of the most important critical traits of OLEDs.[29] It is the ratio of the number of photons emitted through the glass substrate to the number of injected electrons. As shown in equation 1, the $\Phi(ext)$ is the product of the OLEDs' internal quantum efficiency $\Phi(int)$ and out-coupling efficiency ξ.

$$\Phi(ext) = \xi\, \Phi(int) \qquad (1)$$

Internal quantum efficiency is the fraction of excitons that create photons. It is a maximum of 0.25 for fluorescence and 1 for phosphorescence. It can also be described as the ratio of electrons and holes injected from the electrode (electron hole balance). In standard OLED architecture, the out-coupling efficiency is approximately 20%, due to the mismatch of refractive indices between the emissive layer, HTL, indium-tin oxide (ITO) anode, and the glass substrate.[30,31]

In order to obtain novel, high-quality triplet emitters for OLED applications, some requirements must be fulfilled. Emission wavelength (λem), lifetimes (τ), and quantum

yields (Φ) are all important. For full color displays, efficient OLEDs emitting the three primary colors, blue (~450–470 nm), green (~500–550 nm), and red (~650–700 nm), are required. As was mentioned above, blue emitters remain more challenging due to the large energy gap required between the excited triplet and ground states to obtain this emission wavelength. Long emission lifetimes are also a problem. They severely decrease the OLED saturation threshold. If a molecule remains in the triplet state for an extended period, conversion of electrical to photon energy is limited by inhibiting the rapid repopulation of excited states. The ideal phosphorescence lifetime has been reported in the region of 5–50 μs at 298 K.[12] Internal quantum efficiency should approach unity at 298 K. This is difficult to achieve, but to obtain any advantage over fluorescence emitters, internal quantum efficiency should be at least 0.25 at 298 K. In addition, suitable triplet emitters should ideally be stable under high operating temperatures and exhibit reversible redox behavior.

Sensors

In addition to the application in polymer based light emitting devices, metal complexes may be used to geometrically orient π-conjugated materials in specific three-dimensional arrangements in the solid state. Dramatic color shifts occur in response to changes in solvent, temperature, applied potential, and binding to other molecules. Both color changes and conductivity changes are induced by the same mechanism, which consists of twisting the polymer backbone and disrupting conjugation. This mutability makes conjugated polymers attractive as sensors that can provide a range of optical and electronic responses. The number of coplanar rings determines the conjugation length.

The longer the conjugation length, the lower the separation between adjacent energy levels, and the longer the absorption wavelength becomes.

Binding of an analyte will affect the redox potential of coordinatively unsaturated transition metals. Therefore, overlap of the metal and the conjugated polymer will also be affected, resulting in a measurable response in conductivity. The redox potential of the metal center and the conjugated polymer can match to a greater or lesser extent depending on the binding. If the redox potential of the metal and the conjugated polymer match perfectly, binding to the analyte will result in a poorer overlap, resulting in a very sensitive response exhibited as a severe decrease in conductivity. If the redox potential of the metal and the polymer display partial or no redox matching, then a single binding event can create a favorable redox matching that enhances local transport. The sensitivity of this case is best suited to the detection of target analytes at intermediate concentrations.[3]

Sensory systems based on conducting metallopolymers are given in the following examples. Smith *et al.* synthesized and studied families of conducting polymers, incorporating elements from the most studied conducting polymers in conjunction with bipyridyl or terpyridyl units for metal binding and nitric oxide detection (**Figure 8:** eight polymers: CP1a, CP1b, CP1c, CP2a, CP2b, CP2c, CP3b, CP3c).[32] They observed that the emission in the materials was quenched by 75-100% in the presence of Cu(II) ions. The quenching efficiency depends on the metal-ligating group and the identity of the spacer between these units. Main-chain bipyridyl binding units allow more efficient quenching than do minor side-chain terpyridyl units. Decreasing the electron-donating ability of spacers between binding units increases the quenching efficiency.

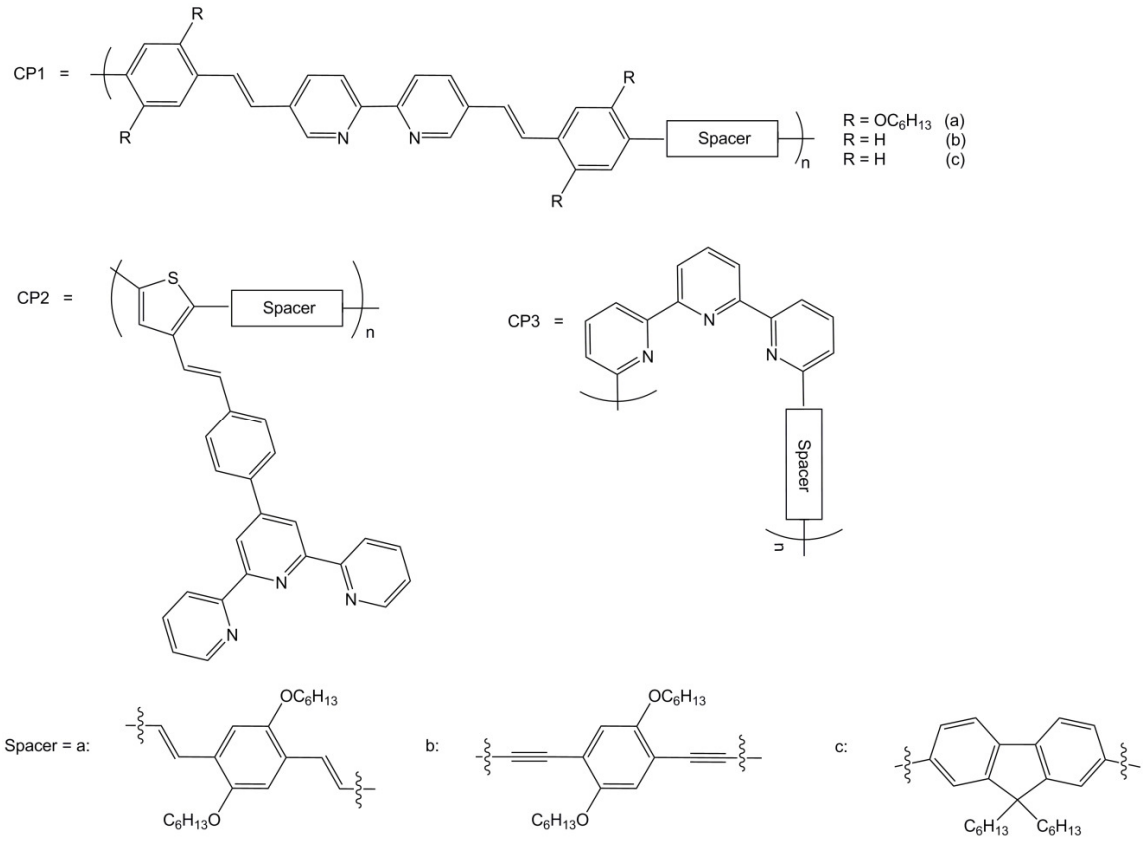

Figure 8. Series of ligand substituted conjugated polymers for nitric oxide detection.

Another example was reported by Zhu *et al.* The sensor is based on the polymetallorotaxane, which takes advantage of its reversible metal ion-binding rotaxane structure (**Figure 9**).[33] The materials display changes in both their optical and electrical properties with metal coordination. In particular, the addition of copper or zinc ions, gives a 34 nm red-shift in the UV-Vis spectrum from the metal-free polymer.

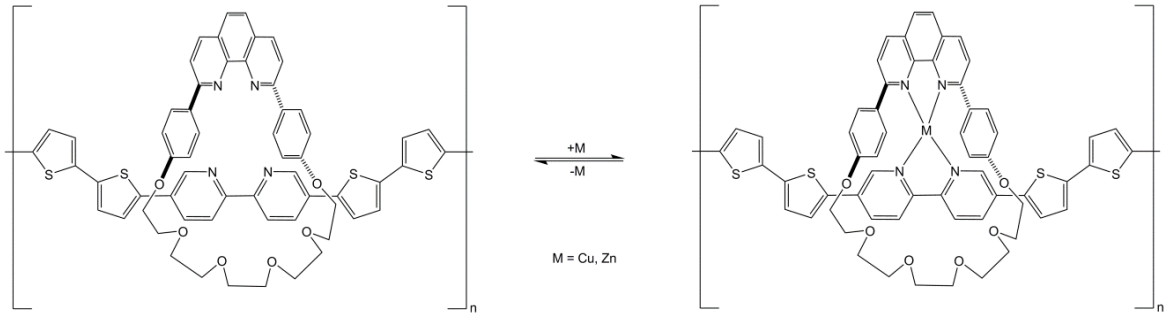

Figure 9. Reversible metal-ion binding to rotaxane structure.

Shioya and Holliday *et al.* also reported a cobalt-based salen polymer to detect nitric oxide both in solution and in the gas phase.[34, 35]

Electrocatalysis

Conducting polymers with coordinated transition metals have a potential use in catalysis: the reactivity of the catalyst can be tuned by applying a voltage, or the polymers can deliver multiple electrons to the reaction site. A recent example, a precursor to fabricate palladium nanoparticle (NP)/polymer hybrids for oxygen reduction, has been published.[36] First, an electropolymerizable palladium (II) metal complex was synthesized. Electropolymerization of the complex allowed for the Pd (II) metal centers to act as seed points for size-controlled palladium NP growth (**Figure 10**). A thin film of the polymer was exposed to a nitrogen-sparged mixture of $PdCl_2$ in water and a $Na_2CO_3/NaHCO_3$ buffer solution. Then, a nitrogen-sparged aqueous ascorbic acid solution was added to the vessel with the films and left to sit for a few minutes. The electropolymerized films were then removed from the nanoparticle growth solution and rinsed. The palladium nanoparticle/conducting metallopolymer hybrid material demonstrated electrocatalytic behavior toward oxygen reduction, with peak current densities around 400 μA/ cm^2 in acidic aqueous conditions.[36]

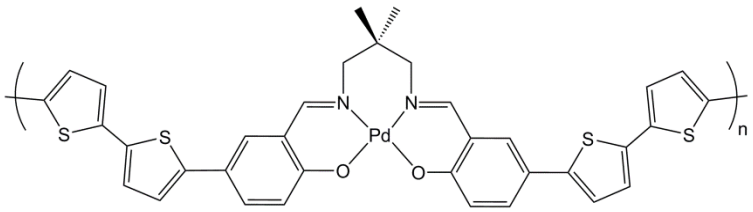

Figure 10. Palladium-containing conducting metallopolymer for electrocatalysis applications.

Another example is the four-electron reduction of oxygen to water electrocatalytically. The polymeric material has been shown to reduce oxygen to water efficiently, (**Figure 11**). The redox matching allows the rapid delivery of electrons to the cobalt and the complete conversion of the oxygen to water. Almost no trace of hydrogen peroxide formation was detected by rotating disk voltammetry.[37]

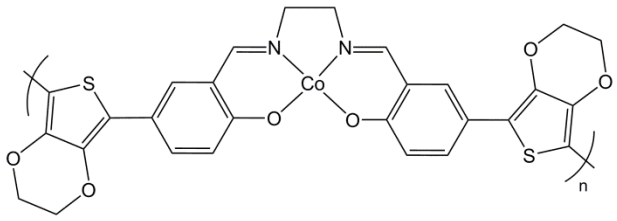

Figure 11. Cobalt-containing conducting metallopolymer for electrocatalysis applications.

TRIDENTATE LIGANDS

Complexes of tridentate ligands have a broad range of functionalization, which allows them to be tuned for specific application needs such as catalysis (hydroformylation, aldol condensation, reductive deamination and Heck arylation)[38,39], molecular materials (synthesis of oligomeric and polymeric coordination compounds,

light-emitting diodes and solar cells)[40,41], biomimics (active sites of metalloenzymes)[42,43] and chemosensors (Hg detection)[44] (**Figure 12**). Tridentate ligands provide enhanced stability to complexes, due to the well-known chelate effect. They can be used as a redox-active component and therefore can affect the binding of ancillary ligands.[45] These ligands can also be incorporated into polymer systems. Many types of tridentate ligands have been studied widely because the hemilabile property of the central atom promotes some catalytic reactions and gives different coordination geometries, such as tridentate monomeric, bidentate monomeric, and bidentate dimeric modes. Binding modes can be controlled by the strength of the central donor atom by having different R groups attached.[40]

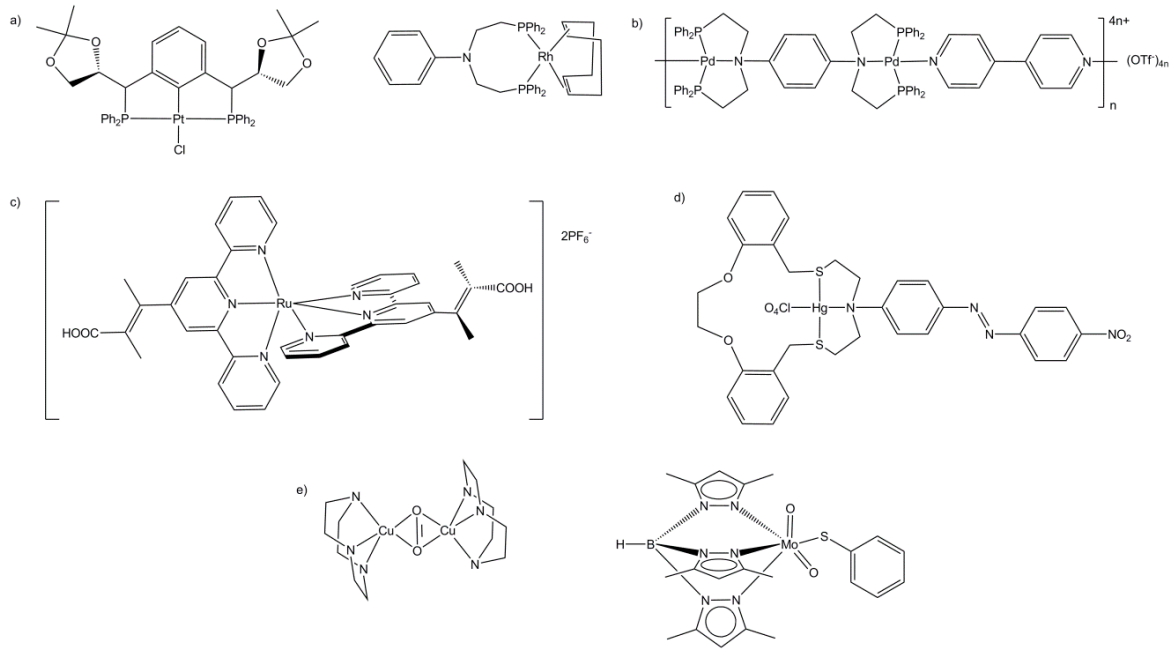

Figure 12. Examples of the applications of complexes with tridentate ligands:
a) catalysts, b) coordination polymer, c) solar cell material, d) chemosensor,
e) biomimics.

In octahedral complexes, tridentate ligands can occupy either two coplanar edges, in a *mer* conformation, or a face of the octahedron, in the *fac* conformation. It is obvious that some ligands coordinate in only one of the two modes (*fac* or *mer*), whereas others are flexible enough to adopt either type of coordination. Tridentate ligands are classified into four groups (**Figure 13**)[46]: (a) crown ligands such as triazacyclononane, in which the three donor atoms are held together by a cyclic system, and which can coordinate in a *fac* mode only; (b) triskelion ligands such as tris(pyrazolyl)borate (*triskelion* from the Greek *skelos*, leg: a symbolic figure of three legs or lines that comes from a common center), which have a larger flexibility than the crown ligands but cannot adopt to the *mer* conformation because of their radial topology; (c) clamp ligands, such as terpyridines, in which the three donor atoms are forced to be nearly coplanar and adopt only the *mer* coordination mode, and (d) open chain ligands or ribbons, such as diethylenetriamine, that are flexible enough to adopt to either the *fac* or the *mer* conformation. It should be noted that crown and triskelion ligands form three chelate rings upon complexation, whereas clamp and ribbon ligands form only two such rings.

The triskelion ligand tris(pyrazolyl)borate (Tp) known as a "scorpionate" ligand, was first reported by DuPont chemist Swiatoslaw Trofimenko in 1966.[47] The name scorpionate comes from the fact that the ligand can bind a metal with two donor sites, like the pincers of a scorpion, and the third donor site reaches over the plane to bind to the metal. The binding can be thought of as a scorpion grabbing the metal with two pincers before stinging it. Many different scorpionate ligands are known with a central atom different from boron and with different donor atoms. An additional specific class of tridentate ligands are called pincer ligands, a type of chelating agent that binds tightly to three adjacent coplanar sites, usually on a transition metal in a meridional configuration. Synthesis of pincer complexes dates back to 1970s. Shaw and Moulton reported on a

pincer–nickel compound with the nickel atom held in place by a monoanionic, terdentate PCP ligand.[48] Pincer ligands generally contain an *ortho*-disubstituted, monoanionic aryl ring (or corresponding alkyl chain). They are covalently bound via a central M–C σ bond to the metal center and two *ortho* substituents, each bearing a heteroatom E providing the tridentate bonding of the pincer ligand with two E–M dative bonds.[39] Pincer ligands are a subgroup of clamp ligands. The inflexibility of the pincer-metal interaction confers high thermal stability to the resulting complexes. The structure and synthetic variability of these ligands are shown in **Figure 14**.[49]

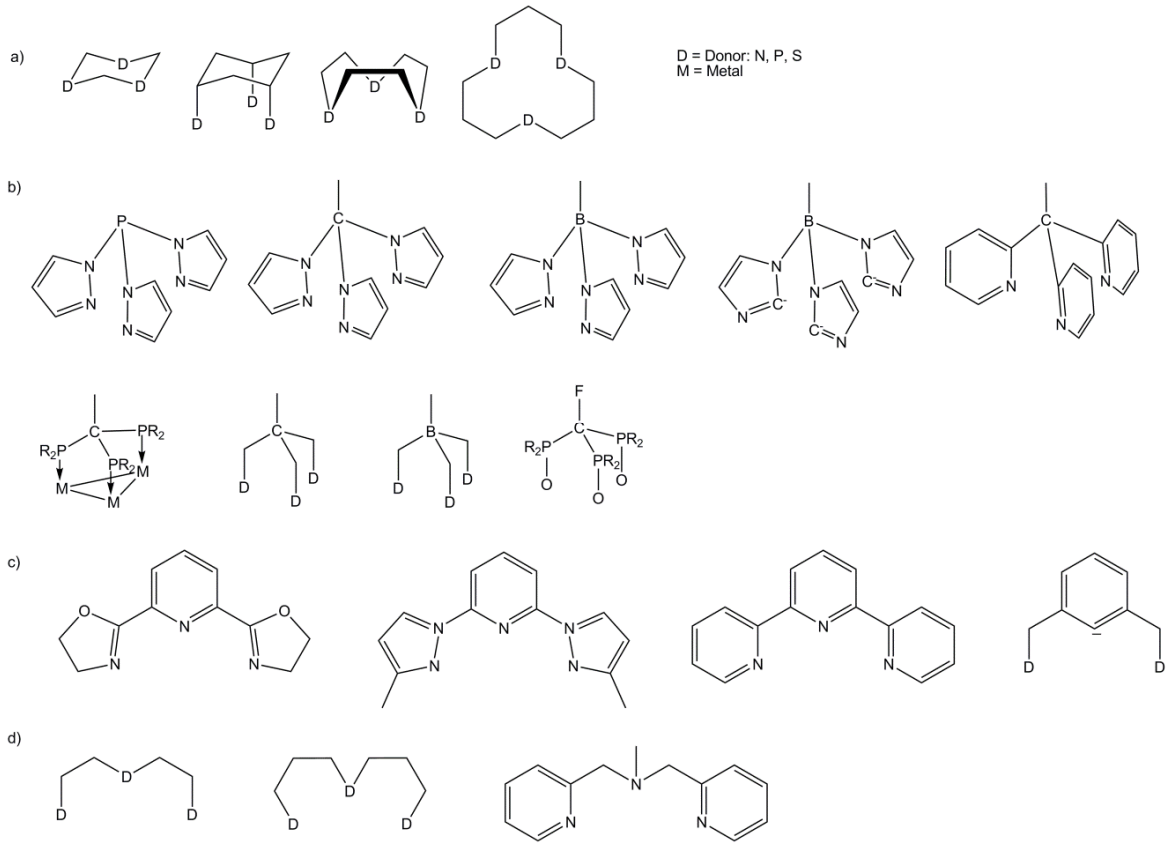

Figure 13. Classes of tridentate ligands. a) crowns b) triskelions c) clamps d) ribbons.

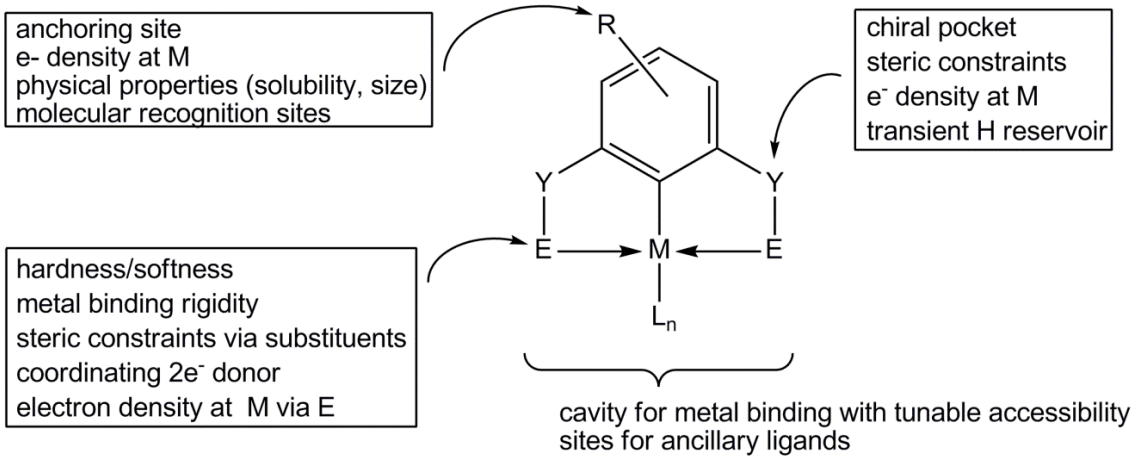

Figure 14. Structure and synthetic variability of pincer complexes. Illustration adapted from reference [49].

SCOPE OF THESIS

Several groups have reported conducting metallopolymers for various applications. For example, Wolf *et al.* coordinated transition metals to substituted thiophenes, thiophene-functionalized ferrocene and acetylides,[4, 5, 50] Swager *et al.* used bithiophene functionalized salen, crown ether, and bipyridine ligands.[33, 35, 37, 51] In addition, Reynolds *et al.* attached metal complexes to a polythiophene backbone.[52] A conducting polymer matrix itself can be a redox-active ligand due to available oxidation states. Transition metals also have multiple oxidation states and are therefore redox active. Electron density on the metal can be tuned by using redox-active conducting polymers as ligands. Also, electron density on the metal can be monitored by using ancillary ligands that can be detected spectroscopically, as in the examples of carbonyl, nitrosyl, and isocyanide detection in IR spectroscopy. Resulting polymer complexes are especially attractive for applications in sensing, and small-molecule storage and release.

Herein, is reported the design, synthesis, and characterization of novel electropolymerizable PNP ligand, which is a ribbon type tridentate ligand, and related to molybdenum complexes in two different coordination modes. Functionalization of the PNP ligand by EDOT groups allows for the electropolymerization of the complexes. Electron-donating ether groups of EDOT act to reduce the oxidation potential of the polymer. Metallopolymers are obtained by potentiodynamic anodic polymerization. Electropolymerization is the preferred technique due to its convenience, having no byproducts and no need for purification. Moreover, film thickness can be controlled. Another designing feature is the use of a ribbon-type PNP ligand, which allows flexible coordination modes, stable complexes by chelate effect, and ancillary ligands for the metal. Carbonyls are used as ancillary ligands both because they can be monitored spectroscopically and because commercially available metal carbonyls can readily be coordinated into the ligand; in addition, they are less expensive than nitric oxide gas for coordination.

$Ru(bpy)_3Cl_2$ has been one of the most widely studied molecules due to its unique properties, especially in luminescence emission and excited-state lifetimes.[53] There are various derivatives of $[Ru(bipy)_3]^{2+}$ in the literature for applications in biodiagnostics, photovoltaics, and organic light-emitting diodes, but no derivative has been commercialized.[54] Ruthenium(II) complexes are incorporated into the conjugated-polymer main chain, because of their promising luminescence properties for materials applications. Ruthenium-containing conjugated polymers reported in the literature are generally based on ligands in which nitrogen is the donor such as 2,2'-bipyridine (bpy), 1,10-phenanthroline (phen), 2,2',6',2"-terpyridine (terpy) and dipyridophenazine.[55, 56] In luminescent conducting metallopolymers, both the complex and the polymer can function

as independent light emitters[55] and conjugated polymers enhance charge carrier mobility.[4]

In this study, polymerizable 2,6-bis(pyrazol-1-yl)pyridines which is a clamp type tridentate ligand with three nitrogen donors were used. Here we report, electropolymerization/electrochemistry, absorption and luminescence measurements of 2,6-Bis[4-[2-(3,4-diethylenedioxy)thiophene]pyrazol-1-yl]pyridine-Ru(L')Cl complexes. The ligand is functionalized again by EDOT to be electropolymerized. Then two anionic and two neutral Ru(II) complexes were synthesized with the following ligands (L'): 1,1,1,5,5,5-hexafluoro-2,4-pentanedione (hfac), dibenzoylmethane (dbm), 2, 2'-bipyridine (bpy), 1,10-phenanthroline (phen). Further electropolymerization of the Ru complexes formed polymers in which the metal group was located directly in the conjugated backbone and strong electronic interactions between the organic bridge and metal group are possible. In addition, the conducting polymer should serve for better charge-carrier mobility. Such polymers have potential applications in OLED and photovoltaic devices.[57]

We sought to investigate the coordination chemistry, isomerization, and luminescence properties of model complexes with N,N-bis[2-(diphenylphosphino)ethyl]phenylamine, which is the PNP ligand without polymerizable groups. We synthesized and characterized molybdenum, silver, copper, platinum and palladium complexes of the ligand. In one part of the study, complexes of PNP with molybdenum, isomers and coordination modes were studied. Various complexes of copper, silver, gold platinum and palladium with nitrogen and phosphorous donors have been reported for their luminescence behavior as well as their interesting structures. In the other part of the study, PNP complexes of those metals were synthesized, characterized, absorption and luminescence properties were investigated.

Chapter 2: Synthesis and Characterization of Molybdenum Carbonyl Complexes with Phosphorus/Nitrogen/Phosphorus Ligand as Bidentate and Tridentate Modes.

INTRODUCTION

Molybdenum complexes with low oxidation states have been investigated extensively due to the role of these complexes in both chemical and biological nitrogen fixation.[58] There are more than fifty molybdenum-containing enzymes known, [59, 60] and the presence of molybdenum in these quantities is required by eukaryotes. [59] Molybdenum complexes also play important roles in organometallic chemistry. For example, molybdenum carbonyls have been used in Pauson–Khand reactions, i.e. [2+2+1] cycloaddition in which an alkene, an alkyne, and carbon monoxide combine to form a α,β-cyclopentenone. Pauson–Khand reactions are mediated both by bimetallic and monometallic transition metal complexes.[61] In addition, the coordination chemistry of molybdenum complexes has also been studied under thermal or photolytic conditions.

Many types of PNP (phosphorus/nitrogen/phosphorus) ligands have been studied widely because the hemilabile property of the nitrogen atom promotes some catalytic reactions and gives different coordination geometries, such as tridentate monomeric (PNP), bidentate monomeric (PP), and bidentate dimeric (PP) modes. Binding modes can be controlled through the donor strength of N by attaching different R groups to it.[40, 62] Examples of each binding mode are shown below.

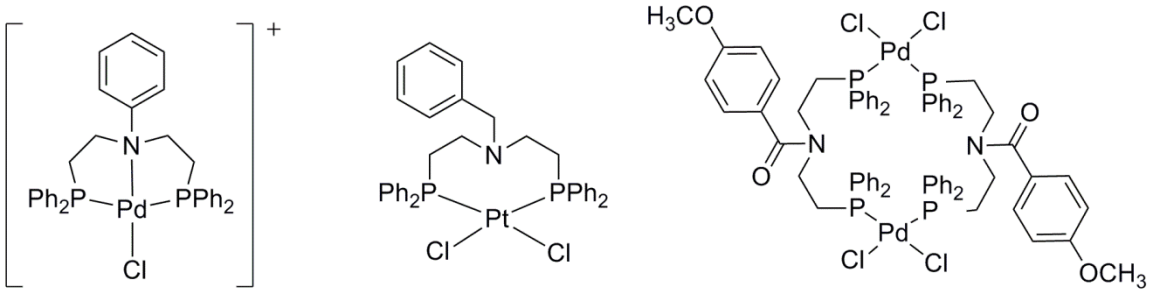

Figure 15. Possible coordination geometries of PNP ligand: PNP – monomeric, PP – monomeric, PP – dimeric. Illustration adapted from reference [40].

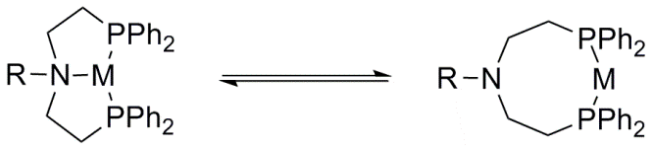

Figure 16. Coordination change by change in donor strength of hemilabile N. Illustration adapted from reference [62].

Previously, complexes of phosphorus/nitrogen/phosphorus (PNP) with molybdenum (PNP-$Mo(CO)_4$, *fac* and *mer* isomers of PNP-$Mo(CO)_3$) with different R groups on the nitrogen atom than our ligand were reported (**Figure 17**).[63-65] Crystal structures only for PNP-$Mo(CO)_4$ complexes (with different R groups on the N than in our complexes) were shown. Crystal structures for *fac* and *mer* isomers of PNP-$Mo(CO)_3$ have not been reported (with the ligand of the type: $(R_2PCH_2CH_2)_2NR$; R can either be a hydrogen atom or an alkyl group). In addition, O. P. Siclovan *et al.* reported that they synthesized and purified the *fac* isomer, but could not isolate the *mer* isomer.[63] They reported $^{31}P\{^1H\}$ NMR data very close to ours. However, only we have obtained the crystal structures for both isomers (and the tetracarbonyl complex). The choice of the *fac*

or *mer* isomer was explained by electronics rather than sterics in other literature papers.[58, 66]

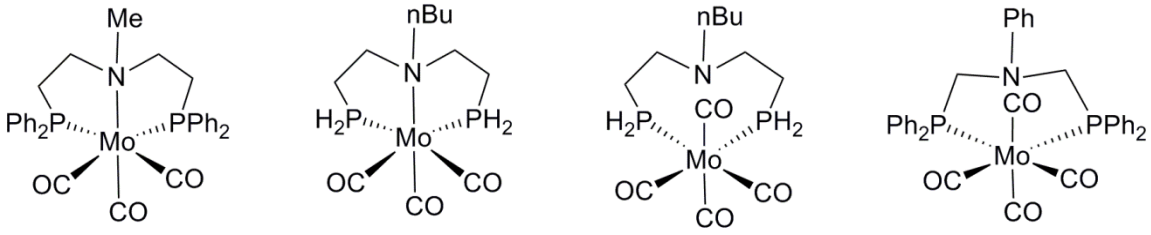

Figure 17. PNP-Mo(CO)$_n$, n = 3-4 complexes previously reported. Illustration adapted from references [63-65].

The title ligand N,N-bis[2-(diphenylphosphino)ethyl]phenylamine we used in our study was synthesized previously and coordinated to rhodium, palladium, and rhenium metals, but not to molybdenum or any other metals.[38, 62, 67]

In this study, molybdenum carbonyl complexes with the N,N-bis[2-(diphenylphosphino)ethyl]phenylamine ligand have been synthesized and characterized. Two isomers for PNP-Mo(CO)$_3$, i.e. *fac* and *mer* isomers, and one tetracarbonyl complex, *cis*-PNP-Mo(CO)$_4$, were obtained as well as their crystal structures. All three complexes are new compounds. Ligand binding modes and conversion among the three complexes have also been investigated.

EXPERIMENTAL

Instrumentation

NMR spectra were recorded with a Varian Unity + 300 spectrometer using a 5 mm auto-switchable probe ($^{1}H/^{19}F/^{13}C/^{31}P$). ^{1}H NMR signals were referenced to residual proton resonances in deuterated solvents. $^{13}C\{^{1}H\}$ NMR spectra were referenced relative to solvent peaks. $^{31}P\{^{1}H\}$ NMR spectra were referenced to a H_3PO_4 external standard. All peak positions are listed in ppm, and all coupling constants are listed in Hertz (Hz). Mass spectrometry was carried out using a Thermo Finnegan TSQ 700 spectrometer. Melting points were recorded on a Mel-Temp II melting temperature apparatus made by Laboratory Devices of Holliston, MA. Elemental analysis was performed by Quantitative Technologies Inc. (Whitehouse, NJ). Samples were freshly prepared prior to analysis.

Spectroscopy

IR spectra were recorded with a Nicolet Avatar 330 FT-IR spectrophotometer. Solid state IR measurements were obtained using an ATR accessory. Solution IR data was recorded using DCM solutions (~ 10^{-2} M).

Raman spectra were recorded with a Princeton Instruments Acton SpectraPro 2500i spectrophotometer, using epi-illumination through an X20 air objective in an Olympus IX-71 inverted microscope with 0.5 mW 532 nm excitation. Each spectrum is the average of 10 acquisitions, each with an exposure time of 5s. Samples were in the solid state on glass substrates.

X-ray Crystal Structure Analysis

The single-crystal diffraction data were collected on a Nonius Kappa CCD diffractometer using a graphite monochromator with MoKα radiation (λ = 0.71073Å) and an Oxford Cryostream low temperature device. Absorption corrections were applied using Multi-scan.[68] Data reductions were performed using DENZO-SMN.[69] The structure was solved by direct methods using SIR97[70] and refined by full-matrix least-squares on F2 with anisotropic displacement parameters for the non-H atoms using SHELXL-97.[71] The hydrogen atoms were calculated in ideal positions with isotropic displacement parameters set to 1.2xUeq of the attached atom (1.5xUeq for methyl hydrogen atoms). Neutral atom scattering factors and values used to calculate the linear absorption coefficient are from the International Tables for X-ray Crystallography (1992).[72]

Synthesis

General Methods

All chemicals were purchased from commercial suppliers and were used as received, except trimethylamine N-oxide dihydrate was purified by sublimation prior to use to remove the water of hydration.[73] Air- and moisture-sensitive reactions were carried out in oven-dried glassware using standard Schlenk techniques under an inert nitrogen atmosphere or in a glove box with an argon atmosphere. Dry solvents were obtained from an Innovative Technologies Pure-Solv 400 solvent purification system. The target ligand, N,N-bis[2-(diphenylphosphino)ethyl] benzenamine **3**, was prepared according to Kostas' method.[38] The synthesis of *cis*-PNP-Mo(CO)$_4$ **4** and *fac*-PNP-Mo(CO)$_3$ **5** were done using techniques similar to Blower's[74] and Ainscough's[75] techniques, respectively.

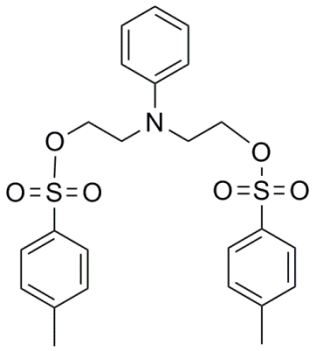

N,N-bis[2-(p-tolylsulfonyl)ethyl]aniline [1]. N-phenyldiethanolamine (2.7855 g, 15.37 mmol) was dissolved in dry pyridine and then cooled to 0°C. p-toluenesulfonylchloride (7.4134 g, 38.89 mmol) was also dissolved in dry pyridine separately and then added into the N-phenyldiethanolamine solution dropwise while stirring at 0°C. After complete addition, the mixture was allowed to warm to RT and stirred overnight. The reaction contents were poured into a rapidly stirred water/ice bath. The resulting precipitate was collected via vacuum filtration. The precipitate was then recrystallized using a hot mixture of toluene/ethanol (1:1) (crystallized at 0 °C). The white crystalline product was collected by filtration (75%, 5.6438 g, 11.53 mmol). ^{1}H NMR (300 MHz, $CDCl_3$): 7.69 (d, 4H, *J* = 8.4), 7.25 (d, 4H, *J* = 8.1), 7.11 (dd, 2H, *J* = 8.7), 6.68 (t, 1H, *J* = 8.1), 6.40 (d, 2H, *J* = 8.1), 4.06 (t, 4H, *J* = 6.0), 3.53 (t, 4H, *J* = 6.0), 2.40 (s, 6H). ^{1}H NMR, ^{13}C{^{1}H} NMR and ESI MS were previously reported.[38]

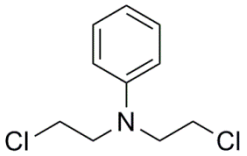

N,N-bis(2-chloroethyl)aniline [2]. N-Phenyldiethanolamine (0.5 g, 2.759 mmol) was dissolved in dry benzene and then cooled to 0°C. Phosphorus oxychloride (0.9 mL, 96.56 mmol) was added dropwise. When the addition was complete, the mixture was refluxed at 90 °C for 1 hr, then cooled to RT and stirred overnight. The reaction mixture

was poured into ice-water, stirred for 1 hr, and then the mixture was transferred into a separatory funnel. The aqueous phase was washed twice with benzene. Organic phases were combined, washed twice with brine, dried over $MgSO_4$, and vacuum filtered, and the filtrate was evaporated. The crude product was purified via column chromatography (silica gel). The eluent was a mixture of hexanes/CH_2Cl_2 (2:1). The first fraction was the product. The solvent was evaporated to obtain the pure product as yellowish oil (66 %, 0.399g, 1.829 mmol). ^{1}H NMR (300 MHz, $CDCl_3$): 7.34 (t, 2H, J = 7.5), 6.86 (t, 1H, J = 7.5), 6.76 (d, 2H, J = 8.7), 3.8–3.66 (m, 8H).

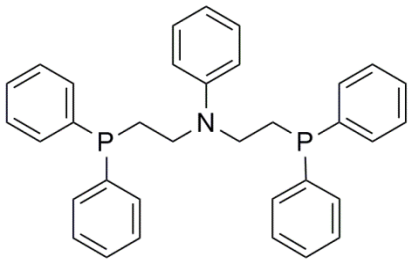

N,N-bis[2 -(diphenylphosphino)ethyl] –benzenamine (PNP) [3]. Ditosylate starting material **1** (2.058 g, 4.2 mmol), was dissolved in dry THF under nitrogen in a Schlenk flask. $KPPh_2$ (17.23 ml, 8.6 mmol, 0.5 M in THF) was added via a glass airtight syringe. The mixture was stirred for 2 hrs at RT and then quenched with ~3.4 mL of dry methanol and stirred for 30 minutes. The solvents were evaporated and the Schlenk flask was then transferred into the glove box. The residue was washed and suspended in toluene, and the washings were passed through a frit in which there were celite/silica gel/celite layers. The filtrate was evaporated to dryness. The residue was then washed with ether and dried again. An analytically pure product was recovered as white precipitate (1.9 g, 3.67 mmol, 88 %). ^{1}H NMR (300 MHz, CD_2Cl_2): 7.45–7.32 (m, 20H), 7.07 (t, 2H, J = 7.8), 6.60 (t, 1H, J = 6.6), 6.37 (d, 2H, J = 8.1) 3.35 (m, 4H), 2.29 (t, 4H,

J = 7.8). $^{31}P\{^{1}H\}$ NMR (121 MHz, CD_2Cl_2): -20 (s). ^{1}H NMR, $^{13}C\{^{1}H\}$ NMR and MS data were reported previously and matched with our data.[38]

Another approach to synthesizing the ligand, using N,N-bis(2-chloroethyl) aniline as the starting material instead of N,N-bis[2-(p-tolylsulfonyl)ethyl]aniline, was also employed, but resulted in a lower yield (~60%).

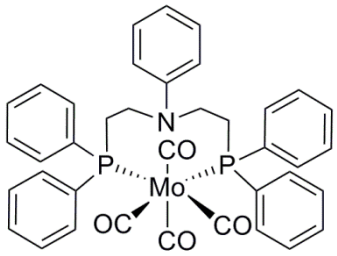

***cis*-PNP-Mo(CO)$_4$ [4].** $Mo(CO)_6$ (0.0963 g, 0.3648 mmol) was dissolved in acetonitrile (ACN) and refluxed under nitrogen for 1-2 hrs until a clear yellow solution was obtained. The ligand, **3**, (0.1879 g, 0.363 mmol) was dissolved in CH_2Cl_2 and then cannula-transferred into the metal solution. The mixture was stirred for 2 days in the dark. Removal of the solvent resulted in a yellow-gray solid, **4** as a crude product mixture. Hexanes were layered on a concentrated CH_2Cl_2 solution of **4** to obtain an X-ray diffraction quality single crystal. ^{1}H NMR (300 MHz, CD_2Cl_2): 6.5–7.6 (m, 25H), 3.34(m, 4H), 2.60 (m, 4H). $^{31}P\{^{1}H\}$ NMR (121 MHz, CD_2Cl_2): 25.6 (s). MS (ESI): calculated for *cis*-PNP-Mo(CO)$_4$ 727.09, found 727.5.

NBD-Mo(CO)$_4$ (0.087 g, 0.29 mmol) was used as a second approach for the synthesis of **4**. Ligand **3** (0.15 g, 0.29 mmol) was dissolved in toluene in the glove box and then NBD-Mo(CO)$_4$ was added to the solution and stirred overnight at RT. The solvent was then evaporated. The residue was dissolved in CH_2Cl_2 and then precipitated by the addition of hexanes. The resulting suspension was filtered through a frit. The filtrate was evaporated to afford a yellow solid (54%, 0.113 g, 0.156 mmol). ^{1}H NMR

(300 MHz, CD_2Cl_2): 7.53–7.25 (m, 20H), 7.08 (t, 2H, *J* = 8.4-6.9), 6.73 (t, 1H, *J* = 7.2), 6.38 (d, 2H, *J* = 8.4), 3.32 (m, 4H), 2.65 (m, 4H). $^{13}C\{^1H\}$ NMR (75 MHz, CD_2Cl_2): 148.9 (s), 138.9 (m), 132.6 (m), 129.8 (s), 129 (s), 128.7 (m), 118.6 (s), 114.9 (s), 48.8 (s), 30.26 (t, *J* = 15). $^{31}P\{^1H\}$ NMR (121 MHz, CH_2Cl_2): 25.8 (s). Both solution state and solid state IR data were obtained. (Solid state, in ATR) IR: 2016 cm^{-1}, 1898 cm^{-1} (combination of two peaks), 1863 cm^{-1}. (Solution in CH_2Cl_2 in between KBr discs) IR: 2020 cm^{-1} and 1903 cm^{-1} (combination of 3 bands). Raman spectrum: 2014 cm^{-1}, 1899 cm^{-1} (combination of two bands), 1865 cm^{-1}. Elemental analysis: calculated for *cis*-PNP-$Mo(CO)_4$ C:62.90, H: 4.58, N: 1.93; found %C: 62.92, %H: 4.45, %N: 1.80. Mp: decomposed around 240°C.

A third way to synthesize the compound **4** is that of simply loading CO gas into the solution of **5**. 35 mg of compound **5** was dissolved in THF in a screw-top NMR tube in the glove box, and the tube was connected to the Schlenk line. The line was vacuumed and purged with N_2 three times. Meanwhile, the NMR tube was cooled down to 0°C. The screw top was slightly opened and quickly vacuumed, and then CO gas was loaded for 15 minutes while the CO tank was open. The reaction solution was kept under a positive pressure of CO (with the tank closed) for 50 minutes. $^{31}P\{^1H\}$ NMR was taken, and the major product was compound **4**. The NMR tube was then connected to the Schlenk line. The same steps were followed, and CO was loaded again, this time for 15 min with an open tank and 45 minutes with a closed tank. The conversion of **5** to **4** was quantitative according to the $^{31}P\{^1H\}$ NMR spectrum.

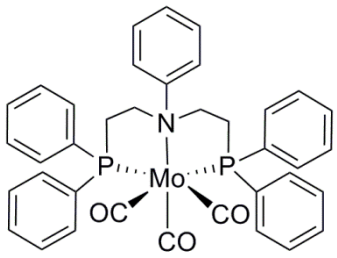

***fac*-PNP-Mo(CO)$_3$ [5].** Both the ligand **3** (0.1g, 0.0001932 mole) and cycloheptatriene tricarbonylmolybdenum (0.053g, 0.0001937 mole) were dissolved in toluene separately in the glove box, and then the metal solution was added to the ligand solution via pipette. The mixture was stirred overnight in the glove box and afforded a precipitate. The precipitate was filtered through a frit layered with celite. The resulting solid was washed twice with toluene and dissolved in dry CH_2Cl_2, then dried in vacuo to afford **5** as a yellow solid (59%, 0.08g, 0.0001147 mole).^{1}H NMR (300 MHz, CD_2Cl_2): 7-8 ppm (m, 25H), 3.67 (m, 4H), 3.16 (m, 4H). ^{31}P{^{1}H} NMR (121 MHz, CD_2Cl_2): 40 (s). HRMS (CI) calculated for fac-PNP-Mo(CO)$_3$ (M+) 671.1041, found 671.1052. Hexanes were layered on a CH_2Cl_2 solution of the product to obtain a crystal suitable for X-ray analysis. Both solution state and solid state IR data were obtained. Solid state IR: 1923 cm^{-1}, 1836 cm^{-1}, 1784 cm^{-1}. Solution state IR (solution in CH_2Cl_2): 1932 cm^{-1}, 1838 cm^{-1}, 1802 cm^{-1}. Raman Spectrum: 1917 cm^{-1}, 1828 cm^{-1}, 1796 cm^{-1} and shoulder at 1782 cm^{-1}. Elemental Analysis: calculated for *fac*-PNP-Mo(CO)$_3$.2H$_2$O %C: 60.58, %H: 5.08, %N: 1.91; found %C: 61.08, %H:4.81, %N: 1.88. Mp: decomposed around 240^{o}C.

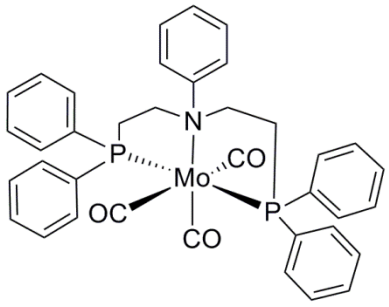

***mer*-PNP-Mo(CO)$_3$ [6].** 50 mg (0.0689 mmol) of **4** was transferred into a 10 mL Schlenk flask and then dissolved in CH_2Cl_2 to afford a clear, burnt orange solution. A stock solution of CH_3NO was prepared by dissolving 49 mg (0.0006524 mole) material in 10 ml of CH_2Cl_2. 1 equivalent (1.06 mL) of the CH_3NO solution was transferred into the Schlenk flask via a syringe and then stirred overnight in the dark at RT. $^{31}P\{^1H\}$ NMR and ^1H NMR were taken, yielding no proof of the product formation. Hexanes were layered on top of the NMR solution to promote crystal formation. **6** was obtained as a minor product (< 1%) of the reaction and observed in X-ray crystallography (**Figure 4**). The remainder of the product was the unreacted starting material **4**.

As a second approach in the synthesis of the *meridional* isomer, we dissolved the *facial* isomer **5** in THF and stirred it for three weeks in the dark in the glove box. Some of the *facial* isomer stayed intact, and some of it decomposed to give the *meridional* isomer, and tetracarbonyl complex **4** in solution, with Mo(0) as a dark precipitate. $^{31}P\{^1H\}$ NMR (121 MHz, CD_2Cl_2): 57.6 (s) *meridional* product, 40 (s) *facial* product, 25 (s) tetracarbonyl complex.

RESULTS AND DISCUSSION

Synthesis

The PNP ligand, **3**, was prepared according to Kostas' method (**Scheme 1**).[38] It was obtained as a white solid. Molybdenum reagents, ($Mo(ACN)_x(CO)_y$, $pip_2Mo(CO)_4$, NBD-$Mo(CO)_4$, and CHT-$Mo(CO)_3$) were reacted with one equivalent of the ligand in each case to obtain the corresponding PNP-$Mo(CO)_n$ complexes (**Scheme 2**). Reaction of CHT-$Mo(CO)_3$ with the PNP ligand **3**, resulted in a *fac*-PNP-$Mo(CO)_3$, **5**. Reactions of $Mo(ACN)_x(CO_)y$, $pip_2Mo(CO)_4$, and NBD-$Mo(CO)_4$ with **3**, resulted in *cis*-PNP-$Mo(CO)_4$, **4**. $Mo(ACN)_x(CO)_y$ reagent was obtained in situ by refluxing $Mo(CO)_6$ in ACN for 1-2 hrs. Commercial NBD-$Mo(CO)_4$ reagent gave the purest product for the synthesis of *cis*-PNP-$Mo(CO)_4$, which is characterized completely. In order to obtain *mer*-PNP-$Mo(CO)_3$, *cis*-PNP-$Mo(CO)_4$ was reacted with $(CH_3)_3NO$. $(CH_3)_3NO$ was prepared by sublimation of $(CH_3)_3NO\cdot 2H_2O$. Reaction mixture of complex **4** and $(CH_3)_3NO$ gave both the *meridional* product and the unreacted *cis*-PNP-$Mo(CO)_4$ as crystals. Only X-ray data of the *meridional* product was obtained from that reaction. Crystals of the *meridional* product was a few and can only be seen under the microscope.

In the second approach of synthesizing the *meridional* product, we used *fac*-PNP-$Mo(CO)_3$. The *facial* isomer was dissolved in THF. The $^{31}P\{^1H\}$ NMR spectrum had a singlet peak initially at 40 ppm. The solution was stirred in the dark for three weeks, and then the $^{31}P\{^1H\}$ NMR spectrum of the solution was measured. Three singlets were observed: 57.6 ppm belongs to *meridional* product **6**, 40 ppm belongs to *facial* product **5**, and 25 ppm belongs to tetracarbonyl complex **4**, which is *cis*. Refluxing **5** in THF overnight gave the same result. We also tried adding PR_3 (R = Et_3, Ph_3, Et_2Ph, $EtPh_2$) into a solution of the *facial* isomer, with the same result: some of the *facial* isomer

decomposed to give the tetracarbonyl product **4**, the *meridional* isomer **6**, unreacted *facial* isomer **5**, some free PNP ligand **3**, and a black precipitate of Mo(0).

Scheme 1. Synthesis of the PNP pincer ligand

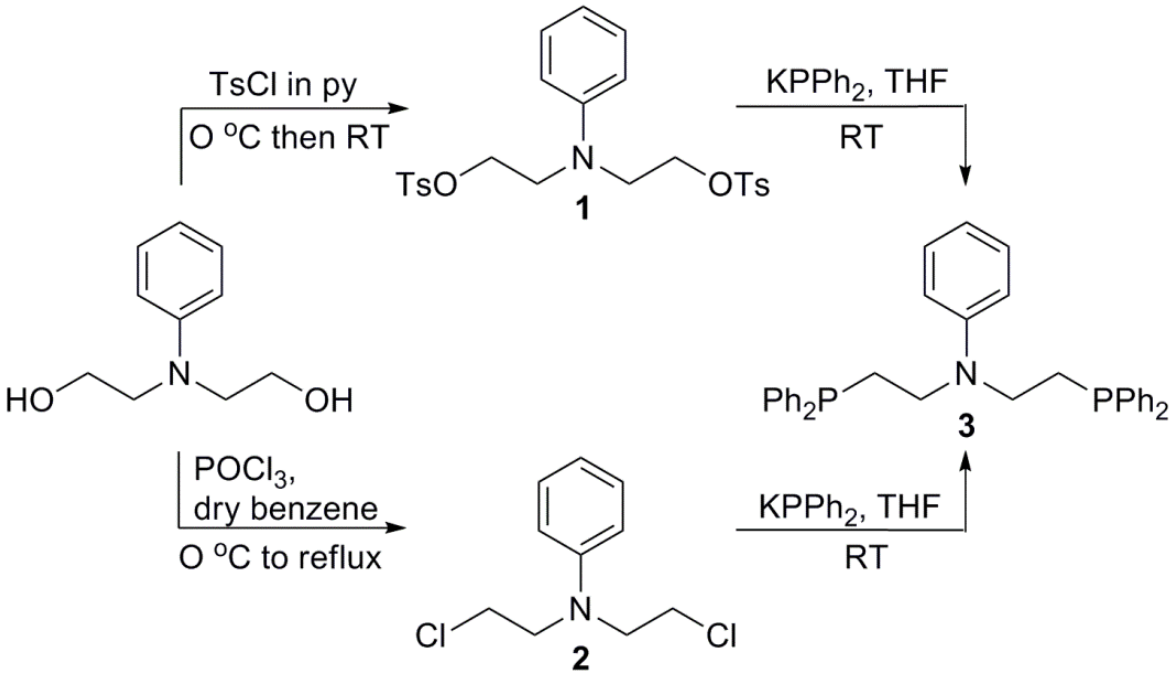

Scheme 2. Synthesis of PNP-Mo(CO)$_n$ complexes and isomers

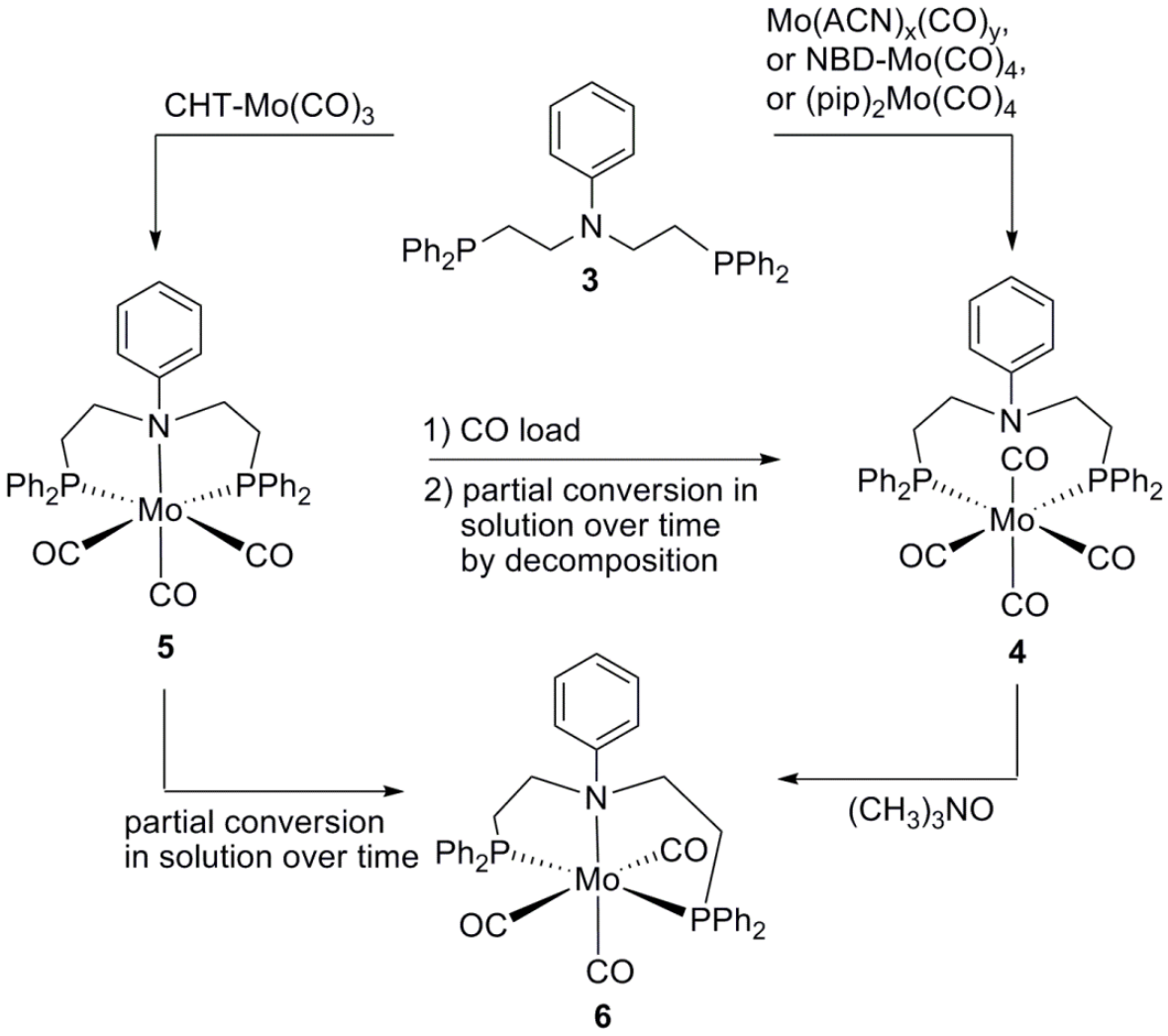

The experimental observations suggest that the conversion of *facial* to *meridional* isomer occurs through the dissociative mechanism. There must be an equilibrium between the isomers, and the *facial* isomer must be the thermodynamically favored product, because stirring a THF solution of pure *facial* isomer **5** gives a black precipitate Mo(0), *cis*-PNP-Mo(CO)$_4$ **4**, and *mer*-PNP-Mo(CO)$_3$ **6**, as well as intact *fac*-PNP-Mo(CO)$_3$ **5**. Some of the *fac*-PNP-Mo(CO)$_3$ must have decomposed to give Mo(0), and

some of the excess carbonyls must have been picked up by another *fac*-PNP-Mo(CO)$_3$ to give *cis*-PNP-Mo(CO)$_4$; the rest of the free carbonyls must be picked up by the five-coordinate intermediate resulting from the dissociation of *fac*-PNP-Mo(CO)$_3$ to give the *mer*-PNP-Mo(CO)$_3$ isomer. That explanation also demonstrates why the *meridional* product is a minor product. Moreover, the literature supports the idea as well. Crabtree explains that ML$_3$(CO)$_3$ complexes undergo dissociative mechanism, and he gives MoL$_3$(CO)$_3$ as a specific example.[76]

Infrared and Raman Studies

All of the complexes are soluble in CH_2Cl_2. Solution and solid state IR data and solid state Raman data obtained for the *fac*-PNP-Mo(CO)$_3$ and *cis*-PNP-Mo(CO)$_4$ (**Figure 18**) are consistent with the proposed molecular structures. For all three complexes, the point group is C_s, which is determined from their crystal structures. Group theory calculations of CO stretches for the three complexes resulted as follows: $\Gamma = 3A' + A''$ for complex **4**, $\Gamma = 2A' + A''$ for complex **5**, and $\Gamma = 3A'$ for the complex **6**. All bands are both Raman and IR active.

IR spectrum of **5** gives three bands, as expected from the calculation; however, Raman spectrum gives three bands and a shoulder (1782 cm^{-1}). Raman and IR spectra of complex **4** give three stretches in the measurements; calculation gives four stretches. On the other hand, one of the stretches (in both spectra) is broad and looks like a combination of two bands (1898 cm^{-1}). The solution state IR spectrum of **4** shows two stretches. It seems that the three bands between 1800 and 1900 cm^{-1} combine to give a broad peak at 1903 cm^{-1}. The other peak is observed at 2020 cm^{-1}.

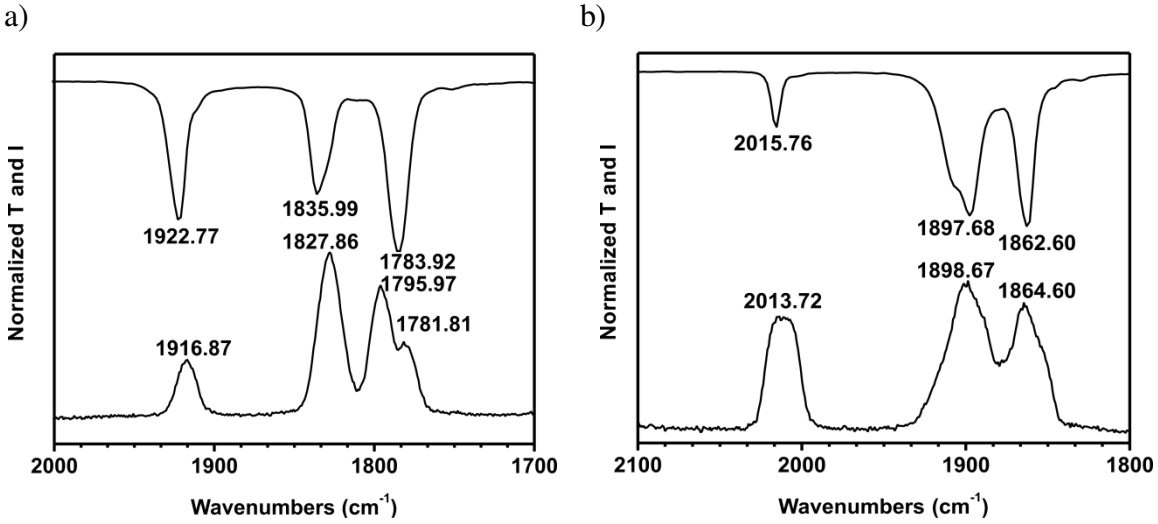

Figure 18. a) Solid state IR and Raman spectra of *fac*-PNP-Mo(CO)$_3$. b) Solid state IR and Raman spectra of *cis*-PNP-Mo(CO)$_4$.

Structure of the Complexes

The solid state structure of complexes **4**, **5**, and **6** were determined by X-ray diffraction analysis. The resulting ORTEP representation can be seen in **Figure 19-21**, and crystallographic and structural refinement data are given in **Table 1**. In complex **4**, the six-coordinate Mo(0) lies at the center of an octahedral environment. The coordination environment around the metal center is defined by two phosphorus atoms from the PNP ligand and four carbon atoms from the carbonyl ligands. Phosphorus atoms are *cis* to each other. In the crystal structure of complex **5** (**Figure 6**), the unit cell contains two *fac*-PNP-Mo(CO)$_3$ complexes, both having a six-coordinate Mo(0) that lies at the center of an octahedral environment. The coordination environment around the metal center is defined by two phosphorus atoms from the PNP ligand *cis* to each other, one N atom from the PNP ligand, and three carbon atoms from the carbonyl ligands in a

facial arrangement. The difference between these two facial complexes is the orientation of the five-membered rings formed upon chelation, i.e. C16 and C17 in one structure have a different orientation than C53 and C54 in the other structure. In complex **6**, the six-coordinate Mo(0) lies, once again, at the center of an octahedral environment. The coordination environment around the metal center is defined by two phosphorus atoms from the PNP ligand, one nitrogen atom from the PNP ligand and three carbon atoms from the carbonyl ligands. The phosphorus atoms are *trans* to each other, with the carbonyl ligands residing in the *meridional* arrangement.

Bond lengths and angles of **4**, **5**, and **6** were compared with similar complexes in the literature. The literature complexes similar to **4** have slightly different angles. For example, the P-Mo-P angle in [ref 65] is 86.75^{o} and in [ref 64] is 88.1^{o}. Compound **4** has a P1-Mo-P2 angle of 94.78^{o}. Bond lengths of the literature complexes and **4** are consistent, however. Complex **5** is consistent with the literature complex both in angles and in bond lengths.[64] In complex **6**, carbonyl carbons that are *trans* to each other (C35-Mo-C37) form a 163^{o} angle, whereas the literature complex has a 171.07^{o} angle. *Trans* phosphines of **6** and the literature value are consistent, although the *trans* carbonyl carbons do not match.[75] Bond lengths are also consistent, except for the Mo-N bond. **6** has a Mo-N distance of 2.424 Å; the literature complex has 2.237 Å.

Table 1. Crystal data and structure refinement for molybdenum complexes.

	4	**5**	**6**
Formula	$C_{38}H_{33}NO_4P_2Mo$	$C_{37}H_{33}NO_3P_2Mo$	$C_{37}H_{33}NO_3P_2Mo$
FW	725.53	697.52	697.52
T (K)	153(2)	153(2)	153(2)
Crystal system	Monoclinic	Monoclinic	Monoclinic
Space group	$P2_1/c$	$P2_1/c$	$C2$
a (Å)	10.027(2)	17.620(4)	19.456(4)
b (Å)	19.158(4)	17.198(3)	12.232(2)
c (Å)	18.646(4)	20.971(4)	13.608(3)
α (deg)	90	90	90
β (deg)	102.853(1)	100.40(3)	95.38(3)
γ (deg)	90	90	90
V (Å^3)	3492.3(12)	3224.2(11)	3224.2(11)
Z	4	8	4
ρ (g/cm^3)	1.38	1.482	1.437
μ (mm^{-1})	0.51	0.56	0.54
F(000)	1488	2864	1432
Crystal size (mm)	0.30 × 0.02 × 0.02	0.46 × 0.06 × 0.07	0.09 × 0.05 × 0.03
θ (deg)	1.0 to 27.5	1.0 to 27.5	1.0 to 27.5
Index ranges	$-13 \le h \le 13$ $-24 \le k \le 23$ $-24 \le l \le 24$	$-20 \le h \le 22$ $-22 \le k \le 18$ $-27 \le l \le 17$	$-25 \le h \le 24$ $-15 \le k \le 15$ $-2 \le l \le 17$
Absorption correction	Multi-scan	Multi-scan	Multi-scan
Max. and min. transmission	0.990 and 0.863	0.994 and 0.896	0.953 and 0.984
GOF on F2	1.02	1.15	1.16
R1, R2 [I > 2σ (I)]	0.0640, 0.1452	0.0585, 0.1225	0.0955, 0.1822
R1, R2 (all data)	0.0758, 0.1487	0.0783, 0.1391	0.1571, 0.2087
Largest diff. peak and hole (e.Å^{-3})	0.66 and -0.63	0.94 and -0.93	1.70 and -1.45

A similar *meridional* PNP-Mo(CO)$_3$ product was reported by O.P. Siclovan *et al.*, but they also could not isolate the *meridional* isomer, although they could successfully synthesize and purify the *facial* isomer.[63] The choice of the *facial* or *meridional* isomer

was explained by electronics rather than sterics in the literature: when the monodentate ligand is negatively charged, such as halogens, the preferred geometry becomes *meridional* because of the electrostatic repulsions between the halogens. In the case of neutral monodentate ligands such as the carbonyl ligand, the preferred geometry is *facial* in the complex.[58, 66] The explanation for the stability of the complexes of *meridional* and *facial* isomers electronics of the monodentate ion plays a role rather than sterics did not satisfactorily explain our experimental observations. We studied the system and formed several explanations, all of which are consistent with each other:

First, the angles around the Mo atom (taken from the crystal structure data) were compared in each complex to find if there is any angular distortion that can cause the difference in stability. The angles of the *meridional* isomer around the O_h Mo atom are the most distorted ones among the three complexes. In addition, the angles between Mo and the carbonyl groups, which should be 180^o, are again distorted the most in the *meridional* isomer. The most distorted angles in the *meridional* isomer are as follows (having distorsions greater than 10^o); C35-Mo-C36: 78.8^o, C35-Mo-C37: 163.1^o, C35-Mo-N: 103.1^o, N-Mo-P1: 79.1^o, C36-Mo-P1: 101.4^o, N-Mo-P2: 79.8^o, P1-Mo-P2: 158.5^o. The difference from the ideal angles varies from 10.2^o to 21.5^o (7 angles).The most distorted angles in the *facial* isomer **5** are as follows are as follows; C3-Mo1-N1: 100.4^o, C3-Mo1-P1: 168.4^o, N1-Mo1-P1: 78.68^o, C1-Mo1-P2: 169.0^o, N1-Mo1-P2: 78.69^o, C40-Mo2-N2: 100.9^o, C40-Mo2-P3: 163.7^o, N2-Mo2-P3: 77.66^o, N2-Mo2-P4: 77.63^o, P3-Mo2-P4: 100.84^o. The difference from the ideal angles for Mo1 varies from 10.4^o to 11.32^o (5 angles); for Mo2, the difference varies from 10.84^o and 16.3^o. The most distorted angle in complex **4** was only 7.3^o. The less distorted angles in the molecule should result in the more stable complex. Moreover, the P-Mo-P angle in the *meridional* isomer **6** is distorted by 21.5^o; the C-Mo-C (*trans*) angle is distorted by 16.9^o. The largest

angular distortions between the C-Mo-C atoms in facial isomer **5** are 8.8° for C38-Mo2-C40 and 3.03° for C1-Mo1-C3. The P-Mo-P angle in complex **5** is distorted by 3.62° for P1-Mo1-P2 and 10.84° for P3-Mo2-P4. Angles are distorted much less in compound **5** than in compound **6**. **Tables 2–5** show the O_h angles around the Mo atom and the Mo-C-O angles in each complex, as well as the deviation from the ideal angles. The corresponding pictures of crystal structures indicate the labeled atoms in **Figures 19-21**.

The second argument concerns the bond distances, *trans* effect and π-backdonation. **Tables 4-6** show the distances of each atom to the Mo center in the O_h environment. We observed that Mo-C distances are slightly shorter in complex **5** than in complex **6**. In complex **4**, the carbonyls that are *trans* to each other have a longer distance from the Mo atom (Mo-C2: 2.027 Å and Mo-C3: 2.049 Å) than the other two carbons, which are *cis* to each other and therefore *trans* to the diphenyl phosphine groups (Mo-C1: 1.982 Å and Mo-C4: 1.978 Å). All of these observations can be explained by the *trans* effect together with π-backdonation. The diphenyl-phosphine group is a much better electron-donating group than the carbonyl group. Therefore, the carbonyls that are *trans* to the phosphines benefit from the π-backdonation and are more tightly held by the metal; as a result, M-C distances are shorter for those carbonyls.[76] This is exactly what we observe in the *facial* complex **5,** in which all M-C distances are less than 2 Å (1.933 Å to 1.979 Å). In complex **6**, phosphines that have less *trans* effect than the carbonyls are *trans* to each other, and the M-P bonds are shorter. As one would expect, the carbonyls that are *trans* to each other have longer M-C distances (Mo-C35: 2.00Å and Mo-C37: 1.99Å), which makes for a poor π-backdonation. Furthermore, the M-C distances in which carbonyls are *trans* to the N atom in both complex **5** and **6** are shorter (for **5** Mo1-C2: 1.933 Å, Mo2-C39:1.937 Å; for **6** Mo-C36: 1.93 Å) than the other M-C distances (1.98 Å for 5, 1.99-2.00 Å for **6**) (*trans* to either phosphine or carbonyl). The reason is

that there is a slight π-backdonation from the metal to the phosphine; therefore, the N atom becomes a better electron donor than the phosphine, and the carbonyls *trans* to the N atom benefit from that electron donation.[77]

We also studied the angles and bond distances of *mer*-PNP-$MoCl_3$, which was reported by Fernandez-Trujillo *et al*.[58] It is not surprising that the *mer*-PNP-$MoCl_3$ complex is more stable than our *mer*-PNP-$Mo(CO)_3$ and can synthetically be made, because Cl^- has a less *trans* effect than CO groups and also than phosphines; in addition, there are ionic bonds between Mo^{3+} and each Cl^- that should be stronger than the Mo-CO bonds. There are still angular distortions for *mer*-PNP-$MoCl_3$ compared to complexes **5** and **6**. The angular distortions greater than 10^o around the Mo atom in the complex *mer*-PNP-$MoCl_3$ taken from the literature are P2-Mo-P3: 161.2^o and P2-Mo-Cl7: 101.2^o; their differences from ideality are 18.8^o and 11.2^o, respectively. The rest of the angles and distortions can be found in **Table 9**. The distances of the atoms from Mo in the O_h environment for *mer*-PNP-$MoCl_3$ are listed in **Table 10**.

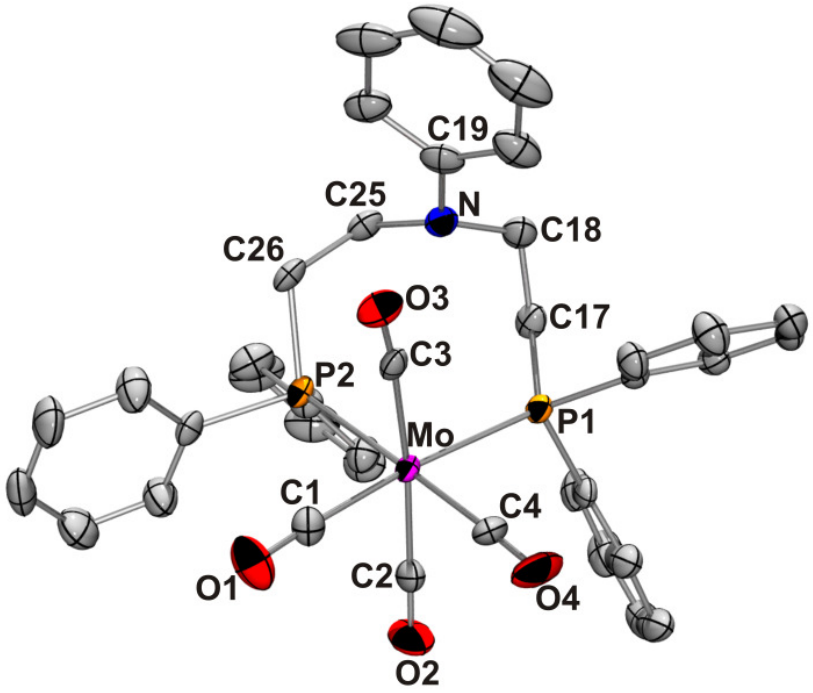

Figure 19. Crystal structure of *cis*-PNP-Mo(CO)$_4$ (**4**) showing the labeling of selected atoms. Hydrogen atoms have been omitted for clarity. Displacement ellipsoids are scaled to the 50% probability level.

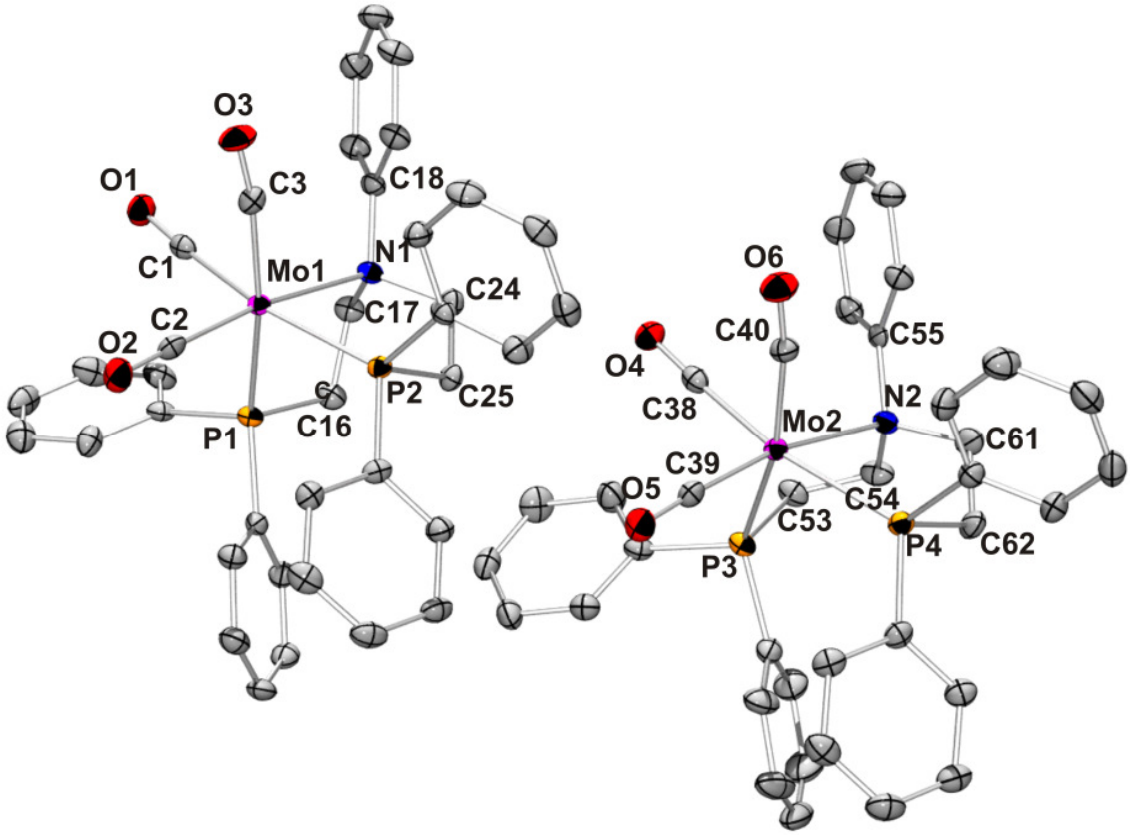

Figure 20. Crystal structure of *fac*-PNP-Mo(CO)$_3$ (**5**) showing the labeling of selected atoms. Hydrogen atoms have been omitted for clarity. Displacement ellipsoids are scaled to the 50% probability level.

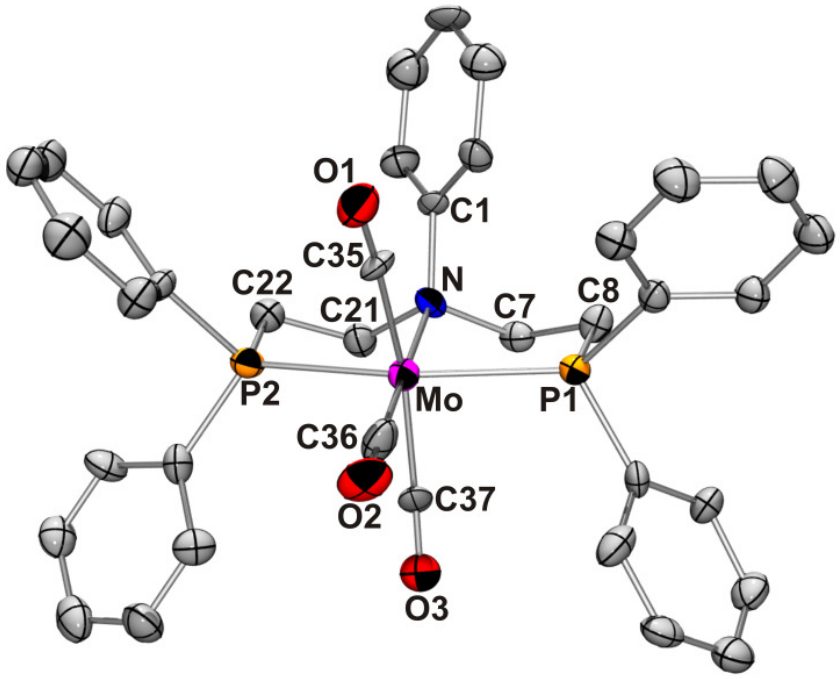

Figure 21. Crystal structure of *mer*-PNP-Mo(CO)$_3$ (**6**) showing the labeling of selected atoms. Hydrogen atoms have been omitted for clarity. Displacement ellipsoids are scaled to the 50% probability level.

Table 2. Angles around O_h Mo atom and Mo-C-O for compound **4**.

cis-PNP-Mo(CO)$_4$	Angle	Ideal angle	Difference
C1-Mo-C2	87.4(1)	90	-2.6
C1-Mo-C3	85.4(1)	90	-4.6
C1-Mo-C4	86.1(1)	90	-3.9
C1-Mo-P1	174.5(1)	180	-5.5
C1-Mo-P2	90.5(1)	90	-0.5
C2-Mo-C3	172.7(1)	180	-7.3
C2-Mo-C4	88.3(2)	90	-1.7
C2-Mo-P1	90.7(1)	90	0.7
C2-Mo-P2	94.0(1)	90	4
C3-Mo-C4	90.0(1)	90	0
C3-Mo-P1	96.37(9)	90	6.37
C3-Mo-P2	87.25(9)	180	-2.74
C4-Mo-P1	88.7(1)	90	-1.3
C4-Mo-P2	175.8(1)	180	-4.2
P1-Mo-P2	94.78(3)	90	4.78
Carbonyl groups			
O1-C1-Mo	175.4(3)	180	-4.6
O2-C2-Mo	175.2(3)	180	-4.8
O3-C3-Mo	173.1(3)	180	-6.9
O4-C4-Mo	177.4(3)	180	-2.6

Table 3. Angles around O_h Mo atom and Mo-C-O for compound **5**.

fac-PNP-Mo(CO)$_3$	Angle	Ideal angle	Difference
C1-Mo1-C2	93.0(1)	90	-3
C1-Mo1-C3	82.3(1)	90	3.03
C1-Mo1-N1	90.5(1)	90	-0.5
C1-Mo1-P1	86.1(1)	90	-3.1
C1-Mo1-P2	169.0(1)	180	11
C2-Mo1-C3	87.5(1)	90	-2.5
C2-Mo1-N1	171.7(1)	180	-8.3
C2-Mo1-P1	94.1(1)	90	4.1
C2-Mo1-P2	98.0(1)	90	8
C3-Mo1-N1	100.4(1)	90	10.4
C3-Mo1-P1	168.4(1)	180	-11.6
C3-Mo1-P2	97.6(1)	90	7.6
N1-Mo1-P1	78.67(7)	90	-11.32
N1-Mo1-P2	78.68(7)	90	-11.31
P1-Mo1-P2	93.62(3)	90	3.62
C38-Mo2-C39	92.1(1)	90	2.1
C38-Mo2-C40	81.2(1)	90	-8.8
C38-Mo2-N2	94.3(1)	90	4.3
C38-Mo2-P3	82.8(1)	90	-7.2
C38-Mo2-P4	170.1(1)	180	-9.9
C39-Mo2-C40	88.9(1)	90	-1.1
C39-Mo2-N2	169.0(1)	180	-11
C39-Mo2-P3	94.3(1)	90	4.3
C39-Mo2-P24	96.9(1)	90	6.9
C40-Mo2-N2	100.9(1)	90	10.9
C40-Mo2-P3	163.7(1)	180	-16.3
C40-Mo2-P4	94.6(1)	90	4.6
N2-Mo2-P3	77.65(7)	90	-12.34
N2-Mo2-P4	77.62(7)	90	-12.37
P3-Mo2-P4	100.84(3)	90	10.84

Table 4. Mo-C-O angles for compound **5**.

O1-C1-Mo1	176.0(3)	180	-4
O2-C2-Mo1	178.7(3)	180	-1.3
O3-C3-Mo1	171.5(3)	180	-8.5
O4-C38-Mo2	176.2(3)	180	-3.8
O5-C39-Mo2	177.0(3)	180	-3
O6-C40-Mo2	171.4(3)	180	-8.6

Table 5. Angles around O_h Mo atom and Mo-C-O for compound **6**.

mer-PNP-Mo(CO)$_3$	Angle	Ideal angle	Difference
C35-Mo-C36	78.7(5)	90	-11.2
C35-Mo-C37	163.0(5)	180	-16.9
C35-Mo-P1	99.8(3)	90	9.8
C35-Mo-P2	89.0(3)	90	-1
C35-Mo-N	103.1(4)	90	13.1
C36-Mo-C37	84.5(5)	90	-5.4
C36-Mo-P1	101.4(4)	90	11.4
C36-Mo-P2	99.6(4)	90	9.6
C36-Mo-N	178.1(4)	180	-1.9
C37-Mo-P1	86.4(3)	90	-3.6
C37-MoP2	99.6(4)	90	9.6
C37-Mo-N	90.8(3)	90	0.8
N-Mo-P1	79.1(2)	90	-10.9
N-Mo-P2	79.8(2)	90	-10.2
P1-Mo-P2	158.5(1)	180	-21.5
Carbonyl groups			
O1-C35-Mo	173(1)	180	-7
O2-C36-Mo	177(1)	180	-3
O3-C37-Mo	175(1)	180	-5

Table 6. Bond lengths [Å] around Mo atom for compound **4**.

cis-PNP-Mo(CO)$_4$	Bond Lengths
Mo-C1	1.982(3)
Mo-C2	2.027(4)
Mo-C3	2.049(3)
Mo-C4	1.978(3)
Mo-P1	2.551(1)
Mo-P2	2.5404(9)

Table 7. Bond lengths [Å] around Mo atom for compound **5**.

fac-PNP-Mo(CO)$_3$	Bond Lengths
Mo1-C1	1.979(4)
Mo1-C2	1.933(3)
Mo1-C3	1.977(3)
Mo1-N1	2.466(3)
Mo1-P1	2.496(1)
Mo1-P2	2.512(1)
Mo2-C38	1.977(4)
Mo2-C39	1.937(3)
Mo2-C40	1.977(3)
Mo2-N2	2.489(3)
Mo2-P3	2.495(1)
Mo2-P4	2.543(1)

Table 8. Bond lengths [Å] around Mo atom for compound **6**.

mer-PNP-Mo(CO)$_3$	Bond Lengths
Mo-C35	2.00(1)
Mo-C36	1.93(1)
Mo-C37	1.99(1)
Mo-P1	2.458(3)
Mo-P2	2.442(3)
N-Mo	2.424(9)

Table 9. Angles around O_h Mo atom for the compound *mer*-PNP-$MoCl_3$.[58]

mer-PNP-$MoCl_3$	Angle	Ideal angle	Difference
N1-Mo-P2	80.5	90	-9.5
N1-Mo-P3	81.1	90	-8.9
N1-Mo-Cl5	87	90	-3
N1-Mo-Cl6	91.1	90	1.1
N1-Mo-Cl7	177.2	180	-2.8
P2-Mo-Cl5	86.8	90	-3.2
P2-Mo-Cl6	88.9	90	-1.1
P2-Mo-Cl7	101.2	90	11.2
P2-Mo-P3	161.2	180	-18.8
P3-Mo-Cl5	88.5	90	-1.5
P3-Mo-Cl6	95.2	90	5.2
P3-Mo-Cl7	97	90	7
Cl5-Mo-Cl6	175.5	180	-4.5
Cl5-Mo-Cl7	91	90	1
Cl6-Mo-Cl7	91.1	90	1.1

Table 10. Bond lengths [Å] around Mo atom for compound *mer*-PNP-$MoCl_3$.[58]

mer-PNP-$MoCl_3$	Bond Lengths
Mo-N	2.332
Mo-P2	2.524
Mo-P3	2.541
Mo-Cl5	2.417
Mo-Cl6	2.395
Mo-Cl7	2.376

CONCLUSIONS

Three different PNP-Mo(CO)$_n$ complexes (where n = 3, 4) were synthesized, and characterized, and the conversion reactions among them were investigated. The synthesis and purification of *fac*-PNP-Mo(CO)$_3$ and *cis*-PNP-Mo(CO)$_4$ were successfully done. However, we could never control the synthesis of *mer*-PNP-Mo(CO)$_3$; it was observed as a minor product in the synthesis reactions by ^{31}P NMR and X-ray diffraction measurements. The solution of *fac*-PNP-Mo(CO)$_3$ partially decomposes over time to give *cis*-PNP-Mo(CO)$_4$, *mer*-PNP-Mo(CO)$_3$, and Mo(0) as a dark precipitate. The observation showed that *fac*-PNP-Mo(CO)$_3$ undergoes a dissociative mechanism. Angular distortions are bigger in *meridional* complex than the other two (**4** and **5**) with the highest value of 21.5^o and Mo-C bonds are longer in *meridional* than *facial* complex. We conclude that the *facial* isomer is favored compared to the *meridional* isomer because of the *trans* effect, π-backdonation and Jahn-Teller effect; we conclude contrary to the literature, that the cause is not electronic.[58, 66]

Chapter 3: Polymerizable N,N-bis[2-(diphenylphosphino)ethyl]aniline Complexes of Molybdenum

INTRODUCTION

Materials made from conjugated polymer systems have been very popular because of their ease of preparation, mechanical processability and electrical conductivity upon doping.[6] Transition metals have been incorporated into these systems to have interesting redox, magnetic, optical, or catalytic properties.[78]

Recently, conjugated polymers with redox-active ligand sites have been investigated to affect the reactivity and binding of transition metal complexes. A conjugated polymer matrix has a large number of available oxidation states. This variety of oxidation states can be used to tune the amount of electron density on the metal center and consequently affect the binding of an additional ligand.[79-81] Reactivity of metal complexes that have redox active ligands can be modulated without changing the immediate coordination sphere. Systems such as these have potential applications in small molecule storage and delivery,[82] electrochemical sensors,[83] and catalysis.[84]

Several redox active complexes have been reported in the literature so far. Many of them used metallocene complexes with or without carbonyl ligands attached to them. Metal carbonyls are practical in monitoring the changes upon ligand oxidation and reduction because M–CO stretches depend on electron density on the metal center and can be monitored by IR spectroscopy. Terminally bound carbonyl complexes are observed between ~1750 – 2100 cm^{-1}. Free carbonmonoxide has its stretching frequency in the gas phase at 2143 cm^{-1}.[77]

Wrighton and coworkers synthesized and studied a series of ferrocene-appended rhenium carbonyl complexes as well as cobaltocene systems. They demonstrated that carbonyl stretching frequencies shifted to higher values upon oxidation due to lowered

electron density on the rhenium center. They also showed that the magnitude of the shift depends on the number of bonds between rhenium and ferrocene moieties.[79] Bielawski *et al.* integrated a 1,1'-disubstituted ferrocene moiety into an N-heterocyclic carbine ligand. They could oxidize the complex by 0.9V. The ferrocene ligand was oxidized; however, rhodium (I/II) was not, resulting in two carbonyl stretches shifted by 18 and 23 cm^{-1}, which confirmed that rhodium centers and redox active carbine ligand were electronically communicating.[85]

Metallopolymers with redox active units were also studied. Wolf and Wrighton prepared metallopolymers to change the electron density at the metal center by a function of charge in the conducting polymer backbone. The resulting changes were demonstrated by peak frequencies of CO stretches in the IR spectrum of 4 and 6 cm^{-1} between neutral and oxidized systems.[81] Mirkin *et al.* worked with ruthenium and rhodium complexes and their polymer systems to make electrochemically tunable redox-active ligand systems. They found that the monothiophene rhodium complex was not suitable for redox-active ligand systems, because rhodium was oxidized before the monothiophene, and polymer growth was inhibited. Systems with terthiophene could easily be polymerized. Hydrogenation of norbornadiene ligands, on the other hand, results in polymers that cannot be used as hemilabile ligands. They also reported a ruthenium-terthiophene based polymer with a reversible increase in CO stretching; however, no tunable change was observed, and these systems can utilize thiophene and polythiophene derivatives as redox-active ligand systems.[82, 86] Recently, Milum and Holliday reported a conducting metallopolymer based on an electropolymerizable NCN pincer ligand which containing platinum and 2,6-dimethylphenyl isocyanide. The amount of electron density on the platinum atom was probed by the isocyanide ligand. The IR stretching frequency was lowered by 9 cm^{-1} upon oxidation of the polymer film, indicating that the Pt-C σ-bond

was weakened due to the withdrawal of electrons from the conducting polymer backbone. They showed redox attenuated metal–ligand interactions also by monitoring with UV-Vis spectroelectrochemistry without the incorporation of a reporter ligand.[45]

Molybdenum-containing hybrid and coordination polymers have been reported for various applications.[87-95] Boruah *et al.* reported polymer-anchored peroxo compounds of vanadium(V) and molybdenum(VI) for their activities with alkaline phosphatase (ALP) and catalase. They used poly(sodiumacrylate) (PA), poly(sodium methacrylate) (PMA), poly-(acrylamide) (PAm), and poly(sodium 4-styrene sulfonate) (PSS) and a copolymer poly(sodium styrene sulfonate-co-maleate) (PSSM) as supports. They found that the polymer-anchored and free monomeric peroxo compounds tested induced their inhibitory effects on ALP through distinctly different pathways. Each of the macromolecular compounds tested is a noncompetitive inhibitor of ALP. Free peroxo metal compounds, on the other hand, exert a mixed type of inhibition on the enzyme function. These findings are likely to have clinical importance.[87] Moreno *et al.*, prepared (hydroxypropyl)-2-aminomethyl pyridine containing hybrid polymer–silica SBA-15 materials supporting Mo(VI) centers and they studied it for heterogeneous catalysts for oct-1-ene epoxidation. The materials they prepared displayed high catalytic activity, stability and reusability in the epoxidation of 1-octene with TBHP (tert-butyl hydroperoxide) as oxidant. The presence of mesoporosity in the final Mo(VI) containing hybrid materials improved the catalytic activity of metal centers.[88] Maurya *et al.* also used polymer-anchored hybrid materials of oxovanadium(IV), dioxomolybdenum(VI), and copper(II) complexes of the bidentate ligand 2-(2 -hydroxyphenyl)benzimidazole to investigate their catalytic activities in the oxidation of styrene and ethylbenzene.[89] Schrock and coworkers synthesized polymer-supported chiral Mo-based complexes as efficient catalysts for enantioselective olefin metathesis. They obtained optically enriched

products through the use of the supported complexes. The products contained significantly lower levels of metal impurities compared to products synthesized with the corresponding homogeneous catalysts.[90] Shultz and coworkers reported the acyclic diene metathesis (ADMET) polymerization of an organometallic molybdenum-containing diene (*cis* -$Mo(CO)_4(Ph_2P(CH_2)_3CH{=}CH_2)_2$) and its copolymerization with an organic diene (**Figure 22**).[91] Kim *et al.* synthesized terthiophenes bearing pendant organomolybdenum complexes and electropolymerized them to obtain electroactive films. They obtained the absorption spectra of the polymer films and observed $\sigma \rightarrow \sigma^*$ transition of the Mo–acetylenic carbon bond, the $d_\pi \rightarrow d_{\pi^*}$ transition of the Mo-Mo bond $\pi \rightarrow \pi^*$ transition of the polymer backbone.[96]

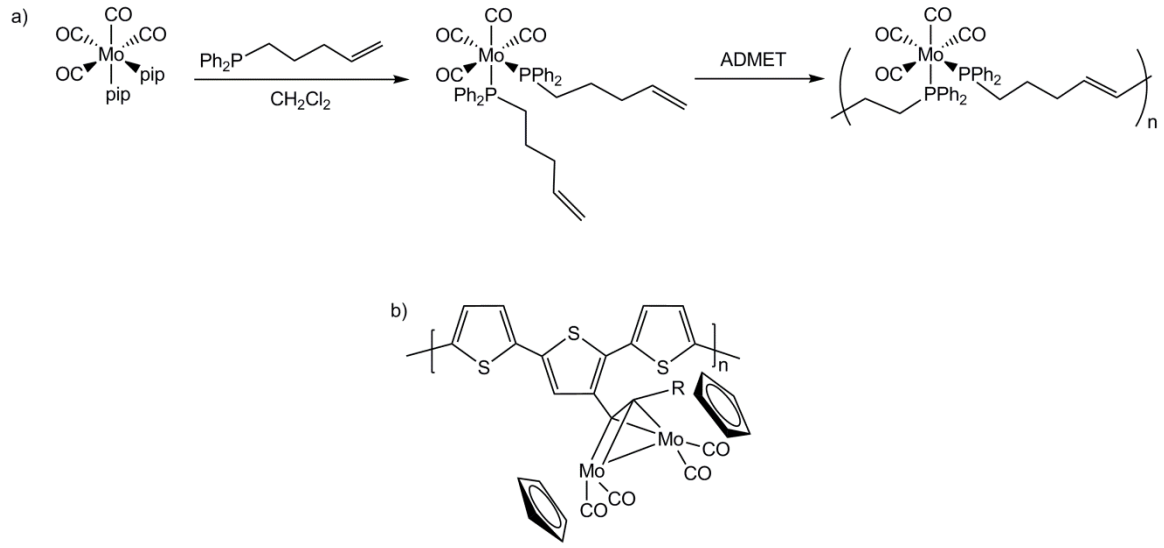

Figure 22. Molybdenum carbonyl containing polymers.[91, 96]

In addition to polymer-anchored molybdenum complexes, a number of coordination polymers of molybdenum have been reported. Chelebaeva *et al.* synthesized one-dimensional cyano-bridged coordination polymers based on the luminescent

lanthanide ion Nd^{3+} and the $[Mo(CN)_8]^{3-}$ building block, i.e. $Nd(phen)_n(DMF)_m[M(CN)_8]$ (M = Mo, W). Adjustment of the number of phenanthroline ligands in the coordination sphere of the lanthanide was reached by modulating the experimental conditions. These compounds displayed the Nd^{3+} typical NIR emission enhanced by the presence of the phenanthroline ligand and ferromagnetic interactions between Nd^{3+} and Mo^{5+} ions.[92] Another molybdenum-containing coordination polymer was obtained by Matsumoto *et al.* to study metal-dependent and redox-selective coordination behaviors of the metalloligand [MoV(1,2-benzenedithiolato$_3$]- with Cu(I)/Ag(I) ions. They found that the complex with copper has a 1-D structure; the complex with silver had a 3-D structure due to additional π-π stacking interactions between adjacent [MoV(bdt$_3$]- moieties.[93] Zhang *et al.* synthesized a non-interpenetrating 3-D $[MoOS_3Cu_3]$ based coordination polymer and found third-order nonlinear optical properties.[94] Das *et al.* synthesized a coordination polymer for catalytic applications. Hexahydro-5-oxoquinoline-3-carboxylates and 1,4-dihydropyridine-3,5-dicarboxylates were synthesized efficiently and rapidly (2 min) in the presence of molybdenum- and tungsten-based coordination polymers $[M(Bu_3Sn)_2O_4)]_n$ (M = Mo or W) as catalyst. The products were formed at room temperature in excellent yields (90–98%). The catalysts worked under heterogeneous conditions and were recyclable.[95]

The purpose of this study is to synthesize and characterize an electropolymerizable tridentate ligand, corresponding molybdenum complexes with carbonyl groups, and electropolymerization of these compounds. Also, redox attenuated binding can be evaluated by IR spectroscopy of the carbonyl functionality. Tridentate ligands give more stable metal complexes than bidentate ligands, and they also allow the metal center to have ancillary ligands. Metal carbonyls are chosen because carbonyl groups are useful in evaluating the electron density around the metal center, which is

affected by the ligand oxidation and reduction, and the M–CO stretching frequencies can be monitored spectroscopically. Two different M–CO systems are targeted; in the first one, the metal is directly bound to a conjugated polymer backbone through N coordination and makes a Wolf type II[5] conducting metallopolymer; the second one has no bond between M and N atom, therefore forming a Wolf type I[5] conducting metallopolymer. The reason of designing two polymers is to see if the applied potential exerts any control over the carbonyl release in these different types of metallopolymers; in other words, metal-polymer backbone communication may be evaluated to determine whether it has any effect on carbonyl release.

Electropolymerization is the technique that we use instead of chemical polymerization. An applied potential electrochemically oxidizes 3,4-ethylenedioxythiophene (EDOT) sites and forms radical cations, which couple to form a dication dimer that subsequently becomes a neutral dimer through the loss of two protons. This process continues until a polymer is deposited at the anode. Electropolymerization is convenient for bithiophene (BT) or EDOT groups; it is preferred, because there is no need to purify the polymer formed at the anode and there are no byproducts. After polymerization, abstraction of electrons from the polymer backbone by electrochemical techniques results in a p-doped (or positively charged) semiconductor. Conduction in the polymer backbone causes the metal centers to change in effective charge or even in oxidation state; this should result in small molecule release due to the lack of electrons for the π-backdonation to the metal center. (**Figure 23**)

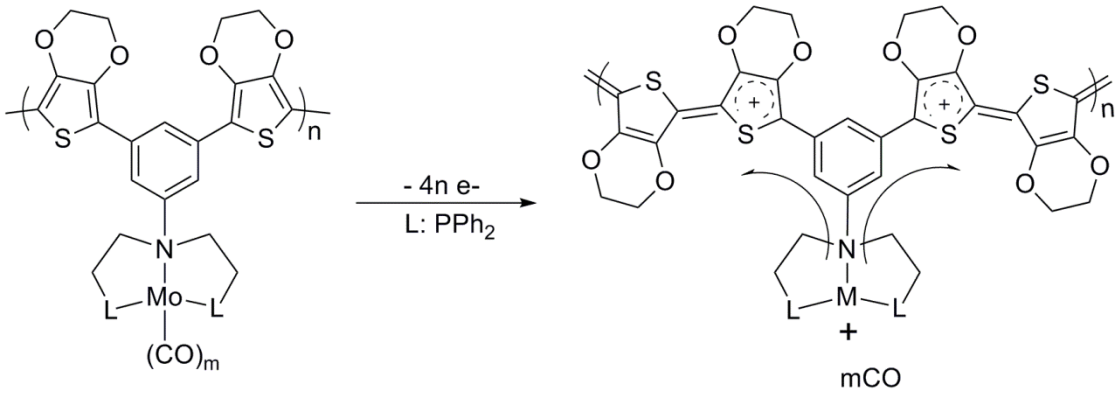

Figure 23. Change in electron density upon oxidation of the polymer.

EXPERIMENTAL

Instrumentation

^{1}H NMR spectra were recorded with a Varian Unity + 300 spectrometer and were referenced to residual solvent peaks $^{31}P\{^{1}H\}$ NMR spectra were referenced to a H_3PO_4 external standard. $^{13}C\{^{1}H\}$ NMR spectra were referenced relative to solvent peaks. All peak positions are listed in ppm, and all coupling constants are listed in Hertz (Hz). Mass spectrometry was carried out using a Waters Autospec Ultima spectrometer. IR spectra were recorded with a Nicolet Avatar 330 FT-IR spectrophotometer. Solid state IR measurements were obtained using an ATR accessory. Solution IR data was recorded using DCM solutions (~ 10^{-2} M). X-ray photoelectron spectroscopy (XPS) was carried out on a PHI 5700 XPS system equipped with dual Mg X-ray sources and monochromatic Al X-ray source complete with depth profile and angle-resolved capabilities. Elemental analysis was performed by QTI, Whitehouse, NJ. The microwave assisted reaction was performed in a CEM Discover reactor. Samples were freshly prepared prior to analysis.

X-ray Crystal Structure Analysis

The single–crystal diffraction data were collected on a Rigaku AFC12 diffractometer with a Saturn 724+ CCD, using a graphite monochromator with MoKα radiation (λ = 0.71073Å). Absorption corrections were applied using Multi-scan. Data reductions were performed using Rigaku Americas Corporation Crystal Clear version 1.40.[97] The structures were solved by direct methods and refined anisotropically using full-matrix least-squares methods with the SHELX 97 program package.[70, 71] The coordinates of the non-hydrogen atoms were refined anisotropically, while hydrogen

atoms were included in the calculation isotropically but not refined. Neutral atom scattering factors and values used to calculate the linear absorption coefficient are from the International Tables for X-ray Crystallography (1992).[72] Crystal data collection and refinement details are given in **Table 11**. Selected bond lengths are given in **Table 12**.

Electrochemistry

Electrochemical syntheses and scan rate dependence studies were performed by using a GPES system from Eco. Chemie B.V. in a glove box under a nitrogen atmosphere. $Ag/AgNO_3$ reference electrode, Pt wire coil counter electrode and a Pt working electrode were used in the electrochemical cell. For the XPS and IR measurements of the polymers, ITO coated glass was used as a working electrode instead of the Pt button. In the reference electrode, Ag wire was dipped in a 0.01 M $AgNO_3$ solution with 0.1 M $[(n\text{-}Bu)_4N][PF_6]$ ($TBAPF_6$) in CH_3CN. Potentials measured were relative to the reference electrode which needed to be calibrated by external reference ferrocene. Calibrations were done before and after experiments were performed. The average of the ferrocene measurements was determined and used to correct the measured potentials. Solution of 0.1 M ($TBAPF_6$) in CH_2Cl_2 was used as the electrolyte. $TBAPF_6$ had to be purified. Hot ethanol was used to recrystallize $TBAPF_6$ three times and then the white crystals were dried for 3 days at above 100 °C under active vacuum. Polymer films were prepared on Delta Technologies ITO-coated glass for spectroscopic measurement and for XPS. Electrochemical syntheses of the polymer films were preformed from ~1 x 10^{-3} M monomer solutions by continuous cycling between -1.4 V (or -0.25 V) and 1.5 V at v = 100 mVs^{-1} (potentials are before referencing with ferrocene). The polymer films

were washed with dry CH_2Cl_2 in the glove box to remove any monomer or electrolyte left on the films before further experiments.

Synthesis

General Methods

All chemicals were purchased from commercial suppliers and were used as received. Dry solvents were obtained from an Innovative Technologies Pure-Solv 400 solvent purification system. Air- and moisture-sensitive reactions were carried out in oven-dried glassware using standard Schlenk techniques under an inert nitrogen atmosphere or in a glove box with an argon atmosphere. The syntheses of *fac*-$EDOT_2PNP\text{-}Mo(CO)_3$ **15** and *cis*-$EDOT_2PNP\text{-}Mo(CO)_4$ **16** were achieved by techniques similar to Blower's[74] and Ainscough's[75], respectively. 2-(tributylstannyl)-3,4-(ethylenedioxy)thiophene was prepared by Swager's method.[98]

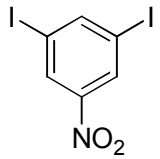

1-nitro-3,5-diiodobenzene [7]. 2,6-diiodo-4-nitroaniline (7g, 17.95 mmol) was dissolved in 0 ^oC H_2SO_4 (98%, 27 ml) adding by small portions. After dissolution was completed, $NaNO_2$ (2.693 g) was added portionwise. After all has been added, mixture was stirred for 2 hrs at 0^oC. The resulting dark, viscous solution was poured over crushed ice (180 g) and stirred. The burnt orange precipitate was filtered off. The filtrate was carefully added into the refluxed solution of $CuSO_4.5H_2O$ (0.6825 g) in C_2H_5OH (360 ml) and heated to 90^oC, then stirred at that temperature for 2 hrs. The mixture was cooled to 0^oC to promote precipitation. The precipitate was collected by vacuum filtration and washed three times

with a C_2H_5OH/H_2O (1:1) mixture (50 ml total). The product was dried under vacuum (65%, 4.374 g, 11.67 mmol). ^1H NMR (300 MHz, $CDCl_3$): δ = 8.354 (t, J = 1.2 Hz, 1H), 8.499 (d, J = 1.2 Hz, 2H). Purity and composition were confirmed by comparing ^1H NMR data with literature values.[99]

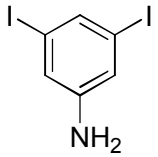

3,5-diiodoaniline [8]. $SnCl_2.2H_2O$ (15.1734 g) was added to a suspension of 1-nitro-3,5-diiodobenzene **7** (5g, 13.34 mmol) in C_2H_5OH (80 ml). This mixture was boiled, and a solution of $NaBH_4$ in C_2H_5OH was added dropwise. The reaction mixture was refluxed for 30 min, then cooled to RT and quenched with H_2O, then neutralized with NaOH (aq). An intense white precipitate resulted. The mixture was extracted with CH_2Cl_2 three times. The organic phases were combined, dried over $MgSO_4$, and vacuum filtered, and the filtrate was evaporated to afford a cream-colored solid. The product was further dried under vacuum (88 %, 4.048 g, 11.736 mmol). ^1H NMR (300 MHz, $CDCl_3$): δ = 7.376 (t, J = 1.5 Hz, 1H), 6.96 (d, J = 1.5 Hz, 2H), 3.651 (broad s, 2H). ^1H NMR data is consistent with the literature values.[100]

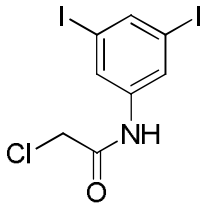

3,5-diiodo-N-[2-chloroethy]-anilide [9]. 3,5-diiodoaniline **8** (4.17 g, 12.09 mmol) and $N(C_2H_5)_3$ (8.7 ml) were dissolved in dry CH_2Cl_2 (130 ml) and cooled to 0^oC. Chloroacetylchloride (4.85 ml) solution in dry CH_2Cl_2 (120 ml) was added dropwise into

the mixture while stirring at that temperature. The mixture was stirred overnight at RT. The solvent was then evaporated. The residue was redissolved in $CH_3COOC_2H_5$ and extracted with H_2O three times. The organic phase was dried over $MgSO_4$, then vacuum filtered, and the filtrate was evaporated. The residue was purified by a silica-gel column in which the eluent was CH_2Cl_2. The product was collected as a white solid (90%, 4.5852g, 10.88 mmol). ^{1}H NMR (300 MHz, $CDCl_3$): δ = 7.9035 (d, J = 1.5 Hz, 2H), 7.837 (t, J = 1.5 Hz, 1H), 4.159 (s, 2H).

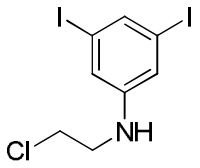

3,5-diiodo-N-[2-chloroethyl]-aniline [10]. 3,5-diiodo-N-[2-chloroethy]-anilide **9** (3.0855 g, 7.322 mmol) was dissolved in dry THF (250 ml) and cooled down to 0^{o}C. BH_3:THF (1M) (115 ml) reagent was added dropwise while the mixture was stirred at that temperature. After all had been added, the mixture was allowed to warm to RT and stirred overnight. The product was monitored by TLC. The reaction mixture was quenched with CH_3OH added dropwise. The solvent was then evaporated. The oily residue was purified by a silica-gel column in which the eluent was CH_2Cl_2/Hexanes (1:1). The product was collected as a yellow oil (68%, 2.0285 g, 4.979 mmol). ^{1}H NMR (300 MHz, $CDCl_3$): δ = 7.360 (t, J = 1.5 Hz, 1H), 6.8905 (d, J = 1.5 Hz, 2H), 4.079 (broad s, 1H), 3.662 (m, 2H), 3.418 (m, 2H).

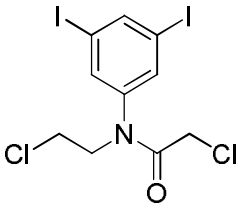

3,5-diiodo-N-[2-chloroethyl]-N-α-chloroanilide [11]. 3,5-diiodo-N-[2-chloroethyl]-aniline **10** (2.6187 g, 6.428 mmol) and $N(C_2H_5)_3$ (4.57 ml) were dissolved in dry CH_2Cl_2 (130 ml) and cooled to 0^oC. A chloroacetylchloride (2.60 ml) solution in dry CH_2Cl_2 (120 ml) was added dropwise to the mixture while was stirred at that temperature. The mixture was stirred overnight at RT. Formation of the product was checked with TLC. Some silica gel was added directly to the reaction mixture, and the solvent was evaporated to adsorb the product on silica gel. The product was purified by a silica-gel column in which the eluent was CH_2Cl_2/Hexanes (5:1). The product was obtained as brown viscous oil (90%, 2.794 g, 5.774 mmol). ^1H NMR (300 MHz, $CDCl_3$): δ = 8.104 (t, *J* = 1.5 Hz, 1H), 7.6425 (d, *J* = 1.5Hz, 2H), 3.973 (t, *J* = 6Hz, 2H), 3.826 (s, 2H), 3.652 (t, *J* = 6Hz, 2H).

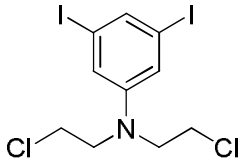

3,5-diiodo-N,N-bis-[2-chloroethyl]-aniline [12]. 3,5-diiodo-N-[2-chloroethyl]-N-α-chloroanilide **11** (3 g, 6.2 mmol) was dissolved in dry THF (250 ml) and cooled to 0^oC. BH_3:THF (1M) (100 ml) reagent was added dropwise while the mixture was stirred at that temperature. After all had been added, the mixture was allowed to warm to RT and stirred overnight. The product was monitored by TLC. The reaction mixture was quenched with CH_3OH added dropwise. The solvent was evaporated, and the oily residue was purified by a silica-gel column in which the eluent was Hexanes/CH_2Cl_2 (3:1). The product was obtained as white crystals (69%, 2.0102 g, 4.278 mmol). ^1H NMR (300 MHz, $CDCl_3$): δ = 7.403 (t, *J* = 0.9 Hz, 1H), 6.9155 (d, *J* = 0.9Hz, 2H), 3.632 (symmetric multiplet, 8H). Only one journal article had reported this compound

previously, in which the compound was supported only by elemental analysis data.[101] ^{1}H NMR data is being reported for the first time.

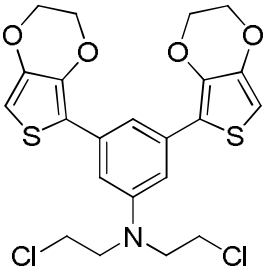

3,5-bis-(3,4-ethylenedioxythien-2-yl)-N,N-bis-[2-chloroethyl]-aniline [13]. 3,5-diiodo-N,N-bis-[2-chloroethyl]-aniline **12** (47.9 mg, 0.102 mmol), $PdCl_2(PPh_3)_2$ (3.7 mg, 0.005271 mmol), and 5-tributylstannyl-EDOT (132.9 mg, 0.3082 mmol) were placed in a microwave reactor tube (8 ml tube) with a small stirring bar added. The tube was sealed, and 4 ml of dry DMF was cannula-transferred. The mixture was sparged with Ar gas for about 5 min. Then, the mixture was placed into the reactor and irradiated with microwaves for 45 min at 105 ^oC. After the reaction was completed, CH_2Cl_2 was added into the mixture, and the organic phase was extracted with saturated NH_4Cl solution three times. The organic phase was dried over $MgSO_4$ and vacuum filtered, and the filtrate was evaporated. The residue was redissolved in $CH_3COOC_2H_5$ (~50 ml), and 40 ml of 10% KF solution was added. After about 1 hr of stirring, the precipitate was filtered off. The filtrate was transferred into the separatory funnel, and the aqueous phase was separated. The organic phase was washed with fresh H_2O twice, dried over $MgSO_4$, and vacuum filtered, and the filtrate was evaporated. The residue was purified by a silica gel column in which the eluent was CH_2Cl_2/Hexanes (1:1) to afford a yellow solid (52%, 26.42 mg, 0.053 mmol). ^{1}H NMR (300 MHz, $CDCl_3$): δ = 7.269 (t, J = 1.2Hz, 1H), 7.012 (d, J =

1.2Hz, 2H), 6.286 (s, aromatic 2Hs of EDOT), 4.266 (symmetric m, 8Hs of EDOT), 3.714 (symmetric m, 8Hs of ethyl chloride group).

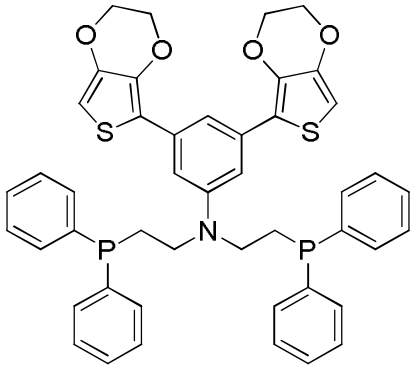

3,5-bis-(3,4-ethylenedioxythien-2-yl)-N,N-bis-[2-diphenylphosphinoethyl]-aniline [14] ($EDOT_2PNP$). 3,5-bis-EDOT-N,N-bis[2-chloroethyl]aniline **13** (100 mg, 0.201 mmol) was dissolved in dry THF in a Schlenk flask under a Schlenk line. 3.25 mL of 0.5M $KPPh_2$ was added via a glass syringe under N_2. The orange mixture was stirred for an hour. The mixture was then taken into the glove box, and filtered through a frit in which there were layers of celite/silica gel/celite. The filtrate was collected into another Schlenk flask, and the solvent was evaporated under the Schlenk line. The residue was transferred back into the glove box where it was dissolved in a minimal amount of CH_2Cl_2, and then copious layer of hexane was layered. The Schlenk flask was placed into the freezer (- 30^oC) to precipitate the product for a week. The precipitate was decanted, washed with diethyl ether, and dried under the Schlenk line to afford a yellow product (76%, 121.66 mg, 0.152 mmol): mp 66.7 ^oC; ^1H NMR (300 MHz, $CDCl_3$): δ = 7.43-7.30 (m, 20H), 7.26 (s, 1H), 6.91 (s, 2H), 6.30 (d, 2H, J = 2.1 Hz), 4.21 (s, 8H), 3.42 (dt, 4H, J_d = 8.1 Hz, J_t = 7.5 Hz), 2.39 (t, 4H, J = 8.7 Hz). $^{31}P\{^1H\}$ NMR (121 MHz, $CDCl_3$): δ = -18.11 (s). $^{13}C\{^1H\}$ NMR (75 MHz, CD_2Cl_2): δ = 147.63 (s), 142.68 (s), 138.79 (s), 138.62 (s), 134.49 (s), 132.94 (d, J = 18.6 Hz), 128.91 (t, J = 6.83 Hz), 118.90 (s), 112.91

(s), 109.77 (s), 97.64 (s), 97.54 (s), 65.03 (d, *J* = 18.075 Hz), 48.75 (d, *J* = 25.125 Hz), 26.27 (d, *J* = 14.775 Hz), 15.49 (s). HRMS (CI+) calculated for [M+H]+: 798.2, found 798.2022.

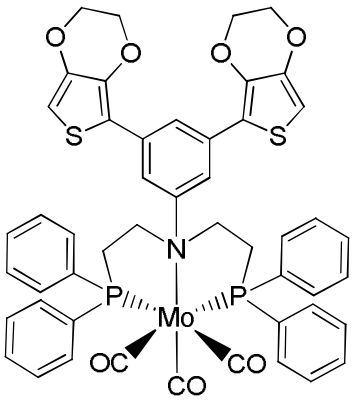

3,5-bis-(3,4-ethylenedioxythien-2-yl)-N,N-bis-[2-diphenylphosphinoethyl]-aniline-tricarbonylmolybdenum [15] (EDOT2PNP-Mo(CO)3). 3,5-bis-EDOT-N,N-bis[2-diphenylphosphinoethyl]aniline **14** (50 mg, 0.0627 mmol) was dissolved in dry THF/CH_2Cl_2 (3:1) in the glove box. CHT-$Mo(CO)_3$ (17 mg, 0.0625 mmol) was added into the solution and stirred overnight. The solvent was evaporated under Schlenk line. The residue was dissolved in CH_2Cl_2 (filtered through alumina prior to use, to get rid of any HCl formed in the solution) in the glove box, and hexanes were added to precipitate the product. The precipitate was collected and dried (63%, 38.6 mg, 0.0395 mmol): mp 172-175^{o}C (decomposed); $^{31}P\{^{1}H\}$ NMR (121 MHz, CD_2Cl_2): δ = 39.75 (s); ^{1}H NMR (300 MHz, CD_2Cl_2): δ = 7.49–7.36 (m, 21 H), 6.98 (s, 2H), 6.30 (s, 2H), 4.26 - 4.18 (m, 8H), 3.63 (bs, 4H), 2.81 (bs, 4H); HRMS (ESI) calculated for 979.09 found 979.078; Both solution state and solid state IR data were obtained; Solid state IR (ATR): 1926 cm^{-1}, 1832 cm^{-1}, 1799 cm^{-1}; Solution state IR (solution in CH_2Cl_2): 1936 cm^{-1}, 1834 cm^{-1},

1793 cm^{-1}; Raman Spectrum could not be obtained because it resulted in fluorescence of the complex; crystal structure was obtained and will be discussed in the next section.

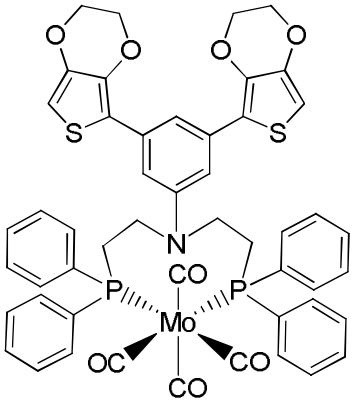

3,5-bis-(3,4-ethylenedioxythien-2-yl)-N,N-bis-[2-diphenylphosphinoethyl]-aniline-tetracarbonylmolybdenum [16] ($EDOT_2PNP$-$Mo(CO)_4$). 3,5-bis-EDOT-N,N-bis[2-diphenylphosphinoethyl]aniline **14** (49 mg, 0.0614 mmol) was dissolved in dry CH_2Cl_2 in the glove box. NBD-$Mo(CO)_4$ was dissolved in dry THF, and then the metal solution was added to the ligand solution, and the mixture was stirred in the glove box overnight. The solvent was evaporated under a Schlenk line. The residue was transferred back into the glove box, where it was redissolved by a minimal amount of CH_2Cl_2 (filtered through alumina prior to use, to get rid of any HCl formed in the solution) and then hexanes were layered on the solution to precipitate the product. The precipitate was collected by celite filtration, then redissolved by CH_2Cl_2, and the resulting solution was collected into a Schlenk flask. The solvent was evaporated to afford a yellow solid (68%, 61.8 mg, 0.0614mmol): mp 185-187^oC (decomposed); $^{31}P\{^1H\}$ NMR (121 MHz, CD_2Cl_2): δ = 22.92 (s); ^1H NMR (300 MHz, CD_2Cl_2): δ = 7.52 – 7.35 (m, 20 H), 7.27 (s, 1H), 6.63 (s, 2H), 6.31 (s, 2H), 4.26 - 4.21 (m, 8H), 3.51 (d, 4H, J = 10.2 Hz), 2.74 (bs, 4H); HRMS (ESI) calculated for 1005.08 found 1005.88; Both solution state and solid state IR data

were obtained. Solid state IR (ATR): 2030 cm^{-1}, 1900 cm^{-1} (broad, combination of 3 peaks); Solution state IR (solution in CH_2Cl_2): 2018 cm^{-1}, 1945 cm^{-1} (shoulder), 1921 cm^{-1} (peaks at 1945 and 1921 cm^{-1} are combined as a broad peak with shoulder), 1897 cm^{-1}; Raman Spectrum could not be obtained because it resulted in fluorescence of the complex.

RESULTS AND DISCUSSION

Synthesis

The PNP ligand with polymerizable EDOT groups was synthesized via an eight-step organic synthesis in which five of the organic compounds (**9**, **10**, **11**, **13** and **14**) are new (**Scheme 3**). **12** was reported once with elemental analysis data only and we report the ^{1}H NMR data for the first time.[101] The ligand **14** was reacted with CHT-$Mo(CO)_3$ and NBD-$Mo(CO)_4$ to obtain the corresponding metal complexes as monomers in which molybdenum tricarbonyl and tetracarbonyl are bound to the PNP ligand in *facial* and *cis* fashion respectively (**Scheme 4**). The monomer metal complexes **15** and **16** are characterized by solid state IR (ATR), solution state IR, ^{1}H, ^{31}P NMR spectra and HRMS. Crystal structure data of only complex **15** were obtained.

Scheme 3. Reagents and conditions: a) i. $NaNO_2$, H_2SO_4, 0^oC, 2 hrs ii. $CuSO_4 \bullet 5H_2O$, EtOH, reflux, 2hrs; b) $SnCl_2 \bullet 2H_2O$, $NaBH_4$, EtOH, reflux, 30 min; c) Chloroacetylchloride, NEt_3, CH_2Cl_2, $0^oC \rightarrow RT$, 12 hrs; d) BH_3:THF, $0^oC \rightarrow RT$, 12 hrs; e) Chloroacetylchloride, NEt_3, CH_2Cl_2, $0^oC \rightarrow RT$, 12 hrs; f) BH_3:THF, $0^oC \rightarrow RT$, 12 hrs; g) 5-($SnBu_3$)-EDOT, $PdCl_2(PPh_3)_2$, DMF, 105^oC microwave, 45min; h) $KPPh_2$, THF, RT, 1 hr.

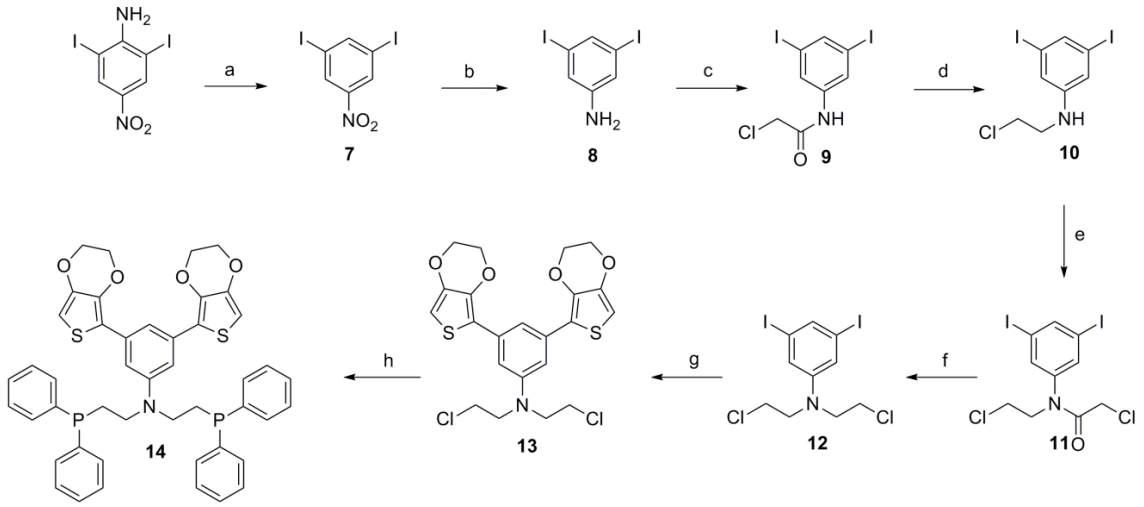

Scheme 4. Synthesis of $EDOT_2PNP\text{-}Mo(CO)_{3\text{-}4}$ complexes

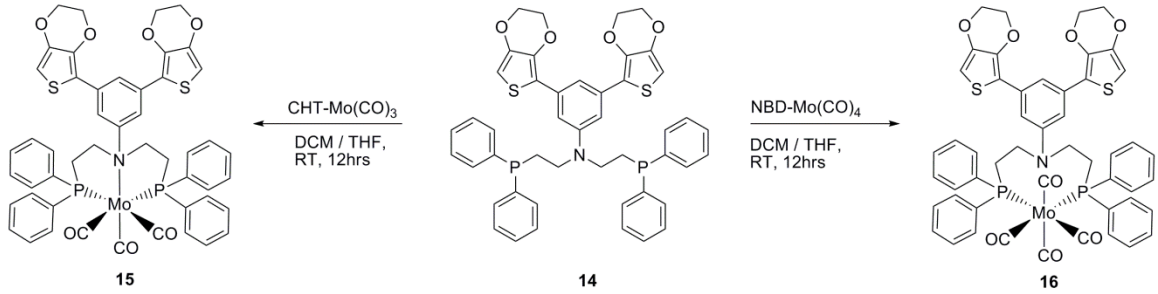

Spectroscopic Properties of Monomer Complexes

Complexes **15** and **16** are soluble in CH_2Cl_2. Solution and solid state IR data were obtained; however, Raman spectra could not be measured because the Raman beam resulted in fluorescence of the samples. The point group of the complex **15** is determined to be is C_s from its crystal structure (**Figure 25**). We do not have the crystal structure for compound **16**, but we determined that it, too, was of point group C_s by comparison with a similar complex in the literature. Based on the point group C_s, group theory calculations of CO stretches for the complexes resulted as follows: $\Gamma = 3A' + A''$ for complex **16** and $\Gamma = 2A' + A''$ for complex **15**. All bands are both Raman and IR active and coincident.

Both solid and solution state IR spectra of **15** resulted in three bands as expected from the calculation; however, there is an additional small peak at 2018 cm^{-1} and a shoulder at 1900 cm^{-1}; these values may come from the other parts of the molecule (non-carbonyl stretches) (**Figure 24a**). Solid state IR spectrum of complex **16** gave two bands (one of them broad) in the measurements; on the other hand, calculation predicts four stretches. The broad peak at 1900 cm^{-1} must be a combination of three peaks (**Figure 24b**). The solution state IR spectrum of **16** shows three stretches (2018 to 1897 cm^{-1}), and peaks are shifted compared to the solid state IR (2030 to 1900 cm^{-1}). The solution state

IR of the complex **15** gave three peaks (1936 to 1793 cm^{-1}), there is also a shift compared to the solid state data (1925 to 1798 cm^{-1}).

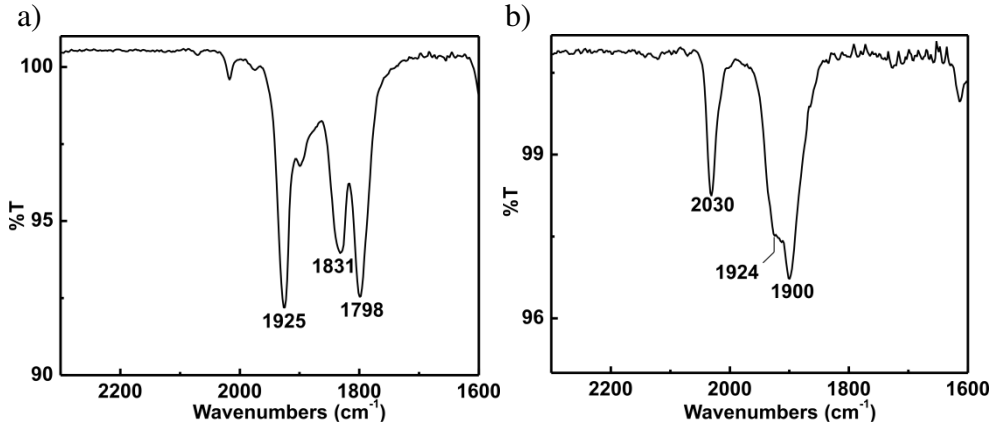

Figure 24. a) ATR-IR spectra of the monomer complex **15**; b) ATR-IR spectra of the monomer complex **16**.

Structure of Complex 15

The solid state structure of monomer **15** was determined by single crystal X-ray diffraction analysis, and the resulting ORTEP representation can be seen in **Figure 25**. Single crystals for X-ray diffraction measurement were grown by slow diffusion of hexanes into a saturated solution of **15** in CH_2Cl_2. The coordination environment around the metal center is defined by two phosphorus and one nitrogen atoms from the $EDOT_2PNP$ ligand and by three carbon atoms from CO ligands. Carbonyl ligands are in *facial* arrangement, and phosphorus atoms are in the *cis* arrangement. The geometry around the molybdenum is slightly distorted from octahedral, having Mo–P and Mo–CO distances consistent with a similar complex in the literature that is a tetracarbonyl complex of molybdenum.[64] However, because the literature compound is a tetracarbonyl

complex, carbonyls *trans* to phosphorus atoms are consistent with our complex. The other two carbonyls of the literature complex have longer M–C bonds than our complex due to the *trans* effect, and carbonyls *trans* to each other have poor π–backdonation.

Table 11. Crystal data and structure refinement of **15**.

Formula	$C_{49}H_{41}NO_7P_2MoS_2$
FW	977.83
T (K)	100(2)
Crystal system	Triclinic
Space group	*P-1*
a (Å)	8.731(5)
b (Å)	10.333(6)
c (Å)	24.709(2)
α (deg)	84.016(2)
β (deg)	87.196(2)
γ (deg)	77.568(3)
V (Å^3)	2164.2(17)
Z	2
ρ (g/cm^3)	1.500
μ (mm^{-1})	0.53
F(000)	1004
Crystal size (mm)	0.16 × 0.07 × 0.07
θ (deg)	3.0 to 27.5
Index ranges	$-10 \leq h \leq 9$
	$-12 \leq k \leq 11$
	$-29 \leq l \leq 29$
Absorption correction	Multi-scan
Max. and min. transmission	1.000 and 0.453
GOF on $F2$	1.02
$R1$, $R2$ [I > 2σ (I)]	0.1061, 0.2184
$R1$, $R2$ (all data)	0.2003, 0.2781
Largest diff. peak and hole (e.Å^{-3})	0.89 and -1.01

Table 12. Selected bond lengths (Å) and angles (deg) of **15**.

Bond Lengths (Å)	
Mo – C(1)	1.910(10)
Mo – C(2)	1.990(10)
Mo – C(3)	1.980(10)
Mo – N	2.512(9)
Mo – P(1)	2.501(3)
Mo – P(2)	2.515(3)
Bond Angles (^{o})	
C(1) – Mo – C(2)	88.3(5)
C(1) – Mo – C(3)	90.1(5)
C(1) – Mo – N	170.6(4)
C(1) – Mo – P(1)	93.8(4)
C(1) – Mo – P(2)	97.9(4)
C(2) – Mo – C(3)	83.5(5)
C(2) – Mo – N	96.0(4)
C(2) – Mo – P(1)	88.3(4)
C(2) – Mo – P(2)	172.6(4)
C(3) – Mo – N	98.7(4)
C(3) – Mo – P(1)	170.9(4)
C(3) – Mo – P(2)	92.4(4)
N – Mo – P(1)	78.0(2)
N – Mo – P(2)	78.5(2)
P(1) – Mo – P(2)	95.2(1)
O(1) – C(1) – Mo	179(1)
O(2) – C(2) – Mo	173(1)
O(3) – C(3) – Mo	175(1)

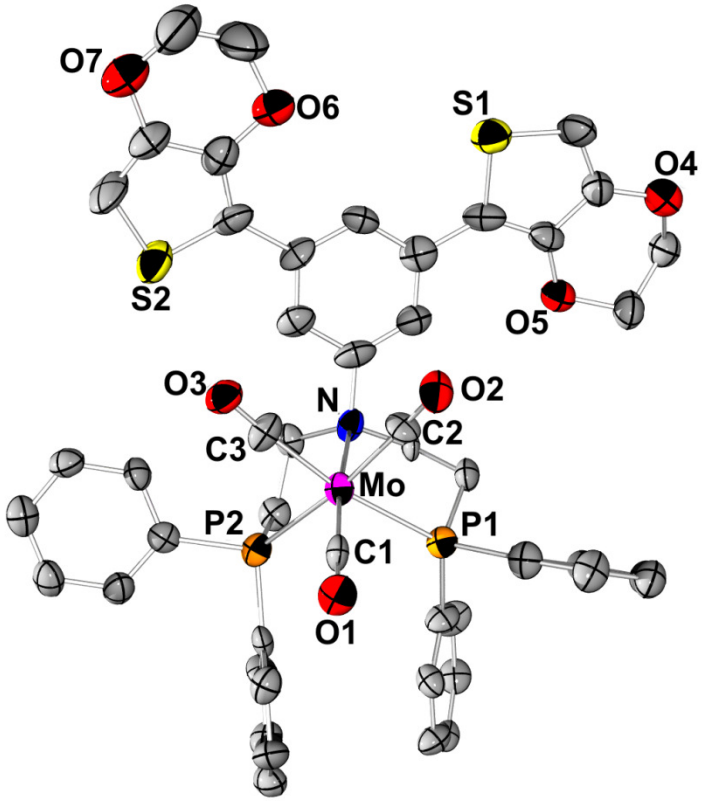

Figure 25. Crystal structure of the monomer complex **15** showing the labeling of selected atoms. Hydrogen atoms have been omitted for clarity. Displacement ellipsoids are scaled to the 50% probability level.

Electrochemistry and Electropolymerization

Monomers **14**, **15**, and **16** were electropolymerized to form **poly-14**, **poly-15**, and **poly-16** on a working electrode, which is a platinum button, to obtain a polymerization profile by applying a potential throughout the solution containing the electrolyte (0.1M $TBAPF_6$ in CH_2Cl_2) and the monomers. Polymers are reddish-brown in color. Growth of a polymer film in all three monomers is indicated by a sequential growth in current.[3, 102] The polymerization profiles and the scan rate dependence of the polymerization processes, which are very similar to each other, are shown in **Figures 26-28**. First scans

are shown in red; all other scans are black in the graphs. Insets of **Figures 26-28** of polymerization profiles show a linear relationship between the current and the number of scans during polymerization. **Poly-14** indicates a uniform growth of the polymer up to 14 scans, after which the graph levels off. **Poly-15** and **poly-16**, however, show a uniform growth up to 20 scans.

The first scan in the polymerization of ligand **14** started with an oxidation at 0.41 V and 0.81V whose positions became more positive with increasing scans. Reduction occurs at 0.25 V (**Figure 26 a**). Kvarnstrom *et al.* reported oxidation of EDOT as 1.1 V vs. Ag / AgCl. The peak at 0.81 V may belong to monomer oxidation.

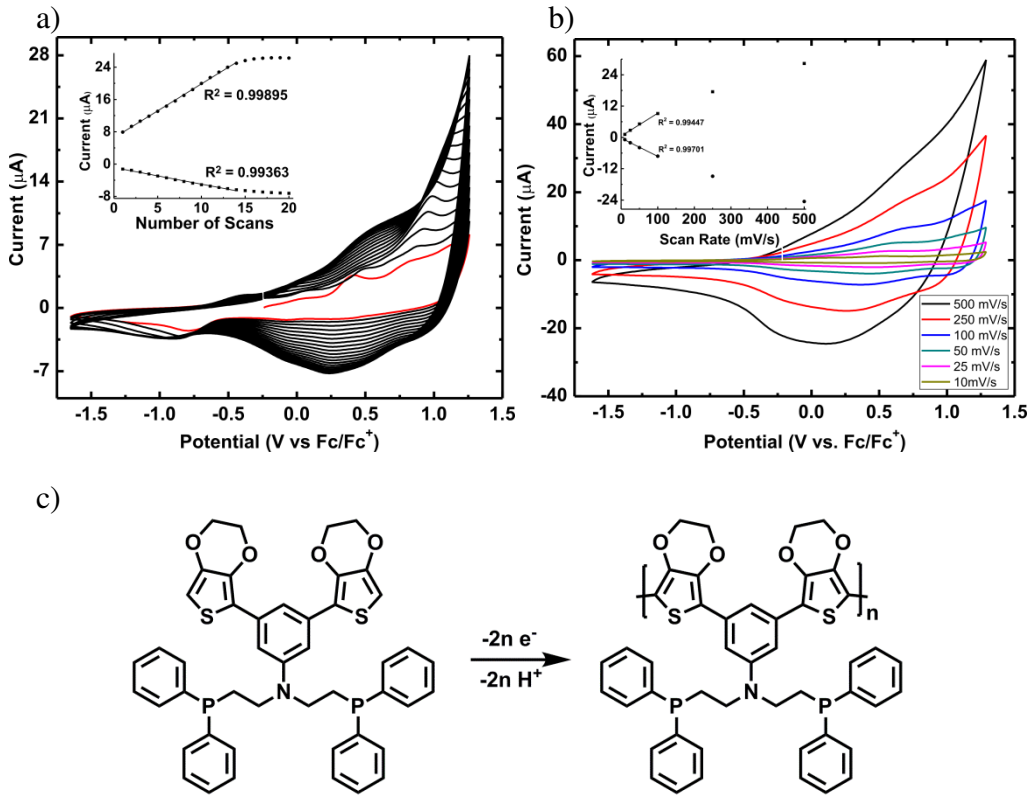

Figure 26. a) Polymerization profile b) scan rate dependence c) polymerization process for **poly-14**.

The first scan of **15** started with an oxidation peak at around -0.07 V and 0.43 V (**Figure 27 a**). The peak at 0.43 V became more and more positive in subsequent scans. An irreversible reduction took place at around -0.85 V.

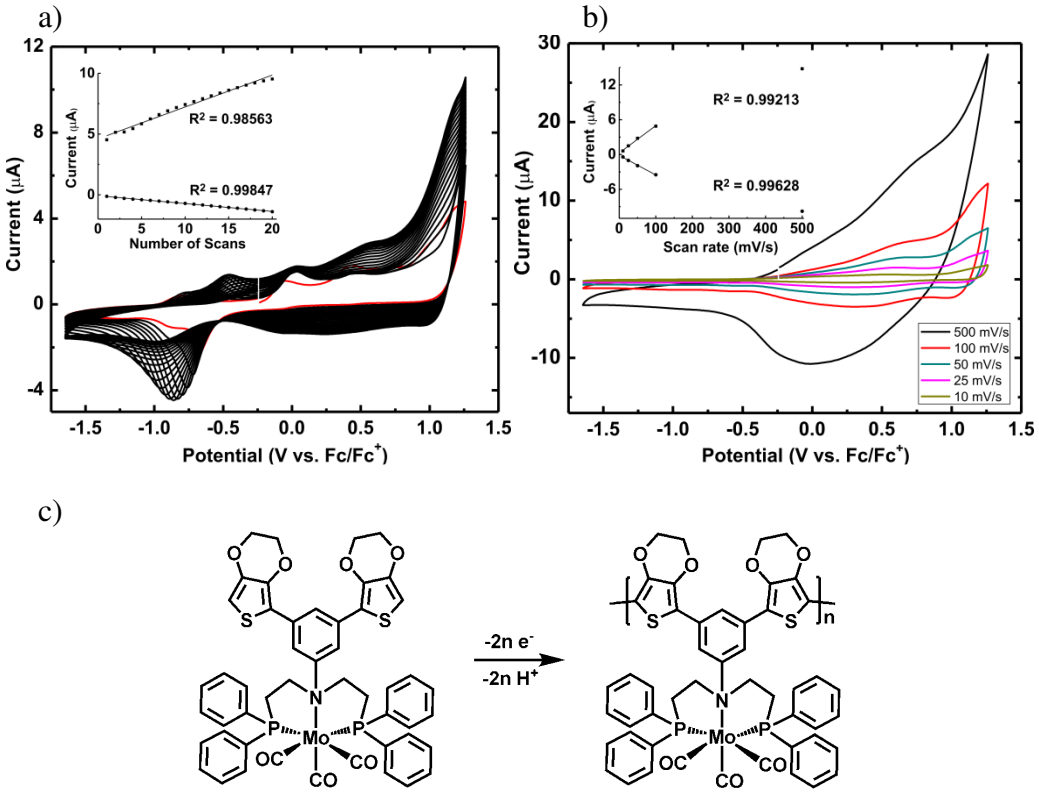

Figure 27. a) Polymerization profile b) scan rate dependence c) polymerization process for **poly-15**.

First scan of **16** started with an oxidation peak at around 0.1 V, 0.43 V, and 0.73 V (**Figure 28 a**). The latter two peaks were not observed in subsequent scans. A peak appeared in the second scan at 1 V and became more and more positive in the following scans, most likely due to polymer oxidation. Compared to the electropolymerization of

15, that peak is much clearer in electropolymerization of **16**. Again in this case, an irreversible reduction occurred around -0.85 V.

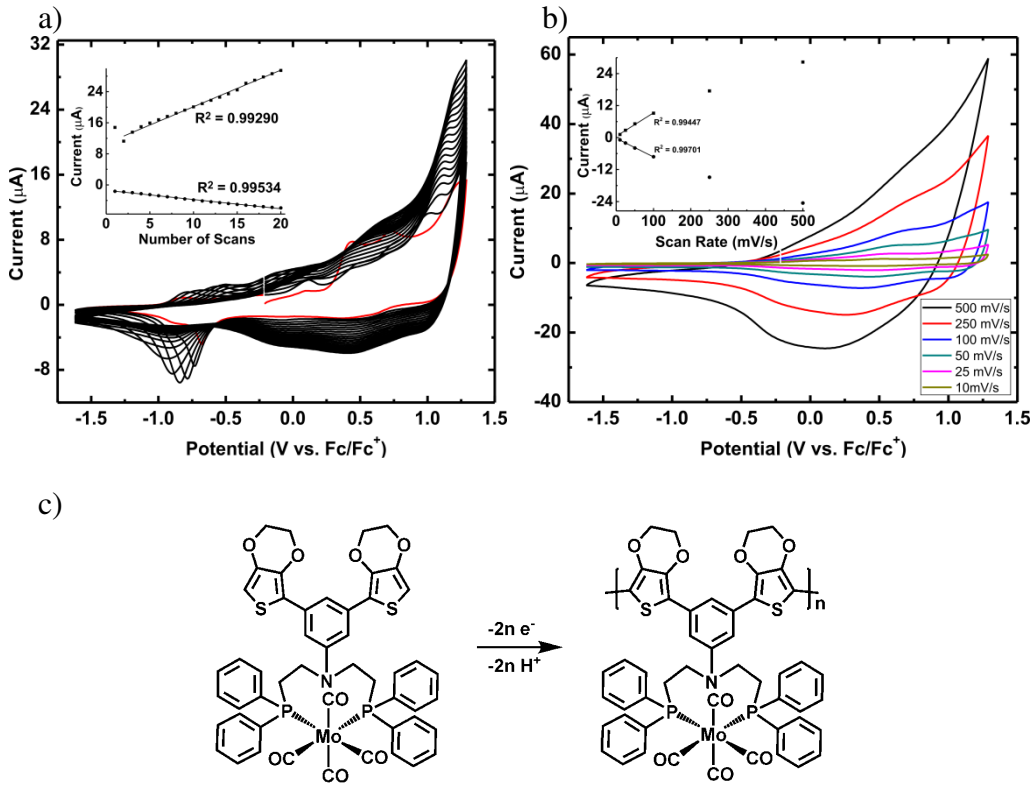

Figure 28. a) Polymerization profile b) scan rate dependence c) polymerization process for **poly-16**.

ITO-coated glass was used as the working electrode for IR studies and X-ray photoelectron spectroscopy (XPS) analysis. IR studies showed no carbonyl stretch whatsoever. The results are discussed in the section titled "Spectroscopic Properties of Polymers".

An irreversible reduction around -0.85 V can be seen for both **poly-15** and **poly-16** in **Figures 27, 28**. Electropolymerization was performed by using complex **15** in a narrower window to see the resulting polymer without this reduction, to show either the

presence of the absence of a carbonyl stretch in the IR (**Figure 29**); this was done to test whether the carbonyl loss was due to that reduction. Unfortunately, the IR spectrum of the corresponding polymer did not have the carbonyl stretches, demonstrating that the reduction was not the cause of the lost of carbonyl.

Polymerizations of complexes **15** and **16** done in $TBAPF_6$ might result in a lost of CO, because in some cases PF_6^- causes HF production in the electrochemistry solution,[103] and the complexes are most likely not stable in the acidic media. Therefore, polymerization of **15** attempted also in $TBAClO_4$. Surprisingly, the monomer did not polymerize as shown by a decrease in initial current. A brown residue was observed on the ITO-coated glass working electrode. ClO_4^- may cause dissociation of the complex. The residue was analyzed with XPS (**Figure 31 e**) which showed that the molybdenum was partially oxidized.

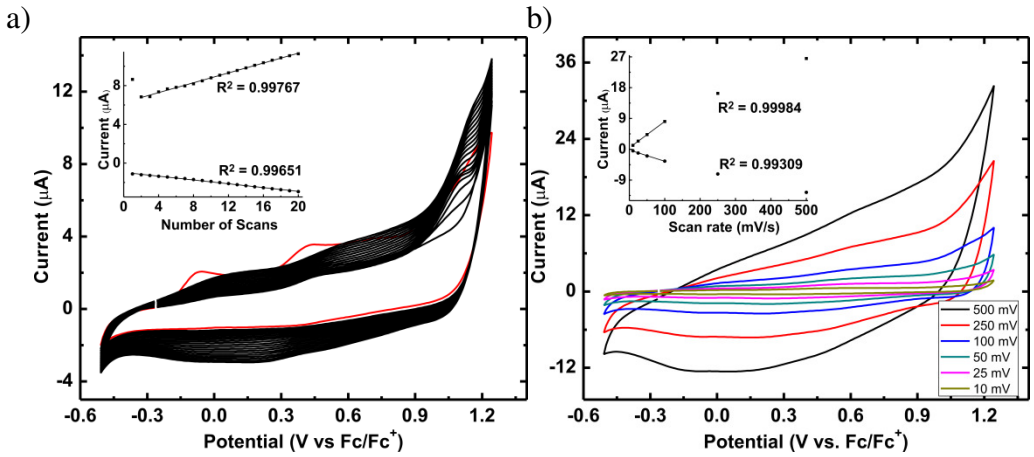

Figure 29. a) Polymerization profile b) scan rate of **poly-15** in a narrow window.

CV data of non-polymerizable model complexes of PNP-$Mo(CO)_n$ n=3,4 were obtained to find Mo^0/Mo^{n+} and compared with similar complexes in the literature to see if

the oxidation is in the polymerization window and therefore can affect the carbonyl loss. Mo^0/Mo^+ oxidation is found to be -0.116 V, which is in the CV window for the polymerization (-1.65 to +1.29V vs Fc/Fc^+ in **Figure 27** and also -0.51 to 1.24V vs Fc/Fc^+ in **Figure 29**), and the literature value of a similar complex is 0.04 V[104] (**Figure 30**). Oxidation of Mo^0 might therefore play a role in carbonyl loss during electropolymerization.

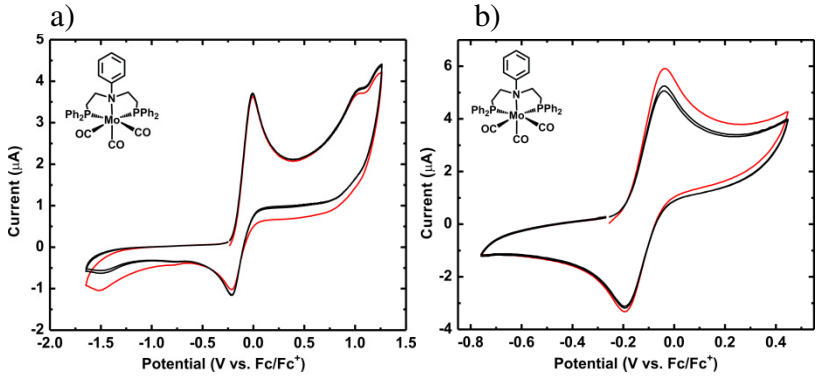

Figure 30. CV data of the model complex PNP-$Mo(CO)_3$.

Characterization of Polymers

XPS and scan-rate dependence were the characterization techniques used for the metallopolymers. XPS data were used to determine the elemental composition of the polymer through survey scans of the film. Polymers were deposited on ITO surfaces for XPS studies. Quantitative XPS analysis of **poly-15** shows that the film has an atomic ratio of molybdenum:sulfur = 1:2.309 and molybdenum:phosphorus = 1:2.049, consistent with the stoichiometric molar ratio proposed for the film structure, 1:2. However, the molybdenum:nitrogen ratio is 1:4.13, compared with a proposed ratio is of 1:1. The extra nitrogen atoms most likely come from the electrolyte, which contains the tetrabutylammonium (TBA) cation, although the polymers were rinsed with CH_2Cl_2 after

the polymerization process. Some TBA^+ must have remained in the polymer, inaccessible to the rinsing solvent. Scan rate dependence is quite linear up to 100 mV for the polymerization processes.

The oxidation states of the molybdenum atoms in both monomers and polymers were determined by high resolution XPS and peak extrapolation of the data (**Figure 31**). Monomers have a zero oxidation state, and polymers are mostly oxidized to +6.[105]

Scan rate dependence is quite linear up to 100 mV for both polymerization processes, indicating that a strongly adsorbed electroactive material is not limited by the ionic flux of counter ions. Because there is a decrease in charge mobility through the polymer backbone at higher scan rates, less facile ion transport and a deviation from the linear relationship occurs.

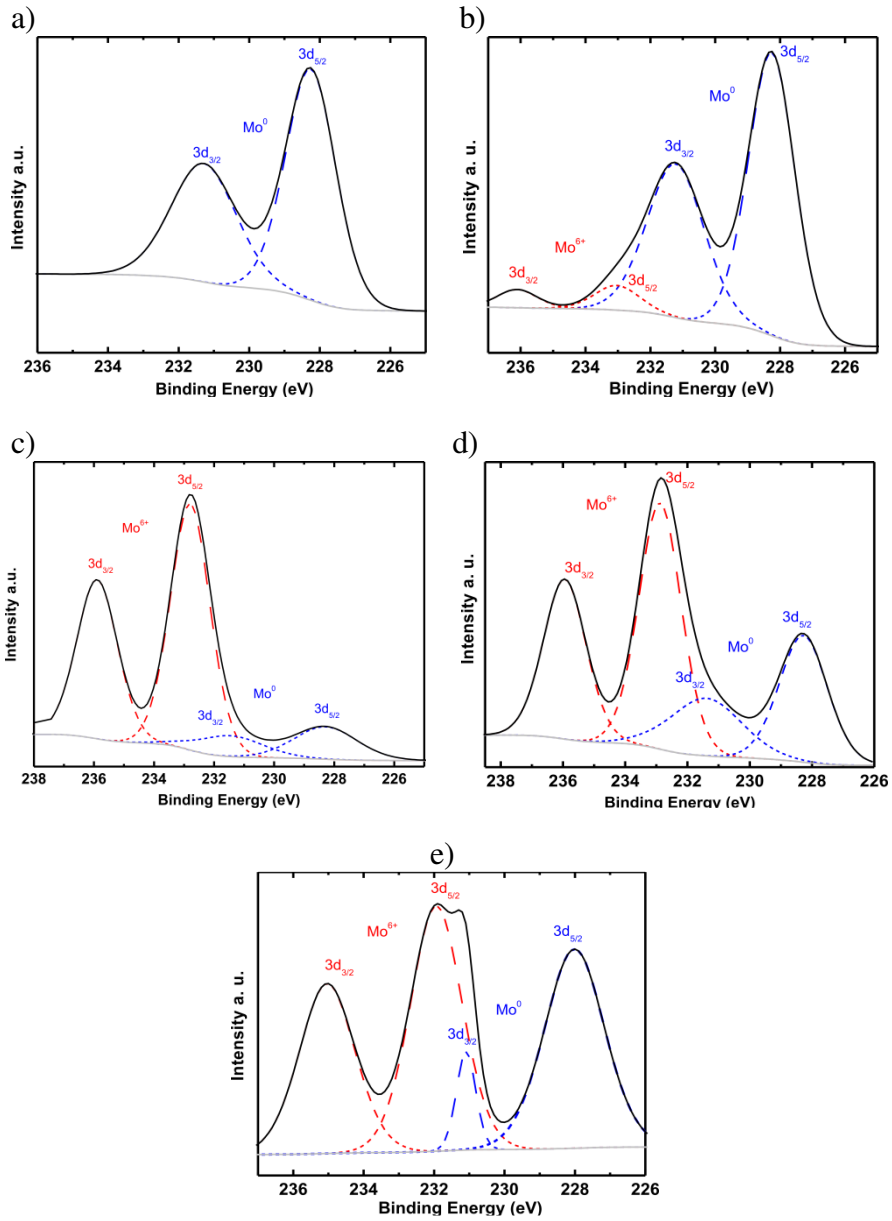

Figure 31. High resolution XPS data (solid line) and peak fitting technique (dashed and dotted lines). a) **15** b) **16** c) **poly-15** d) **poly 16** e) attempt to make **poly 15** in $TBAClO_4$.

Spectroscopic Properties of Polymers

In order to measure the carbonyl stretches in the polymers, specular reflectance IR, ATR-IR, and KBr pellet methods were employed. We could polymerize the complex by using $TBAPF_6$ as the electrolyte, on different surfaces such as Au-Cr on glass (for specular reflectance IR), Au-Ag-InO_3 on plastic (for ATR-IR), and indium tin oxide (ITO) to observe the carbonyl peaks in IR spectrum. The first method we tried was specular reflectance IR, which did not show any CO stretches. Then, the monomers were polymerized on a plastic surface coated with Au-Ag-InO_3. The ATR-IR measurement was performed by placing the polymer on the plastic substrate directly onto the ATR apparatus. Again, no carbonyl stretches were observed. The last method employed was to isolate the polymer film from the substrate (working electrode) and measure the solid state IR data of the polymer film directly. After polymerizing the monomer on the ITO surface, the polymer was collected and separated by a razor blade from the ITO surface, and the ATR-IR spectrum of the collected film was obtained. The polymer film was also blended with some KBr (approximately 10 times more of the sample weight) to make a pellet for IR measurement. Unfortunately, none of the IR techniques showed carbonyl stretches, whereas the IR spectra of the monomers do.

The polymers on Au-Cr surface and Au-Ag-InO_3 were tried to be loaded with CO gas. Polymers on these surfaces placed in a vial separately and covered by a septum. Then CO gas was blown for 5 min then polymers were left under positive pressure of CO gas for 30 min. IR measurements were done. Again no CO stretch was found. Also polymers were soaked in CH_2Cl_2 in a vial covered by a septum. CO gas was bubbled for 5 min., and then the polymers were left under positive pressure of CO gas for 1 hour. IR measurement showed no CO stretch.

The carbonyl ligands must be dissociated during polymerization in which the molybdenum in the polymer is oxidized, because the oxidized Mo will not be able to donate its electrons to the carbonyls for π-backdonation. In order to prove this to be the case, we analyzed the high resolution XPS data of the monomers **15**, **16** and polymers **poly-15**, **poly-16** to find the oxidation state of the Mo. The monomer complexes **15** and **16** contain Mo^0, i.e. complex **16** contains 92.3% Mo^0 and 7.7% Mo^{6+}. The polymers have mostly Mo^{6+} and some Mo^0 (**Figure 31**). Mo^0 has a binding energy value for 3d5/2 at 228 eV and 3d3/2 at 231 eV. Mo^{6+}, on the other hand, has 3d5/2 at 232.5 eV and 3d3/2 at 236 eV as reported in the literature.[105] XPS data prove that some of the Mo atoms on the polymer have been permanently oxidized.

CONCLUSIONS

We report synthesis and characterization of a novel polymerizable ligand **14** and corresponding molybdenum complexes **15** and **16** with this ligand. Both the ligand and the complexes are electropolymerizable.

The monomer complexes have carbonyl stretches in their IR spectra; on the other hand, the corresponding polymers show no carbonyl stretches in any of the IR techniques used. The first oxidation of Mo in CV data is found in the polymerization window. Carbonyl ligands must be lost during the electropolymerization process. Polymers also exposed to CO, but did not take up the gas. Presence of PF_6^- anion may also have a role in carbonyl release by causing HF formation in the electrolyte. Monomer complexes may not be stable in the media that have HF.

XPS analysis was performed on both monomers and polymers to further investigate the situation. The XPS result of the oxidation state of Mo atoms showed that

monomer complexes have Mo^0 atoms and polymers have Mo atoms mostly oxidized. During the oxidation of Mo, carbonyl ligands must have been released due to lack of electrons on Mo for π-backdonation. In fact, changing the oxidation state of the metal through use of a redox active ligand caused the release of the carbonyls permanently.

Future efforts will focus on controlled release of carbonyl ligands by preparing metal complexes of the electropolymerizable PNP ligand, which have metal oxidation outside the polymerization window. Therefore, when potential is applied to the complex, the carbonyl stretch in IR spectra can be studied for a controlled release. Since nitric oxide is isoelectronic and a similar molecule to carbonmonooxide, electropolymerizable complexes with nitrosonium analogues of the molybdenum polymers may also be prepared and nitric oxide release can be probed with IR spectroscopy. It should be noted that controlled release of nitric oxide would likely have clinical significance to implant applications.[106]

Chapter 4: Polymerizable 2,6-bis(pyrazolyl)pyridine Complexes of Ruthenium

INTRODUCTION

$Ru(bpy)_3Cl_2$ has been thoroughly studied and frequently employed due to its unique properties, such as chemical stability, luminescence emission and excited state lifetime, redox properties, and excited state reactivity.[53] This red crystalline salt is obtained as the hexahydrate from the reaction of an aqueous solution of ruthenium trichloride with 2,2'-bipyridine. Ru(III) is reduced to Ru(II) in the process by hypophosphorous acid.[107] The complex is a chiral, d^6 system with D_3 symmetry, and its enantiomers are kinetically stable. All of the properties of interest are in the cation $[Ru(bipy)_3]^{2+}$, which has a noteworthy chemical stability as it can be stored in aqueous solutions for months; furthermore, it is unaffected by boiling in concentrated HCl or 50% aqueous NaOH solutions.[108,109] Excited solutions of the cation emit light both at room temperature (890 ns in CH_3CN, 650 ns in H_2O) and at 77 K (5 μs) with relatively long lifetimes.[53, 110] When Ru (II)–polypyridine complexes undergo one electron oxidation, the process involves a metal centered orbital with the formation of Ru(III) complexes, which have a low spin $4d^5$ configuration and are inert to ligand substitution.[111] Single electron reduction of Ru (II) – polypyridine complexes generally takes place on a ligand orbital, depending on either a sufficiently strong ligand field or easily reducible ligands. The reduced form in this case has a low spin $4d^6$ configuration and is usually quite inert.[112] Both single electron oxidation and reduction are reversible processes. The triplet excited state of $Ru(bipy)_3^{2+}$ has both oxidizing and reducing properties. This remarkable situation arises because the excited state can be described as a Ru^{3+} complex containing a $bipy^-$ ligand.[113] $Ru(bipy)_3^{2+}$ has been examined as a photosensitizer for both the oxidation and reduction of water.[114]

The excited states of Ru (II) – polypyridine complexes may involve three types of electronic transitions (**Figure 32a**).[13, 115] Polypyridine molecules possess σ–donor orbitals localized on the nitrogen atoms and π–acceptor orbitals delocalized on aromatic rings. Promotion of an electron from a π_M metal orbital to π^*_L ligand orbitals results in metal-to-ligand charge transfer (MLCT) excited states, while promotion of an electron from π_M to σ^*_M orbitals leads to metal centered (MC) excited states. Promotion of an electron from π_L to π^*_L generates ligand centered (LC) excited states. Presence of the heavy ruthenium atom causes spin-orbit coupling which leads to singlet-triplet mixing in the MC and MLCT excited states.[13, 115] Homotrischelated complexes of ruthenium with bidentate polypyridine ligands exhibit a D_3 symmetry; corresponding orbitals involved in electronic transitions are shown in **Figure 32b**.[53, 116]

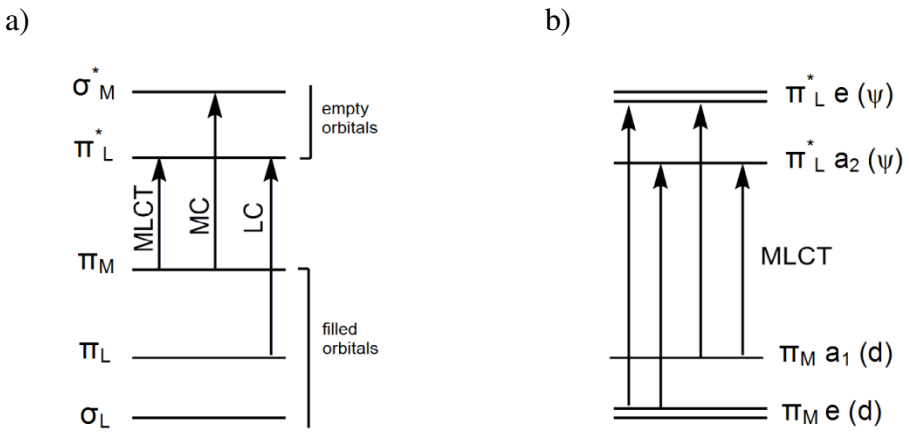

Figure 32. a) Molecular orbital diagram for $Ru(LL)_3^{2+}$ showing types of electronic transitions occurring b) detailed representation of the MLCT transition in D_3 symmetry. Diagram adapted from reference [53].

Transition metal complexes in their high-energy excited states undergo fast nonradiative deactivation,[117] and therefore the lowest excited state and the states

populated according to Boltzmann equilibrium law may result in luminescence emission and in bimolecular processes. The MC excited states of d^6 octahedral complexes are strongly displaced with respect to the ground state geometry; therefore, such molecules undergo fast nonradiative deactivation or ligand dissociation reactions. Consequently, no luminescence can be observed at room temperature from the MC excited states.[118] Luminescence can generally be observed when the lowest excited states are LC and MLCT, due to their small displacement from the ground state geometry; therefore the complexes do not undergo fast nonradiative decay.

Derivatives of $[Ru(bipy)_3]^{2+}$ are numerous. Such complexes are widely discussed for possible applications in biodiagnostics, photovoltaics, and organic light-emitting diode, but no derivative has been commercialized.[53, 54] Due to their promising luminescence properties for materials applications, ruthenium (II) complexes are coordinated into the conducting polymer backbones. N-donating ligands with bidentate and tridentate coordination modes are generally used for such metallopolymers. (**Figure 33**).[55, 56, 119] Metallopolymers which contain ruthenium with thienyl groups are other examples (**Figure 34**).[9, 51, 120] Peng *et al.* reported a metallopolymer with increased photosensitivity upon incorporation of the metal complex that has a strong absorption in the visible region of the spectrum.[121] Ruthenium(II) polypyridine complexes can enhance the charge mobility of the resulting metallopolymer, and processing the material is easy.[55]

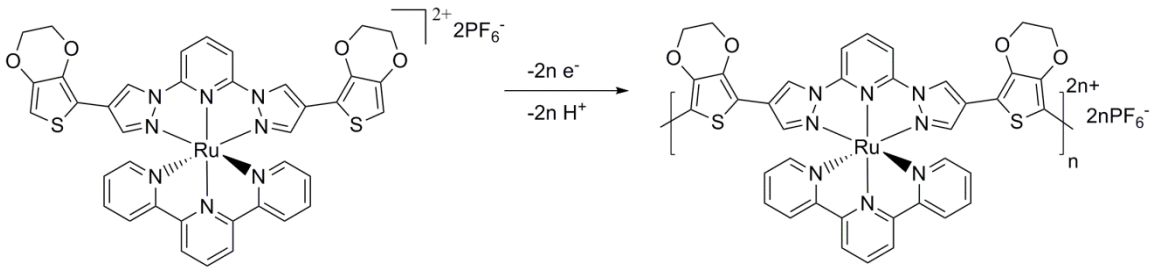

Figure 33. Electropolymerization of a ruthenium-containing polymer in which the donor atoms are N.

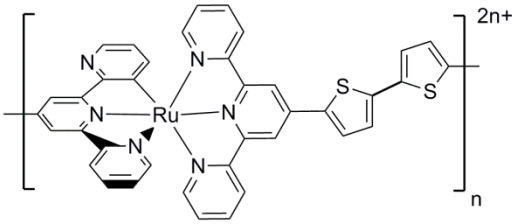

Figure 34. Ruthenium-containing rod-like conducting polymer with bithiophene units.

In this study, the syntheses and characterization of four Ru(II) complexes were reproduced after Dr. Xunjin Zhu with the polymerizable tridentate ligand Bis[4-[2-(3,4-diethylenedioxy)thiophene]pyrazol-1-yl]pyridine [119, 122] ($EDOT_2NNN$) and the following bidentate ligands 1,1,1,5,5,5-hexafluoro-2,4- pentanedione (hfac), dibenzoylmethane (dbm), 2,2'-bipyridine (bpy), 1,10- phenanthroline (phen). Then, further studies on the complexes were performed, i.e., electrochemistry/electropolymerization, UV-Vis spectroscopy of complexes and one of the polymers, luminescence studies of the monomer complexes in air free and aerated media as well as the luminescence study of one of the polymers. The reasons that we chose ruthenium polymers are ease on processibility, their chemical stability, luminescence emission and high charge carrier mobility compared to monomers as well as the electronic interactions between the

organic backbone and the ruthenium metals. In addition, having the bidentate ligands can enhance the light absorption. Possible application to these materials would be PLEDs.

EXPERIMENTAL

Instrumentation

^{1}H and $^{13}C\{^{1}H\}$ NMR spectra were recorded with a Varian 300 MHz spectrometer. ^{1}H NMR signals were referenced to residual proton resonances in deuterated solvents. $^{13}C\{^{1}H\}$ NMR spectra were referenced relative to solvent peaks. All peak positions are listed in ppm and all coupling constants are listed in Hertz (Hz). UV-Vis measurements were obtained by using a Varian Cary 6000i UV-VIS-NIR spectrophotometer. Luminescence measurements were performed by a Photon Technology International QM 4 spectrophotometer. Innovative Technology, Pure Solv solvent purifier was used to obtain dry solvents. Samples were freshly prepared prior to analysis.

Electrochemistry

GPES system from Eco. Chemie was used to carry out electrochemistry and electropolymerization experiments in the glove box with three electrodes, i.e., $Ag/AgNO_3$ as the reference electrode, Pt wire coil as the counter electrode and a Pt working electrode. For the UV-Vis and luminescence measurements of the polymers, Delta Technologies ITO coated glass was used as a working electrode instead of the Pt button. The reference electrode is made up of a Ag wire which was in a 0.01 M $AgNO_3$ solution with 0.1 M $[(n\text{-}Bu)_4N][PF_6]$ ($TBAPF_6$) in CH_3CN. Potentials measured were relative to the reference electrode which needed to be calibrated by external reference ferrocene. Calibrations were done before and after experiments were performed. The average of the ferrocene measurements was determined and used to correct the measured potentials. Solution of 0.1 M ($TBAPF_6$) in CH_2Cl_2 was used as the electrolyte. ~1 x 10^{-3} M monomer

solutions were prepared for electropolymerizations. The potential windows were between ~-1.6 V and ~1.25 V at the rate v = 100 mVs^{-1}. The polymer films were washed with dry CH_2Cl_2 in the glove box to remove any monomer or electrolyte left on the films before further experiments. $TBAPF_6$ had to be purified. Hot ethanol was used to recrystallize $TBAPF_6$ three times and then the white crystals were dried for 3 days above 100°C under active vacuum.

Synthesis

General Methods

All chemicals were purchased from commercial suppliers and were used as received. The reactions were performed by using a Schlenk line which has a nitrogen atmosphere and using dry glassware.

2-(tributylstannyl)-3,4-(ethylenedioxy)thiophene was prepared by Swager's method.[98] 2,6-Bis(N-pyrazolyl)pyridine was prepared by a similar technique that of Jameson and coworkers' (NaH and THF was used instead of K and 2-methoxyethyl ether) to afford white crystals (5.81 g, yield = 68%).[123] 2,6-Bis(4-iodopyrazol-1-yl)pyridine was prepared by Zoppellaro and coworkers' techniques as a white solid (6.173 g, yield 96%).[122, 124] 2,6-Bis[4-[2-(3,4-diethylenedioxy)thiophene]pyrazol-1-yl]pyridine was synthesized according to Zhu's technique.[119, 122] The tan precipitate was collected as 0.355 g (48% yield). ^1H NMR and $^{13}C\{^1H\}$ NMR matched with the literature value.[119] UV-Vis (CH_2Cl_2, nm (ε)): 277 (21969), 315 (24507) sh, 335 (29034). The yield and the ε value are different than those reported by Stanley.[122]

The following complexes (**17-21**) were made by Dr. Zhu (**Scheme 5**). Seyma Keskin reproduced the syntheses and confirmed by the values of ^1H NMR data (except

Bis[4-[2-(3,4-diethylenedioxy)thiophene]pyrazol-1-yl]pyridinerutheniumtrichloride (III) which is an insoluble black powder). UV-Vis data and further experiments were done by Seyma Keskin.

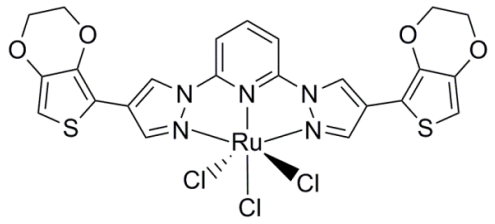

17

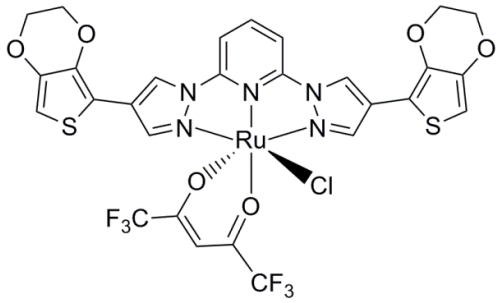

18

^{1}H NMR (400 MHz, δ ppm, CD_2Cl_2, 298 K): 8.63 (s, 2 H), 8.24 (s, 2 H), 7.64 (t, 1H, *J* = 8.4 Hz), 7.47 (d, 2H, *J* = 8Hz,), 6.34 (s, 2H), 6.10 (s, 1H), 4.26-4.34 (m, 8H). UV-Vis (CH_2Cl_2, nm (ε)): 281 (29011), 316 (21986) sh, 354 (12247), 497 (6896).

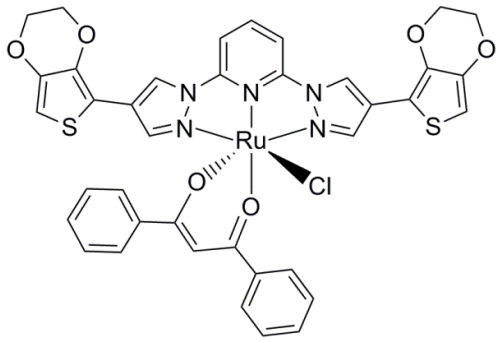

19

^{1}H NMR (400 MHz, δ ppm, CD_2Cl_2, 298 K): 8.66 (s, 2 H), 8.34 (m, 2 H), 8.11 (s, 2H), 7.51-7.62 (6H), 7.17-7.14 (m, 3H), 7.06 (t, *J* = 8 Hz, 2H), 6.64 (s, 1H), 6.26 (s, 2H), 4.19-4.29 (m, 8H). UV-Vis (CH_2Cl_2, nm (ε)): 256 (35714), 279 (38713), 326 (52803), 486 (8153).

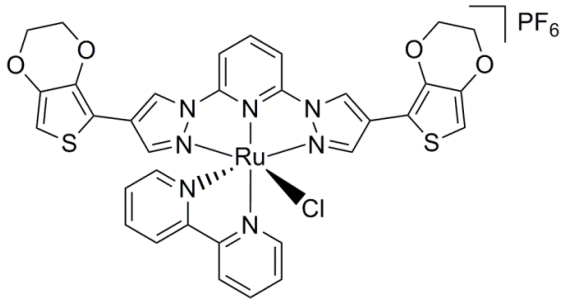

20

^{1}H NMR (400 MHz, δ ppm, CD_3CN, 298 K): 10.25 (m, 1H), 8.92 (s, 2H), 8.56 (d, *J* = 8.0 Hz, 1H), 8.32 (d, *J* = 7.6 Hz, 1H), 8.23-8.27 (m, 1H), 8.18-8.22 (m, 1H), 8.01 (d, *J* = 8Hz, 2H), 7.89-7.92 (m, 1H), 7.70-7.74 (m, 1H), 7.5 (s, 2H), 7.38 (d, *J* = 8.0 Hz, 1H), 6.96-7.00 (m, 1H), 6.35 (s, 2H), 4.17-4.25 (m, 8H). UV-Vis (CH_2Cl_2, nm (ε)): 254 (30553), 290 (66486), 355 (21887), 455 (8894), 550 (4119).

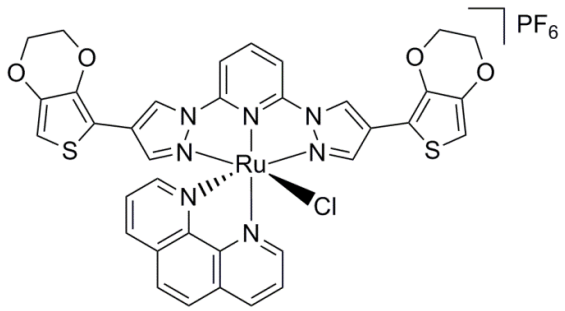

21

^{1}H NMR (400 MHz, δ ppm, CD_3CN, 298 K): 10.43 (dd, 1H), 8.90 (s, 2H), 8.78 (dd,1H), 8.23-8.29 (m, 4H), 8.04-8.08 (m, 3H), 7.74 (dd, 1H), 7.34 (s, 2H), 7.30 (dd, 1H), 6.28 (s, 2H), 4.11-4.19 (m, 8H).UV-Vis (CH_3CN, nm (ε)): 223 (53267), 265 (66997), 349 (18970), 443 (11820), 549 (4033).

RESULTS AND DISCUSSION

Synthesis

The polymerizable ligand ($EDOT_2NNN$) was prepared by Zhu's technique.[119, 122] First, the hydrogen attached to the nitrogen of pyrazole was abstracted by NaH, and then 2,6-dibromopyridine was added to give compound 2,6-Bis(N-pyrazolyl)pyridine in 68% yield. Then, 2,6-Bis(N-pyrazolyl)pyridine was symmetrically iodinated in a hot, acidic medium to afford 2,6-Bis(4-iodopyrazol-1-yl)pyridine in 96% yield. The last step was the Stille coupling of 2-(Tributylstannyl)-3,4-(ethylenedioxy)thiophene and 2,6-bis(4-iodopyrazol-1-yl)pyridine to give 2,6-Bis[4-[2-(3,4-diethylenedioxy)thiophene]pyrazol-1-yl]pyridine ($EDOT_2NNN$) in 48% yield.

Ligand ($EDOT_2NNN$) was reacted with $RuCl_3.XH_2O$ in boiling C_2H_5OH to obtain the precursor **17** as a dark insoluble powder in high yields (85 %). Then two of the chlorides on ruthenium were exchanged by the bidentate ligans (hfac, dbm, bpy and phen) to afford the ruthenium complexes **18–21 (Scheme 5)**; two of which are neutral, two of which are ionic monomer complexes. $N(CH_2CH_3)_3$ base was used to help abstraction of acidic α-hydrogen of the the diketonate ligands in the synthesis of **18** and **19**. Precursor **17** has Ru(III) metal, on the other hand, complexes **18**-**21** have Ru (II) metal. Metals were reduced during the ligand exchange reaction by oxidation of the solvent ethanol.

Scheme 5. Complex syntheses

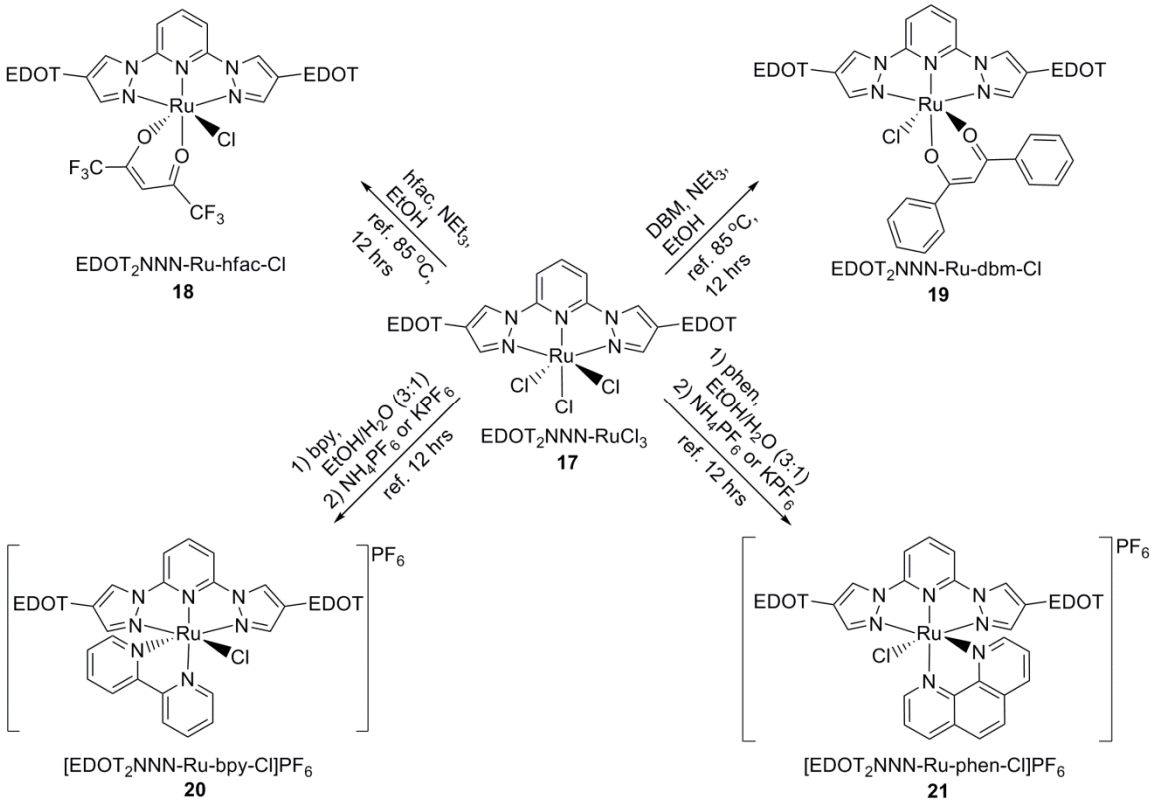

Electropolymerization of Ruthenium Complexes.

Monomers (**18**–**21**) with ~ $1x10^{-3}$M concentration were electropolymerized in the glovebox and the chemical process is shown in **Scheme 6** and related polymerization profiles of the monomer complexes are shown in **Figure 35**. Polymerization profiles of all complexes are similar to Ru(II)/Ru(III) redox couples and monomer oxidations. Although it is not practical and sufficient to compare potentials reported in the literature, it should be mentioned that Ru(II)/Ru(III) potentials of polypyridine complexes are around 1.25 V with respect to NHE (0.62V vs Fc/Fc^{+}).[53, 119, 125] Substitution of polypyridine ligands can drastically change these potentials. For example, when one of

the bpy ligands of Ru $(bpy)_3^{2+}$ is replaced by 2 Cl^- ligands, the potential is lowered by 0.35V.[53]

Scheme 6. Electropolymerization of $EDOT_2NNN$-Ru Complexes

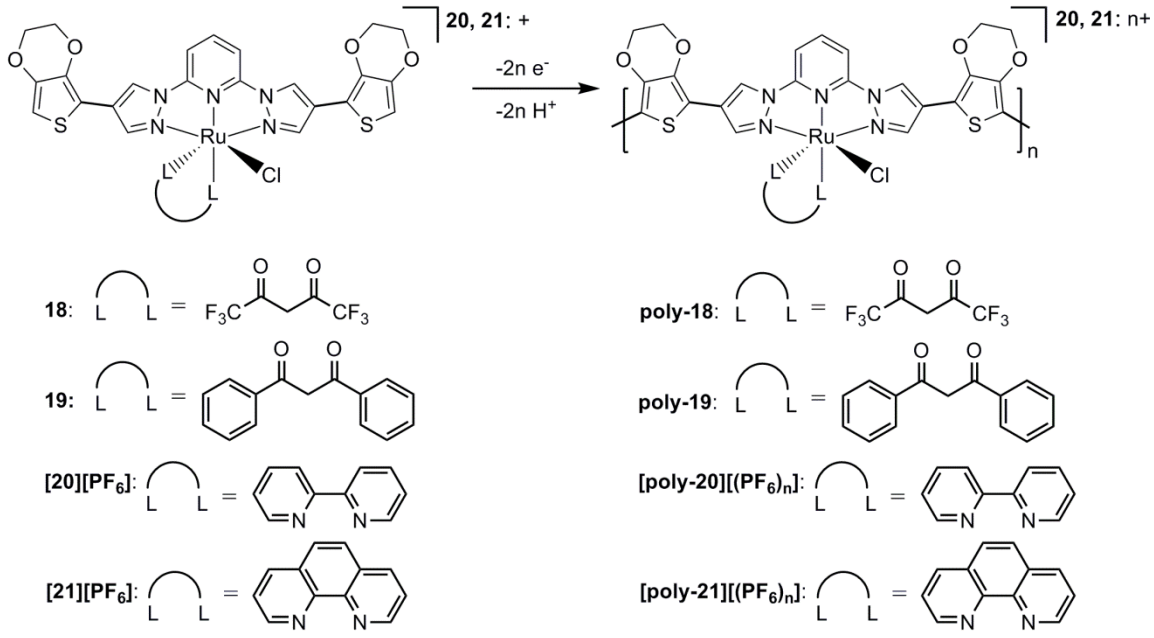

The polymerization scan of complex **18** (**Figure 35a**) has an oxidation at 0.31 V and reduction at 0.34 V (redox couple). An irreversible oxidation at 1.04V was observed. The peak at 0.31 V was assigned as the Ru(II)/Ru(III) oxidation, and the peak at 1.04 was assigned as oxidation of the monomer. New oxidation and reduction peaks grow at -0.04V and 0.71V respectively. Complex **19** has Ru (II)/Ru(III) redox couple at 0.04V and –0.40 V, and monomer oxidation is observed at 0.75 V. Complex **20** has Ru (II)/Ru(III) redox couple at 0.51 V and 0.41 V. Monomer oxidation was observed at 0.78 V, and new oxidation (1.04 V) and reduction (0.85 V) peaks were observed in subsequent scans. Complex **21** has Ru (II)/Ru(III) redox couple at 0.53 V and 0.46 V. Monomer oxidation

was observed at 0.8 V, and new oxidation (1.05 V) and reduction (0.96 V) peaks were observed in subsequent scans. The peak around –0.75 V which appears in the polymerization of all complexes, may belong to the reduction of short oligomers not incorporated in the polymer film.[119]

Polymerizations of complexes **18** and **19** have a linear increase of peak currents with number of scans up to sixteen and twenty scans, respectively (**Figure 35 a-d**, insets). Complexes **20** and **21** also have an increase in peak currents with number of scans; however the graphs start to level off at earlier scans. Accordingly, all polymers are redox-active.

The resulting polymer films of complexes were rinsed with fresh CH_2Cl_2 in the glove box to rinse any monomers and oligomers off of the polymers, and then the reddish brown film confined to the electrode was cycled in a monomer-free electrolyte solution of 0.1 M $TBAPF_6$ at scan rates varying 10–500 mV/s (**Figure 36**). **Poly-20** has reversible peaks at 0.53 V and 0.45 V; **poly-21** has reversible peaks at 0.60 V and 0.46V. Peak currents increase with increasing scan rate for both **poly-20** and **poly-21**. Scan rate dependence of the polymers was measured for characterization. It is quite linear up to 100 mV for both polymerization processes, indicating that the electroactive material is not limited by the ionic flux of counter ions. Because there is a decrease in charge mobility through the polymer backbone at higher scan rates, less facile ion transport and a deviation from the linear relationship occur. A very similar ruthenium-containing conducting polymer reported in the literature has results consistent with these.[119]

Complexes **18** - **21** have also been polymerized on a stainless steel surface as well as ITO on a glass substrate for XPS (X–ray photoelectron spectroscopy) measurement; however, the Ru peak coincides with the carbon peak in XPS, and the percentage for the Ru atoms in the analysis were exaggerated. The other problem is that our electrolyte was

0.1 M $TBAPF_6$ (tetrabutyl ammonium fluoride hexafluorophosphate) in CH_2Cl_2, although the polymers were rinsed with CH_2Cl_2; after the polymerization was finished, some of the $TBAPF_6$ remained in the polymer film, so the percentage of N, F, and P atoms were also hard to interpret.

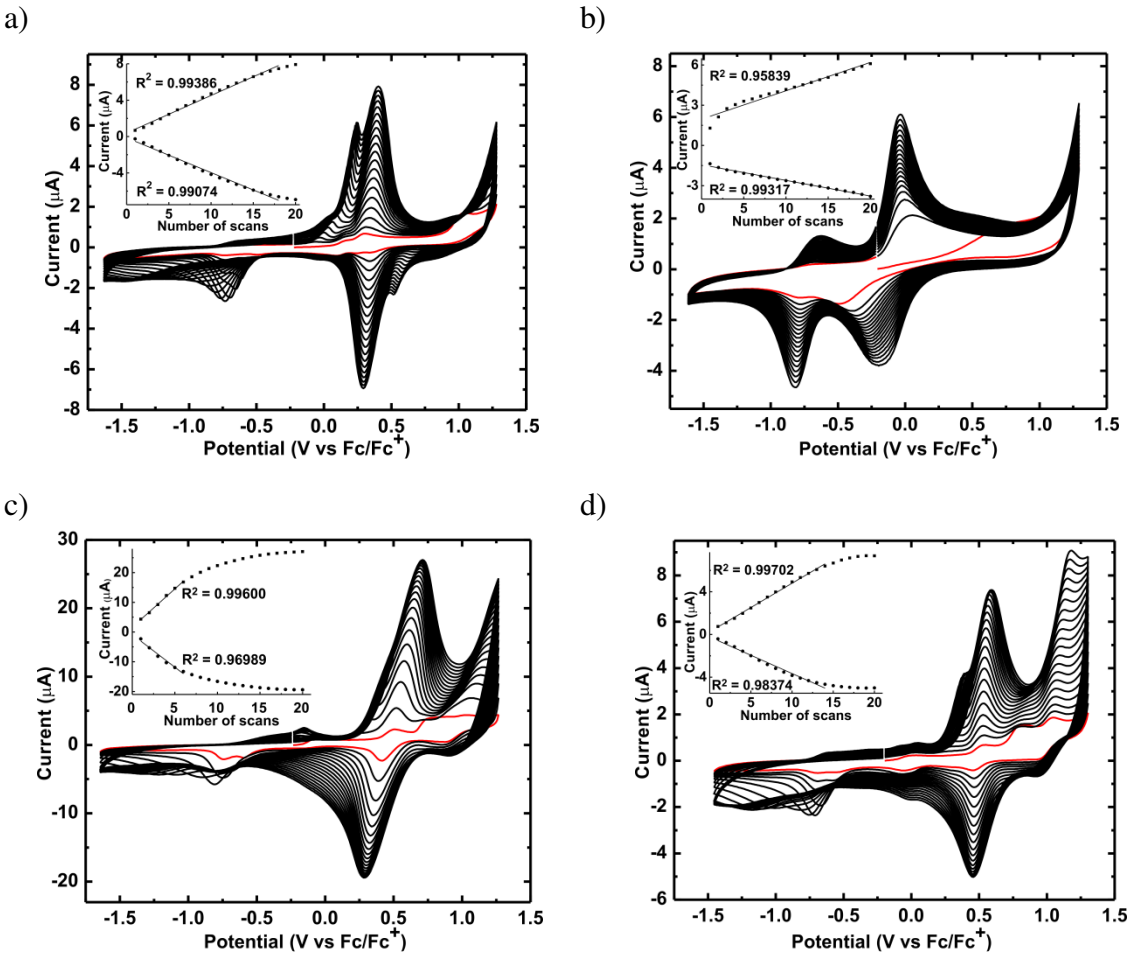

Figure 35. Electropolymerization of ruthenium complexes, initial scans shown in red. Insets: Current vs. number of scans. a) **18** b) **19** c) **20** d) **21**.

a) b)

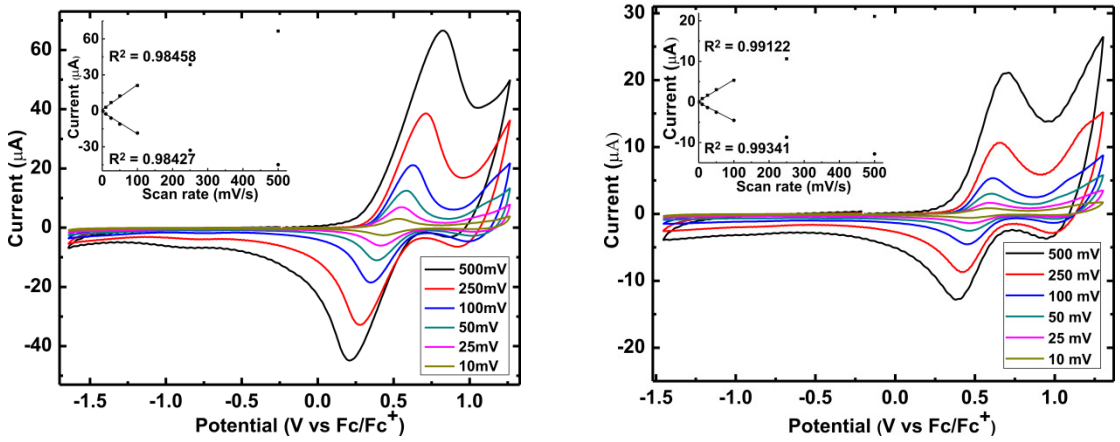

Figure 36. Electrochemical scan rate dependance of a) **poly-20** b) **poly-21**. Insets: Current vs scan rate.

UV-Visible Studies

All four complexes have Ru^{2+}, which is a d^6 system. For most Ru (II) complexes in the literature, the lowest excited state is a ^{3}MLCT, which undergoes slow radiationless transitions and therefore exhibits a long lifetime and intense luminescence emission.[53]

UV-visible spectroscopic characterization of complexes **18, 19, 20, 21** and ligand 2,6-Bis[4-[2-(3,4-diethylenedioxy)thiophene]pyrazol-1-yl]pyridine ($EDOT_2NNN$) were obtained. Complexes are maroon to reddish brown; the ligand is tan in color. Molar extinction coefficient values versus wavelength of the complexes were shown in **Figure 37**. Complexes **18**, **19**, **20** and ligand $EDOT_2NNN$ were dissolved in CH_2Cl_2; complex **21** was dissolved in CH_3CN (due to lower solubility in CH_2Cl_2) to prepare stock solutions for UV-Vis absorption spectra. The maximum absorptions are below 300 nm for complexes **18**, **20**, and **21**, and the maximum absorptions are above 300 nm for complex **19** and ligand $EDOT_2NNN$ due to LC (ligand centered) π to π^* transitions.[126, 53] Ligand

$EDOT_2NNN$ and complex **18** have relatively small molar-extinction coefficient values, i.e. 29034 and 29011, than complexes **19**, **20**, and **21**, which have molar-extinction coefficient values of 52803, 66486, and 66997 $M^{-1}cm^{-1}$, respectively. Intense visible absorption bands around 450-600 nm were assigned as ^{1}MLCT for the complexes,[126] and there clearly is no such a band in the UV-Vis spectrum of ligand $EDOT_2NNN$. No peak was observed for ^{3}MLCT absorption at RT. Results are consistent with the $Ru(bpy)_3^{2+}$ complex, which has reported values of LC transition at 285 nm, MLCT transitions at 240 and 450 nm, and MC transition at 344 nm (shoulder). ^{3}MLCT of the $Ru(bpy)_3^{2+}$ complex was observed at about 550 nm ($\varepsilon \sim 600$) when the measurement was done in ethanol–methanol glass at 77K.[53]

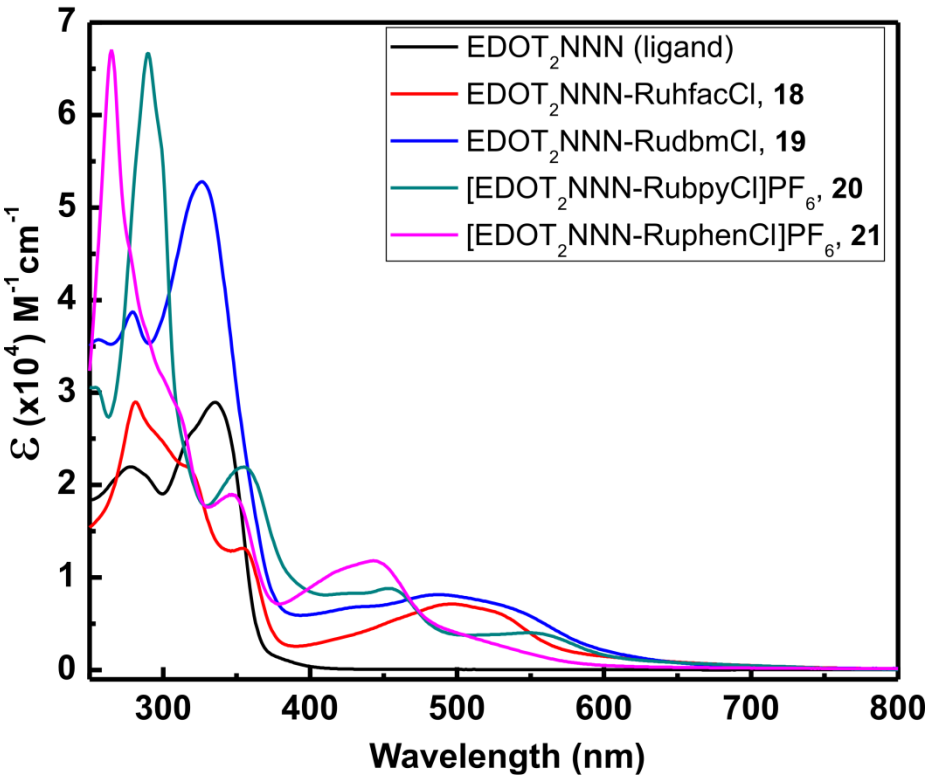

Figure 37. Molar extinction coefficient values vs wavelength for the complexes **18**, **19**, **20**, **21** and the ligand $EDOT_2NNN$.

Ligand $EDOT_2NNN$ has an absorption maximum at 335 nm. The hfac, dbm, bpy, and phen ligands have their absorption maxima and molar-extinction coefficients measured in CH_2Cl_2 as follows: for phen λ_{max} = 264 nm, ε = 31000[127]; bpy λmax = 302 nm, ε = 14125[128]; dbm λmax = 337 nm, ε = 26646[129]; hfac λmax = 275 nm[130]. For all complexes, absorption maxima are blue shifted upon Ru^{2+} coordination with respect to ligand $EDOT_2NNN$. Complex **19** has only 9 nm blue shift, other complexes have larger blue shifts; i.e. 54 nm for complex **18**, and 45 nm for complex **20**, and 70 nm for complex **21**. When the absorption maxima of each complex are compared with the absorption maxima of the corresponding bidentate ligand, shift in λmax upon coordination is relatively small, i.e. **18** is red shifted by 6 nm, **19** blue shifted by 17 nm, **20** is blue shifted by 12 nm, and **21** is unchanged.

Complex **21** was electropolymerized on ITO coated glass surface to obtain the solid state absorption spectrum of the corresponding polymer (**Figure 38**). An empty ITO coated glass was used as a blank in a double beam instrument. The solid state UV-Vis spectrum of **Poly-21** shows peaks at 289 and 355 nm and a shoulder at 441 nm. Absorbance measurement was done up to 285 nm as a cut-off wavelength, due to the absorption coming from the substrate. The monomer complex **21** has peaks at 223, 265, 349, and 443 nm. The peaks at 265 and 349 nm in the monomer **21** were slightly red shifted to 289 and 355 nm upon polymerization, due to the extended aromatic system formed between monomer units. The peak at 443 nm was shifted to 441 nm, however.

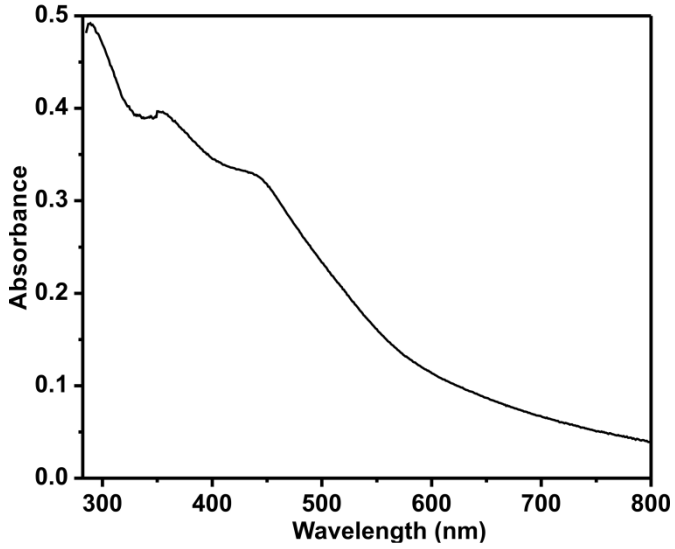

Figure 38. Absorption spectrum of **poly-21** electropolymerized on ITO coated glass surface.

Luminescence Studies

Photophysical data of each complex, i.e. excitation and emission spectra at 77K and RT, in EtOH/MeOH (4:1) and in 2-MeTHF (dry, air-free and aerated), in cuvette and in EPR tube, quantum yield, luminescence lifetime, and oxygen quenching, have been obtained and listed in **Table 13**. Optical density of all complexes was about 0.1 absorbance unit to exclude any excimer formation and concentration quenching effect. Quantum yield measurements by using an integrating sphere did not give any useful data; therefore, measurements were done by relative quantum yield technique in which previously reported values for a standard (or reference) are needed. $Ru(bpy)_3Cl_2$ was chosen as the reference. Although 2-MeTHF was used in the initial luminescence experiments, EtOH/MeOH (4:1) was used for the same measurements (to compare lifetimes) and for the further experiments because experimental conditions were required be the same as the reference. Relative quantum yield of each complex was calculated by using the following formula,[131] where integration is the area under emission peak.

$\Phi_{reference}$ was reported as 0.35 and 0.328 in the literature, and the latter was used in our calculations.[126, 132]

$$\Phi_{sample} = \Phi_{ref} \times \frac{\text{Integration sample}}{\text{Integration ref}} \times \frac{\text{Absorbance reference}}{\text{Absorbance sample}} \quad (2)$$

Radiative (k_r) and nonradiative (k_{nr}) decay constants as well as oxygen quenching rate coefficient (k_q) of each complex were calculated by using the following formulas,[133, 134] in which relative quantum yields of emission (Φ_{Em}), measured phosphorescence lifetimes (τ_0), and measured intensity of emissions (I) were used. Oxygen concentration in the alcohol mixture was taken from the literature.[135]

$$k_r = \Phi_{Em}/\tau_0 \quad (3)$$

$$k_{nr} = (1- \Phi_{Em})/\tau_0 \quad (4)$$

$$I/I` = 1+ (k_q. \tau_0.[O_2]) \quad (5)$$

Dry solvents of 2- MeTHF, EtOH and MeOH were degassed by freeze-pump-thaw technique for 4-5 cycles and then transferred into the glove box which was filled with a N_2 atmosphere. EtOH/MeOH (4:1) solution was prepared for stock solutions of each complex, and a sample of each complex solution was then taken to measure its optical density (~ 0.1 A). After reaching a proper range of optical density (0.05–0.1 A), fresh stock solutions were transferred into capped and parafilmed quartz EPR tubes as well as airtight quartz cuvettes in the glove box. Measurements with airtight cuvettes could only be done at RT, but samples in EPR tubes were suitable for both RT and 77 K measurements. A second set of measurements of each complex and the standard were

done in an EPR tube in four different conditions, under the following order: air-free–RT, air-free–77 K, aerated–RT, aerated–77K. Resulting luminescence spectra are shown in **Figure 39-42**. First, luminescence spectra of samples and the standard in airtight cuvettes were obtained, and then airtight cuvettes were aerated via bubbling air from a Pasteur pipette for the corresponding measurements (**Figure 43, 44**).

Table 13. Photophysical data for the ruthenium complexes.

Complex	**18**	**19**	**20**	**21**
λ_{Abs}/nm, (ε, $M^{-1}cm^{-1}$)	281 (29011), 316 (21986)sh, 354 (12247), 497 (6896)	256 (35714), 279 (3873), 326 (52803), 489 (8151)	254 (30553), 290 (66486), 355 (21887), 455 (8894), 550 (4119)	223 (53267), 265 (66997), 349 (18970), 443 (11820) 549 (4033)
$\lambda_{Em\ (Ex)}$/nm at 77K	310, 400, 630, 750 (276); 450 (400)	306, 400, 635, 760 (278); 485 (450)	315, 400, 620, 750 (277); 581 (456)	312, 400, 618, 750 (278); 566 (453)
$\lambda_{Em\ (Ex)}$/nm at RT	318, 640 (276)	316, 650 (276)	327, 650 (277); 610 (450)	316, 618 (275); 580 (445)
τ_0/µsec (^{3}MLCT) in 2-MeTHF (air-free, dry)	6 +/- 3	7.2 +/- 0.4	11 +/- 1	14 +/- 1
τ_0/µsec (^{3}MLCT) in EtOH/MeOH (4:1) (air-free, dry)	6 +/- 2	8 +/- 3	10 +/- 3	14 +/- 1
τ_0/µsec (^{3}MLCT) in EtOH/MeOH (4:1) (aerated)	6 +/- 2	7 +/- 2	10 +/- 4	14 +/- 3
τ_0/µsec (^{3}MC) in EtOH/MeOH (4:1) (aerated)	5 +/- 1	4 +/- 2	9 +/- 6	7 +/- 3
Φ_{Em} (%) of phos. (^{3}MLCT) (air-free, dry)	1.07	1.4	7.94	10.6
Φ_{Em}(%) of phos. (^{3}MLCT) (aerated)	1.13	1.3	6.98	7.99
Φ_{Em} (%) of flurores. (air-free, dry)	35.8	14.4	19.3	22.5
Φ_{Em} (%) of flurorescence (aerated)	34.4	14.2	19.2	13.7
k_r (s^{-1}), air-free (aerated)	1783.33 (1883.33)	1750 (1857.14)	7940 (6980)	7571.43 (5707.1)
k_{nr} (s^{-1}), air-free (aerated)	164883.33 (164783.33)	123250 (141000)	92060 (93020)	63857.14 (65721.43)
k_q (M^{-1} s^{-1}) (O_2 quenching)	4.68×10^6	1.287×10^7	8.49×10^6	1.353×10^7

In order to find the excitation and emission spectra of complexes, solutions of each complex were excited at their UV–Vis absorption maxima. Resulting emission maxima were used to obtain excitation maxima, and finally, samples were excited at the excitation maxima found to obtain the maximized emission spectra. All complexes have excitation maxima at 276-278 nm both at RT and at 77 K, although all have different absorption maxima in UV-Vis spectra (**Figure 37** and **39**). Corresponding emission maxima are also more or less the same, i.e. 310-320 nm and a broad peak ~550-750 nm (**Figure 39**). Emissions around 310-320 nm correspond to ligand fluorescence, because of both small Stokes shift and short excited-state lifetime. Emission around ~550-750 nm should come from ligand phosphorescence due to intersystem crossing after having a singlet excited state. When cooled to 77 K in EtOH/MeOH (4:1) glass, emission intensity was increased for all complexes and for the $Ru(bpy)_3^{2+}$ standard; the broad peak ~550-750 nm became slightly structured and blue shifted; furthermore, a new structured peak appeared around ~350-550 nm. These observations are due to the reduction of thermal nonradiative pathways available for energy loss.

Luminescent properties of a complex depend on the ordering of its low energy excited states and the orbital nature of its lowest excited state. Therefore, the energy positions of MC, MLCT, and LC are important. The energy of the MC excited states depends on the ligand field strength, which is related to σ–donor and π–acceptor properties of the ligands, steric crowding around the metal, and the bite angle of the polydentate ligands. The energy of the MLCT excited states depends on the reduction potential of the ligand involved in the MLCT, the oxidation potential of the metal in the complex, and the charge separation caused by the transition. The energy of the LC excited states depends on the intrinsic properties of the ligands, such as the energy gap between HOMO–LUMO levels and singlet–triplet splitting. Ru(II) polypyridine

complexes generally have ^{3}MLCT as their lowest excited state and show long lifetimes and intense luminescence properties.[53]

In order to find the orbital nature of the emission that occurred from ~350 to 550 nm upon cooling to 77 K, emission spectra of all complexes and the standard were compared to the emission spectrum of the free ligand $EDOT_2NNN$, which was previously reported.[122] The RT absorption and the emission of $EDOT_2NNN$ were reported as 339 nm and 378 nm respectively. These values are higher than the absorption and emission of the complexes. Ligand phosphorescence of $EDOT_2NNN$ was observed between 484 and 650 nm. There is no peak in that region in the emission spectra of the complexes. All of the complexes and the standard have the same structured emission from ~375 to 550 nm upon cooling. The only common component among complexes **18** and **19** and the standard is the Ru^{2+}ion, yet the emissions from ~350 to 550 nm overlap; the common components among complexes **20** and **21** and the standard are Ru^{2+} and the bpy ligand (phen is similar to bpy in complex **21**); furthermore, the lifetime of the emissions are in the same range, i.e. a few microseconds (**Table 13**). Assignment of the peak is made as ^{3}MC emission. Literature supports the idea as follows: in d^6 octahedral complexes, MC excited states are strongly displaced with respect to the ground state geometry along metal–ligand vibration coordinates. As the lowest excited state is MC, it undergoes a fast nonradiative pathway to the ground state or ligand dissociation reactions. As a result, no luminescence can be observed at RT. Because LC and MLCT excited states are not strongly displaced compared to the ground state, fast nonradiative pathways do not occur, and luminescence can be observed. Luminescence coming from ^{3}LC and ^{3}MLCT states is usually structured. ^{3}LC emission generally occurs close to the free ligand emission; on the other hand, ^{3}MLCT emission occurs at lower energies. Moreover, ^{3}LC emission is less influenced by the heavy metal ion, thus emission lifetime is longer than ^{3}MLCT.

Luminescence arising from a ^{3}MC excited state appears as a Gaussian shaped emission band, red shifted compared to the lowest energy absorption bands. Excited state lifetime and intensity both decrease with increasing temperature. ^{3}MC emissions cannot be observed in fluid solutions at RT.[53]

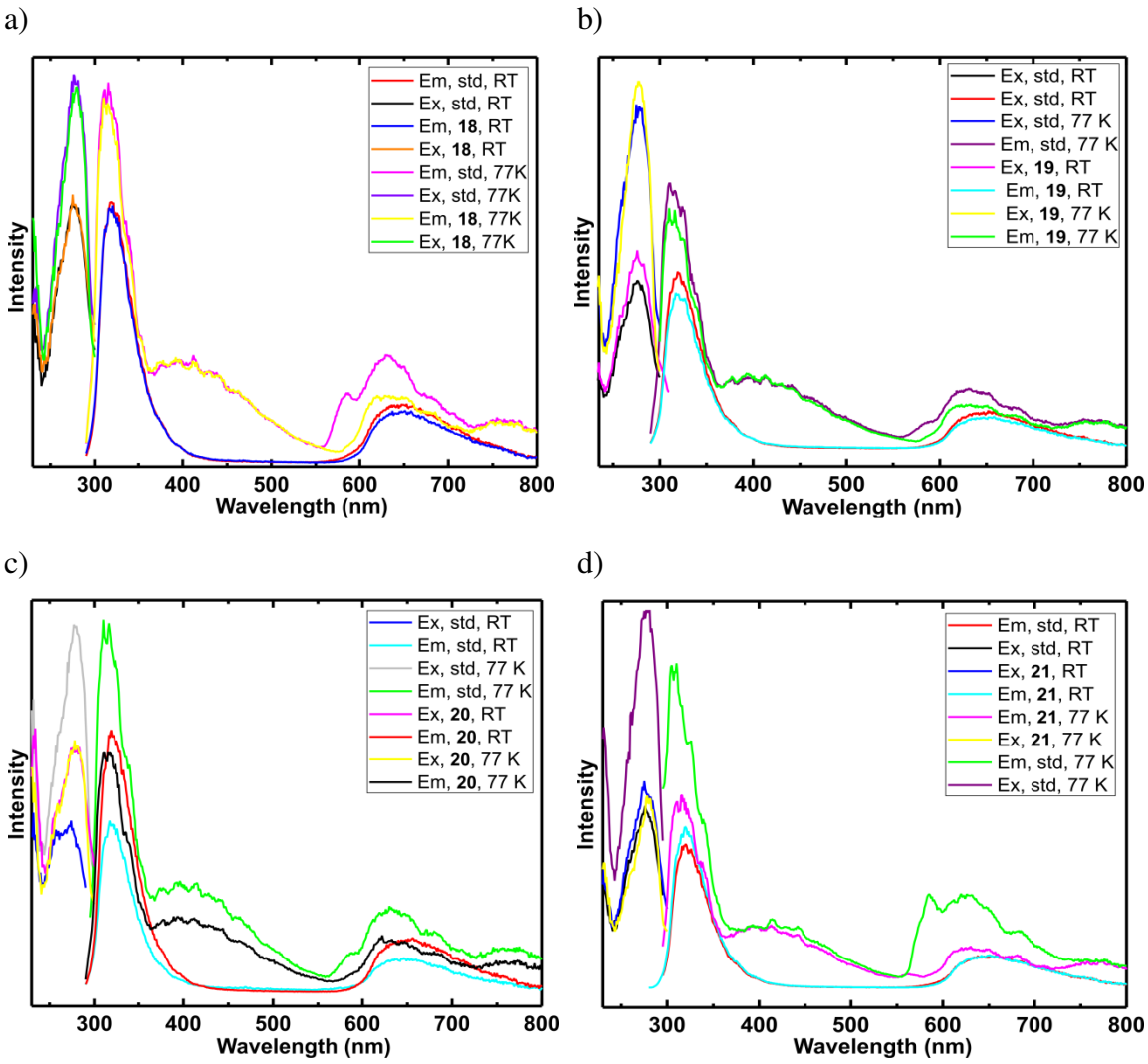

Figure 39. Excitation and emission spectra of the complexes a) **18**, b) **19**, c) **20**, d) **21** and $Ru(bpy)_3^{2+}$ as the standard in dry, air-free EtOH/MeOH (4:1) solution at RT and at 77 K in a quartz EPR tube.

In order to find luminescence originating from the MLCT transition, excitation spectra of complexes were obtained by having the emission maxima around 630 nm, and then the complexes were excited at the excitation maxima found (~ 450 nm). Corresponding maximized emission spectra are assigned as the ^{3}MLCT emissions.[53, 126]

Luminescence measurements were done first at RT, then at 77 K in a quartz EPR tube (**Figure 40–42**). For complexes **18** and **19**, both excitation and emission peaks were weak. In **Figure 40**, complex **18** did not even show an emission peak at RT in an EPR tube (blue graph). Upon cooling to 77 K, a shoulder appeared (green graph). Complex **19** yielded better results at both temperatures; however, the peaks appeared still weak and noisy (black and red graphs). Emission of **19** is enhanced upon cooling and blue shifted. Neither complexes showed good emission peaks in the measurements done at RT in a cuvette.

^{3}MLCT emissions of complexes **20** and **21** in an EPR tube at RT show small blips (**Figure 41, 42**). Upon cooling to 77 K, both complexes show highly structured excitation and emission bands as expected for MLCT transition. In addition, emission maxima of **20** and **21** were blue shifted when cooled to 77 K. Again, having a broad, structureless spectra at RT and structured spectra upon cooling show that thermal nonradiative pathways are reduced due to the energy loss. Excitation and emission spectra of complex **20** for the MLCT transition overlap with excitation and emission spectra of the standard. On the other hand, emission spectrum for the MLCT transition of complex **21** is 15 nm blue shifted with respect to the standard.

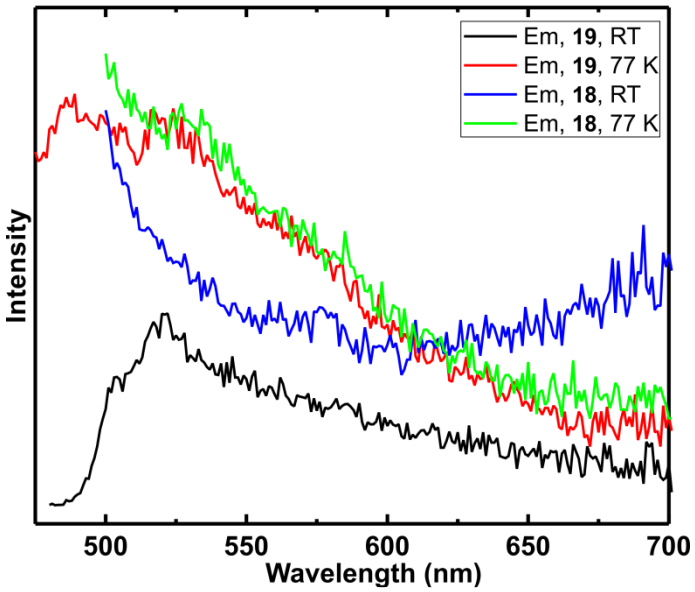

Figure 40. Emission spectra of ^{3}MLCT phosphorescence of complexes **18** and **19** at RT and at 77 K in a dry, air-free EtOH/MeOH (4:1) solution in a quartz EPR tube.

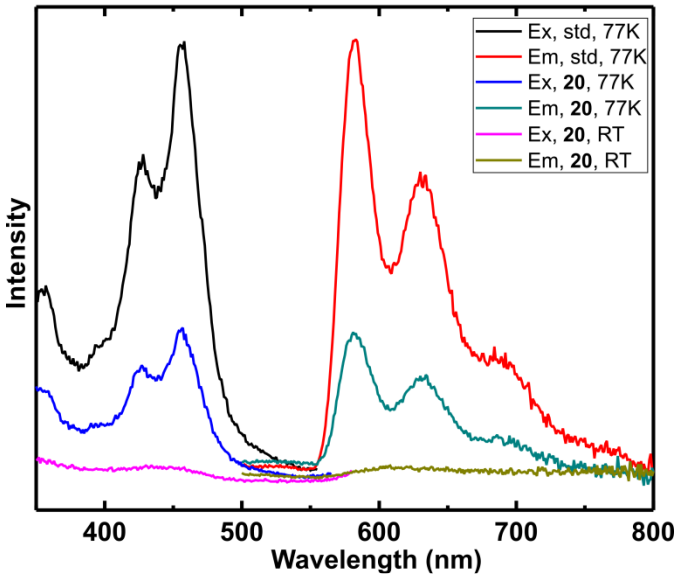

Figure 41. Excitation and emission spectra of ^{3}MLCT phosphorescence of complex **20** and $Ru(bpy)_3^{2+}$ as the standard at RT and at 77 K in a dry, air-free EtOH/MeOH (4:1) solution in a quartz EPR tube.

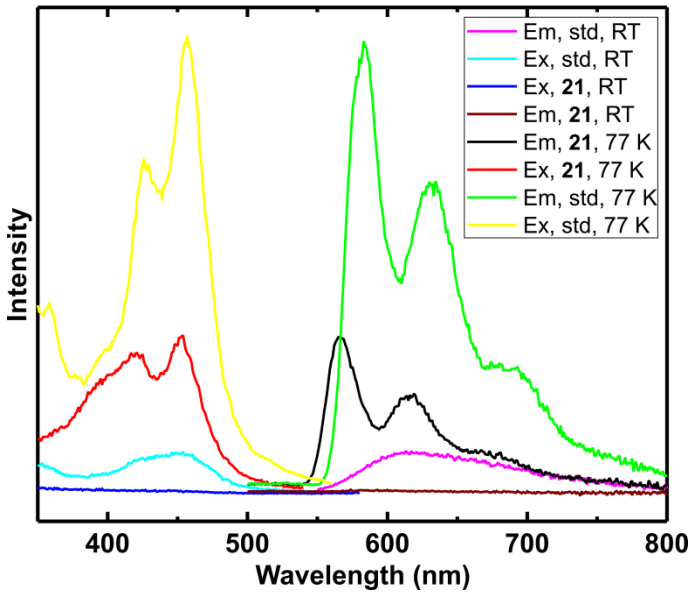

Figure 42. Excitation and emission spectra of ^{3}MLCT phosphorescence of complex **21** and $Ru(bpy)_3^{2+}$ as the standard at RT and at 77 K in a dry, air-free EtOH/MeOH (4:1) solution in a quartz EPR tube.

Excitation and emission spectra of **20** and **21** in a quartz cuvette at RT showed broad, unstructured bands, as was true for the measurements done in EPR tube at RT. Peak maxima of complex **21** are again blue shifted by 10–15 nm with respect to **20** and the standard (**Figure 43, 44**).

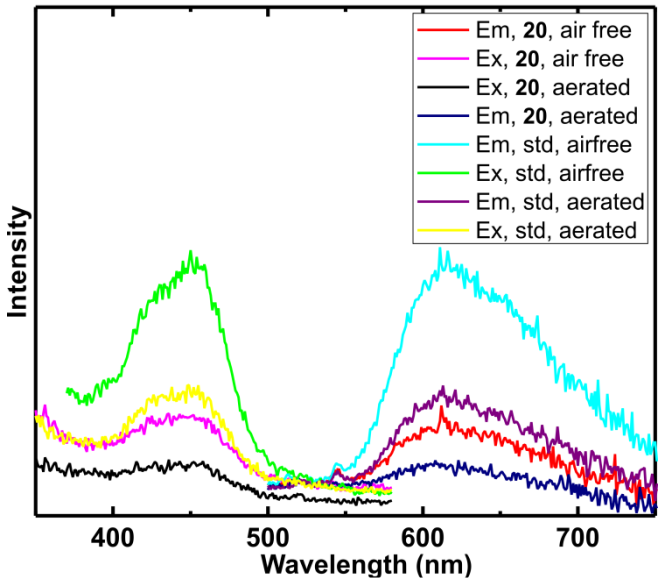

Figure 43. Excitation and emission spectra of ^{3}MLCT phosphorescence of complex **20** and $Ru(bpy)_3^{2+}$ as the standard at RT in air-free and aerated EtOH/MeOH (4:1) solution in an airtight quartz cuvette.

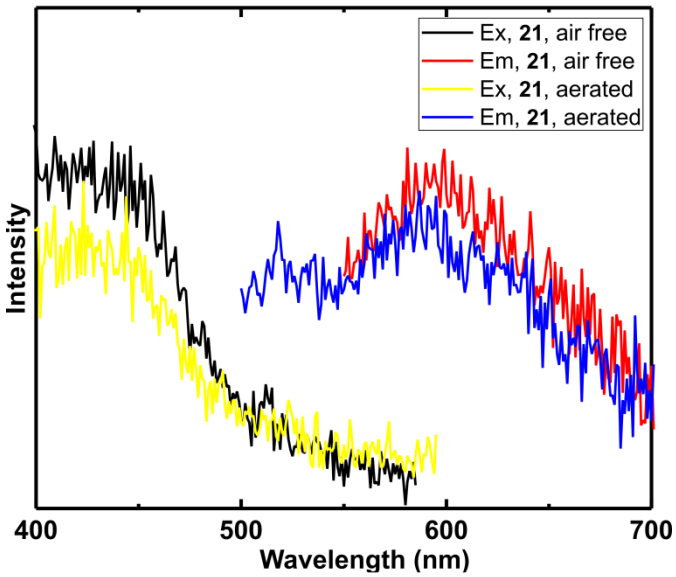

Figure 44. Excitation and emission spectra of ^{3}MLCT phosphorescence of complex **21** at RT in air-free and aerated EtOH/MeOH (4:1) solution in an airtight quartz cuvette.

Emission lifetimes of all complexes in both air-free and aerated solutions were measured at 77 K and given in **Table 13**. The lifetime of the standard was also measured and found to be consistent with the literature value of 5 μs.[53] The complexes have mean lifetime values from 6 to 14 μs. Complex **18** has the shortest lifetime, and complex **21** has the longest. The lifetime values of complexes changed neither by changing the solvent from 2-MeTHF to EtOH/MeOH (4:1) nor by introducing air into the solutions. Lifetimes of phosphorescence due to ^{3}MC transition of complexes were also measured. Corresponding values were almost the same as, but slightly lower than ^{3}MLCT phosphorescence for all complexes.

Fluorescence and phosphorescence quantum yields of complexes were calculated by formula (2) both in dry, air-free and aerated solutions of complexes. Quantum yield of ligand fluorescence was the highest in **18**; however, quantum yield of phosphorescence due to ^{3}MLCT was the highest in **21**. Emission intensities of both fluorescence and phosphorescence values of all complexes decreased upon exposure to air. Corresponding quantum yield calculations were also decreased up to 2.61% for the phosphorescence and 8.8% for the fluorescence of **21**.

Quenching of the emission by dissolved molecular oxygen was investigated. Preparation of degassed solution of complexes and introduction of air into samples was described previously. Farley *et al.* reported a very efficient quenching of dissolved oxygen on their series of platinum complexes by the same technique we used, except [O_2] was taken as 0.0022 M in their calculations, rather than the value of 0.0019099 M that we used.[135, 136] In this study, oxygen quenching resulted in a slight decrease in the emission intensities and a k_q value on the order of 10^6–10^7 M^{-1} s^{-1}, in contrast to the values reported by Farley *et al.* as in the order of 10^9 M^{-1} s^{-1}. Calculated values of quantum yield also show that oxygen quenching is minimal (**Table 13**). The reason for having this much

difference in quenching might be the empty axial position of the metal in square planar platinum(II) complexes that Farley *et al.* made, which are relatively accessible for interaction with a quencher; on the other hand, it is hard to reach to metal center of an octahedral ruthenium complex, which is coordinatively saturated. Another technique for oxygen quenching was reported by Rusak *et al.* In this technique, oxygen quenching of $Ru(bpy)_3^{2+}$ was studied by introducing SO_3^{2-} anions into the $Ru(bpy)_3^{2+}$ solution to adjust O_2 concentration by the reaction $2SO_3^{2-} + O_2 \rightarrow 2SO_4^{2-}$, and measurements were carried out at RT, in which the lifetimes were shorter than the value at 77 K.[134] Measurements were done in aqueous solution of $Ru(bpy)_3^{2+}$ without any degassing procedure, because the luminescence without SO_3^{2-} anions is measured first, and SO_3^{2-} is then added to decrease the O_2 concentration to obtain enhanced luminescence.

Complex **21** was chosen to be electropolymerized on ITO coated glass surface to obtain the solid state excitation and emission spectra of the corresponding polymer because **21** has the highest quantum yield of phosphorescence and the longest lifetime. First, **poly-21** was excited at 276 nm, which is the excitation wavelength of monomer complexes mainly for fluorescence emission; corresponding emission spectra were recorded at 77 K (**Figure 45 a**). Emission peaks were found at around 312 nm and 728 nm. A peak at 312 nm appeared in the same region as in the monomer; however, the broad peak at ~728 nm had a considerable red shift compared to the monomer emission, which was around 630 nm. The reason for this shift may be the extended π conjugation upon polymerization. The peak at 312 nm had a lower intensity than the broad peak at 747 nm. Emission spectrum of the monomer was the opposite in terms of the intensity, i.e. the peak around 310 nm was much more intense than the MLCT emission peak at ~630 nm. The reason may be that the singlet excited state of the polymer encounters efficient intersystem crossing, so that the triplet emission is enhanced. **Poly-21** was

excited also to obtain MLCT emission, first at 453 nm, the monomer excitation wavelength, which did not result in any emission. Two excitation maxima were found to obtain emission at 747 nm (531 and 639 nm, **Figure 45** in black). Then, **poly-21** was excited at these two wavelengths to obtain emission spectra (**Figure 45 b** red and blue). The lifetime of 747 nm emission was measured as 13 +/- 8 μs. This value is very close to the monomer lifetime (14 +/- 1 μs) for an emission at 566 nm at 77 K, however, the standard deviation is much higher than the corresponding value for the monomer. The ITO coated glass substrate was also excited at 456 nm to see if the emission originated from the ITO itself. Emission maximum of the ITO surface was found as 730 nm which is a value fairly near, but different from the **poly-21** emission at 747 nm.

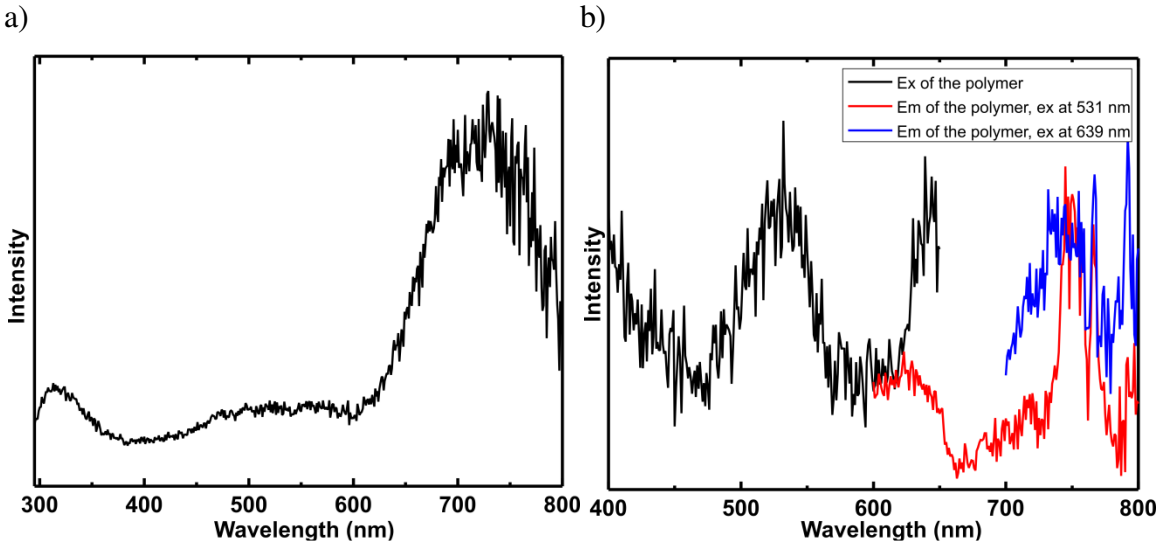

Figure 45. a) Emission spectrum of **poly-21** excited at 276 nm. b) Excitation (black) and emission spectra (red and blue) of **poly-21** in the visible region of the spectrum.

CONCLUSIONS

In summary, we report the electropolymerization/electrochemistry, UV-Vis absorption and luminescence properties of EDOT-functionalized (2,6-bis(pyrazol-1-yl)pyridine) Ru(II) (L′)Cl complexes in which two of the L′ ligands are anionic (hfac and dbm), and the other two are neutral (bpy and phen) bidentate ligands for potential OLED applications. All complexes are electropolymerizable and polymers are electroactive. The complexes are emissive with relatively long lifetimes and oxygen quenching of the emission is minimal. Complex **21** was polymerized on an ITO-coated glass substrate for the luminescence studies of the resulting polymer which has promising results for photoluminescence. Future studies will focus on preparing derivatives of the bidentate ligands to optimize and tune the emission of the complexes of the corresponding polymers.

Chapter 5: Synthesis, Characterization, Coordination Chemistry, and Luminescence Studies of Copper, Silver, Palladium, and Platinum Complexes with a Phosphorus/Nitrogen/Phosphorus Ligand

INTRODUCTION

PNP ligands have been used widely in coordination chemistry since the 1960s.[137] Complexes of these ligands to transition metals have been extensively reported since this type of ligands combines hard and soft donor atoms to give flexible coordination modes.[62] The N-donor group in ligands of the type $RN(CH_2CH_2PR'_2)_2$ is hemilabile. When the R group is aromatic, for example, a phenyl group, the lone pair of electrons on the nitrogen is conjugated to the phenyl group. Consequently, the ligand is more hemilabile than similar ligands containing hydrogen or alkyl groups bound to the nitrogen. The preference for forming complexes as the monomeric tridentate ligands or the as monomeric and dimeric bidentate ligands can be controlled by modifying the relative donor strength of the nitrogen donor via adjusting the electron donating or withdrawing ability of the substituent R and the anion X^{-}[40, 138] (**Figure 46**).

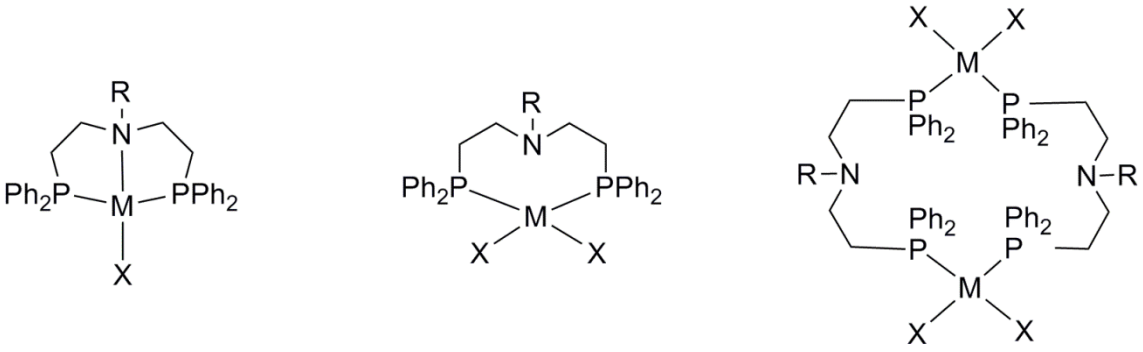

Figure 46. Binding modes of PNP ligand of the type $RN(CH_2CH_2PPh_2)_2$.

In addition to having different binding modes, a PNP ligand of the type $RN(CH_2CH_2PPh_2)_2$ can also be used to synthesize oligomeric and polymeric coordination

compounds.[40] Complexes of this type of PNP ligand are suitable for many applications, such as molecular materials and catalysis.[139, 140]

Various complexes of copper, silver, gold, platinum, and palladium with nitrogen and phosphorus donors have been reported for their luminescence behavior as well as their interesting structures (**Figure 47**).[141-145] Jun-Feng Zhang *et al.* have reported copper and platinum complexes of the naphthyridine-phosphine ligand with their photophysical properties and different coordination modes. They reported both mononuclear and binuclear copper complexes with distorted tetrahedral geometry, as well as a binuclear copper complex with distorted trigonal planar geometry, which has a Cu–Cu bond. Their platinum complexes, however, are mononuclear with square planar geometry. Spectroscopic investigations showed that solution emissions of their compounds at room temperature resulted in ligand fluorescence, whereas solid state phosphorescence was obtained from a copper and a platinum complex.[141] Vivian Wing-Wah Yam *et al.* also reported luminescent trinuclear copper(I) acetylides with PNP [bis(diphenylphosphino)-alkyl/-aryl amine] as bridging ligands. They changed the substituents on the diphenylphosphinoamine for the design and study of donor-acceptor properties and substituent effects on the spectroscopic and electrochemical properties of the trinuclear copper complexes.[142] Seth B. Harkins and Jonas C. Peters reported an exceptional luminophore based on an amido-bridged bimetallic copper system, $[(PNP)CuI]_2$, derived from a chelating bis(phosphine)amide ligand ($[PNP]^-$ = bis(2-(diisobutylphosphino)phenyl)amide). Its combined quantum yield is $\Phi > 0.65$, and its lifetime is $\tau > 10$ μs.[143] Vincent J. Catalano *et al.* reported luminescent gold(I) and silver(I) metallocryptates using a hybrid phosphine-phenanthroline ligand, 2,9-bis(diphenylphosphino)-1,10-phenanthroline (P_2phen).[144] Recently, Qiong-Hua Jin *et al.* reported palladium(II)–PPh_3 complexes with different heterocyclic-N/NS co-ligands, and

found that the coexistence of PPh_3 and heterocyclic-N/NS ligands remarkably change the luminescence property of d^8 palladium(II) complexes, although d^8 palladium(II) complexes are well known quenchers like platinum analogues.[145]

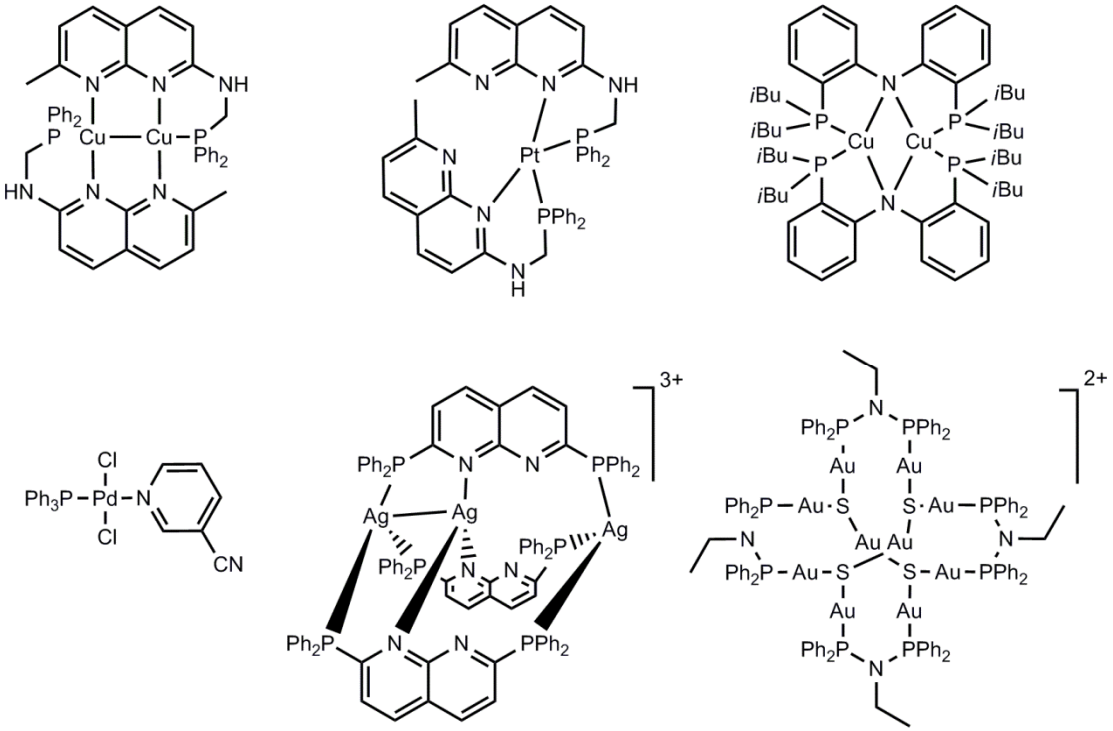

Figure 47. Examples of luminescent complexes of copper, silver, gold, platinum and palladium with phosphorus and nitrogen donating ligands.

Luminescent platinum (II) complexes can be divided into three groups: 1) mononuclear complexes, 2) dinuclear complexes with bridging ligands, and 3) linear chains comprising stacked complex units. Platinum (II) complexes with a d^8 electronic structure are often stacked in the solid state, which results in luminescence coming from metal–metal electronic interactions. The majority of the mononuclear platinum (II) complexes were non-luminescent in solution at room temperature, although they emitted at low temperatures. The reasons could be that the *d-d* transition states may induce fast

non-radiative deactivation, and solvent molecules can cause facile quenching of the excited state, because the square-planar structures have open coordination sites, lastly, they can be quenched by triplet oxygen.[146] The metal-metal bond establishment resulted in the investigation of similar d^{10}-d^{10} complexes. Luminescence properties of phosphine complexes of d^{10} metals such as Cu(I), Ag(I), Au(I), Ni(0), Pd(0), and Pt(0) have been reported.[147] Interestingly, in polynuclear d^{10} metal complexes, short metal–metal distances were observed. In theory, in the absence of metal *(n+1)s* and *(n+1)p* electrons, the interaction between the closed shell d^{10} metal centers would be expected to be repulsive. However, configuration mixing of the filled *nd* orbitals with the empty *(n+1)s* and *(n+1)p* orbitals turns this repulsion into a slight attraction between the metal centers, resulting in a weak metal-metal bonding interaction.[148]

In addition to their luminescence properties, some of the PNP complexes show catalytic activities that were first reported with iridium, rhodium, and palladium. Some of the complexes are chiral or have hydrophilic groups; in some cases, the nitrogen atom is tethered to solid supports.[149] Hii *et al.* reported PNP-Pd complexes with both 0 and +2 oxidation states and studied the rate of oxidative addition of Pd(0) to aryl iodides.[62] They showed for the first time that the coordination behavior of PNP ligands with respect to palladium is dependent on the nature of the nitrogen donor. They also found that nature of the nitrogen donor dramatically altered the reactivity of their palladium(0) complexes in oxidative addition reactions toward aryl halides which is an important first step in many palladium catalyzed reactions.

In this study, we sought to prepare complexes of copper, silver, platinum, and palladium with N,N-bis[2 -(diphenylphosphino)ethyl]benzenamine (PNP) ligand and investigate the luminescence of the resulting complexes. Different coordination modes and different numbers of metal centers are possible with the title ligand. Consequently,

the luminescence properties of the resulting complexes may be affected. Moreover, fluorescence spectra of the title ligand are not previously reported nor is the crystal structure of a platinum complex with the ligands of the type $RN(CH_2CH_2PR'_2)_2$. It is possible to make an electropolymerizable version of the monomeric complexes, which have tridentate binding mode. These monomer complexes can be used for applications, such as luminescent polymers for PLED or heterogeneous catalysis.

EXPERIMENTAL

Instrumentation

NMR spectra were recorded with a Varian Unity + 300 or Varian 500 spectrometer using a 5 mm Auto-switchable probe ($^{1}H/^{19}F/^{13}C/^{31}P$). ^{1}H NMR signals were referenced to residual proton resonances in deuterated solvents. $^{13}C\{^{1}H\}$ NMR spectra were referenced relative to solvent peaks. $^{31}P\{^{1}H\}$ NMR spectra were referenced to a H_3PO_4 external standard. All peak positions are listed in ppm, and all coupling constants are listed in Hertz (Hz). Mass spectrometry was carried out using a Thermo Finnegan TSQ 700 spectrometer. Melting points were recorded on a Mel-Temp II melting temperature apparatus made by Laboratory Devices of Holliston, MA. Elemental analysis was performed by Quantitative Technologies Inc. (Whitehouse, NJ). Luminescence measurements were performed by a Photon Technology International QM 4 spectrophotometer. Samples were freshly prepared prior to analyses.

X-ray Crystal Structure Analysis

The single–crystal diffraction data of **22** were collected on a Nonius Kappa CCD diffractometer using a graphite monochromator with MoKα radiation (λ = 0.71073Å) and an Oxford Cryostream low temperature device. The single–crystal diffraction data of **23**, **24**, and **27** were collected on a Rigaku SCX-Mini diffractometer with a Mercury CCD using a graphite monochromator with MoKα radiation (λ = 0.71073Å). The single–crystal diffraction data of **25** and **26** were collected on a Rigaku AFC12 diffractometer with a Saturn 724+ CCD using a graphite monochromator with MoKα radiation (λ = 0.71073Å). Absorption corrections were applied using Multi-scan. Data reductions were performed using Rigaku Americas Corporation Crystal Clear version 1.40.[97] The

structures were solved by direct methods and refined anisotropically using full-matrix least-square methods with the SHELX 97 program package.[71] The coordinates of the non-hydrogen atoms were refined anisotropically, while hydrogen atoms were included in the calculation isotropically but not refined. Neutral atom scattering factors and values used to calculate the linear absorption coefficient are from the International Tables for X-ray Crystallography (1992).[72] Crystal data collection and refinement details are given in **Tables 14** and **15**. Selected bond lengths are given in **Tables 16–21**.

Synthesis

General Methods

All chemicals were purchased from commercial suppliers and were used as received. Air- and moisture-sensitive reactions were carried out in oven-dried glassware using standard Schlenk techniques under an inert nitrogen atmosphere or in a glove box with an argon atmosphere. Dry solvents were obtained from an Innovative Technologies Pure-Solv 400 solvent purification system. The target ligand, N,N-bis[2-(diphenylphosphino)ethyl] benzenamine **3**, was prepared according to Kostas' method[38] and synthesis scheme was shown in chapter 2 (**Scheme 1**). Bisbenzonitriledichloroplatinum (II) and bisbenzonitriledichloropalladium (II) were prepared according to literature methods.[150]

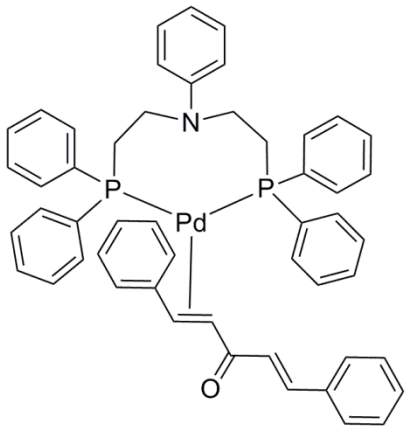

PNP-Pd-dba [22]. 3 (0.202 g, 0.39 mmol) was dissolved in 5 ml of THF in the glove box. Pd_2dba_3 (0.179 g, 0.205 mmol) was added to the ligand solution. The mixture was stirred overnight, then filtered through a piece of cotton and celite placed in a Pasteur pipette. The filtrate was dried under a Schlenk line. The residue was redissolved in DCM, on which hexanes were layered to afford orange crystals, which were then placed in the freezer. Crystals were isolated (57.4%, 0.192 g, 0.22 mmol) and characterized by X-ray diffraction analysis for the first time.[151] $^{31}P\{^{1}H\}$ NMR and MS are matching with the reported values.[62]

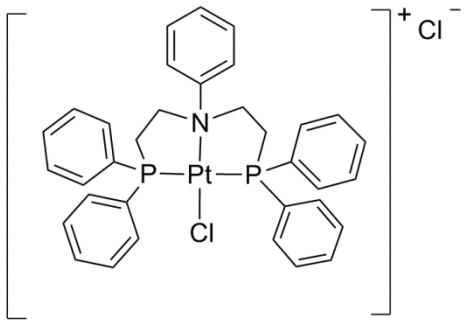

[PNP-PtCl]Cl [23]. Ligand **3** (0.145 g, 0.28 mmol) and bis-benzonitriledichloroplatinum (II) (0.128 g, 0.28 mmol) were weighed into separate Schlenk flasks in the glove box, then connected to a Schlenk line. Dry benzene was cannula-transferred into both flasks, which were then stirred. The mixture containing

platinum did not dissolve, so it was refluxed to produce a light yellow solution. The ligand solution was cannula-transferred into the refluxing metal solution. The reaction mixture was refluxed for 1.5 hours to obtain a white precipitate and a colorless solution. The mixture was cooled to room temperature under N_2. The precipitate was cannula-filtered and then dried under vacuum to afford a white solid **23** (94.2%, 0.2067 g, 0.264 mmol). ^{1}H NMR (300 MHz, $CDCl_3$): 7.46 (dd, 8H, J = 8.1, J = 2.4), 7.26 – 7.35 (m, 6H), 7.13 (t, 8H, J = 7.2), 6.85 (t, 1H, J = 7.5), 6.56 (d, 2H, J = 8.4), 4.14 (d, 4H, J_{PH} = 19.8), 2.56 (bs, 4H). ^{31}P{^{1}H} NMR (121.498 MHz, $CDCl_3$): 10.32 (s) with satellites at 25.11 and -4.46 (J_{PtP} = 1796.96 Hz). HRMS (ESI) calculated for $C_{34}H_{33}ClNP_2Pt$ [M – Cl]+ 748.14, found 748.11. Hexanes were layered on a CH_2Cl_2 solution of the product to obtain a crystal suitable for X-ray analysis. Elemental Analysis: calculated for $C_{34}H_{33}Cl_2NP_2Pt$ % C: 52.12, % H: 4.24, % N: 1.79; found % C: 51.37, % H: 3.12, % N: 1.49. Mp: decomposed around 240^{o}C.

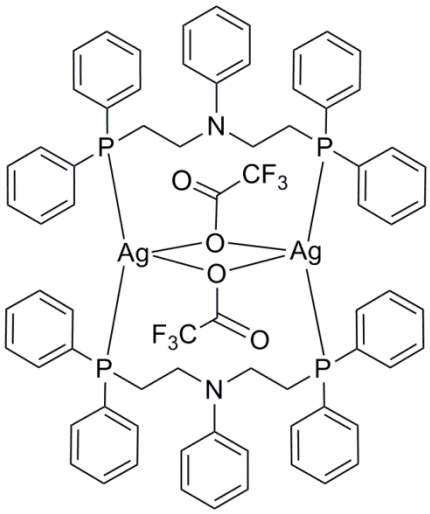

[PNP-AgCF$_3$COO]$_2$ [24]. 3 (0.030 g, 0.058 mmol) was dissolved in 5 ml of dry THF in the glove box. $AgCF_3COO$ (0.013 g, 0.058 mmol) was added to the ligand solution. The mixture was stirred for 3 hours while covered by aluminum foil in the glove

box. Then, the reaction mixture was connected to a Schlenk line, and the solvent was pulled under vacuum to obtain an off-white solid (88%, 0.038 g, 0.026 mmol). ^{1}H NMR (300 MHz, CD_2Cl_2): 7.44 – 7.24 (m, 40H), 7.04 (bs, 4H), 6.56 (bs, 2H), 6.12 (bs, 4H), 3.51 (bs, 8H), 2.58 (bs, 8H). $^{31}P\{^{1}H\}$ NMR (121.498 MHz, CD_2Cl_2): 2.153 (dd, $^{1}J(^{31}P, ^{109}Ag)$ = 520.257, ^{1}J (^{31}P, ^{107}Ag) = 450.516). HRMS (ESI) calculated for monomer $C_{34}H_{33}AgNP_2$ $[M - CF_3COO]^+$ 626.11, found 626.1; HRMS (ESI) calculated for $C_{68}H_{66}Ag_2ClN_2P_4$ $[M–2(CF_3COO)+Cl]^+$ 1285.2, found 1285.3; HRMS (ESI) calculated for $C_{72}H_{66}Ag_2F_6N_2O_4P_4$ [M] 1476.2, small peak found at 1474.8. Hexanes were layered on a CH_2Cl_2 solution of the product to obtain a crystal suitable for X-ray analysis. Elemental Analysis: calculated for $C_{36}H_{33}AgF_3NO_2P_2$ % C: 58.55, % H: 4.50, %N: 1.90; found % C: 58.87, % H: 4.27, %N: 1.81. Mp: 200°C.

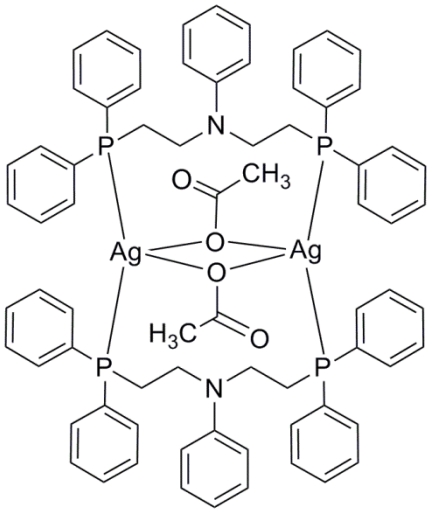

[PNP-AgCH$_3$COO]$_2$ [25]. Prepared the same way as **24**. Off-white solid (85%, 0.080 g, 0.058 mmol) ^{1}H NMR (300 MHz, CD_2Cl_2): 7.52–7.23 (m, 40H), 7.05 (t, 4H, J = 8.4), 6.61 (bs, 2H), 6.25 (bs, 4H), 3.54 (bs, 8H), 2.56 (bs, 8H), 1.91 (s, 6H). $^{31}P\{^{1}H\}$ NMR (121.498 MHz, CD_2Cl_2, 25°C): -2.386 (s). $^{31}P\{^{1}H\}$ NMR (202.348 MHz, CD_2Cl_2 27°C): -1.49 (s). $^{31}P\{^{1}H\}$ NMR (202.348 MHz, CD_2Cl_2, -40°C): -1.43 (dd, $^{1}J(^{31}P, ^{109}Ag)$

= 493.729, $^{1}J(^{31}P, ^{107}Ag)$ = 427.764). $^{31}P\{^{1}H\}$ NMR (202.348 MHz, CD_2Cl_2,-80°C): -2.44 (d, J = 467.829). HRMS (ESI) calculated for $C_{70}H_{69}Ag_2N_2O_2P_4$ $[M - CH_3COO]^+$ 1310.24, found 1310.20. Hexanes were layered on a CH_2Cl_2 solution of the product to obtain a crystal suitable for X-ray analysis. Elemental Analysis: calculated for $C_{36}H_{36}AgNO_2P_2$ % C: 63.17, % H: 5.30, %N: 2.05; found % C: 62.49, % H: 5.23, %N: 1.89. Mp: 183°C.

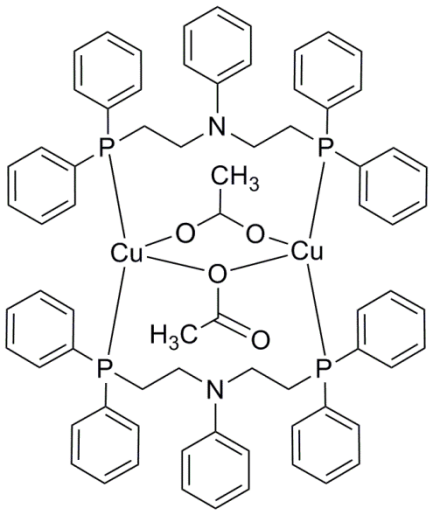

[PNP-CuCH$_3$COO]$_2$ [26]. $Cu(CH_3COO)_2$ (0.011 g, 0.058 mmol) was transferred into a Schlenk flask in the glove box. 5 ml of dry THF was added; the mixture was stirred but did not dissolve. **3** (0.030 g, 0.058 mmol) was added to the mixture, and the Schlenk flask was connected to a Schlenk line, then heated to reflux for 3 hrs under N_2 to obtain a teal solution. The solvent was pulled under vacuum to obtain a light teal solid (78%, 0.029 g, 0.023 mmol). ^{1}H NMR (300 MHz, CD_2Cl_2): 7.59 (bs, 4H), 7.19 - 7.04 (m, 40H), 6.73 (bs, 2H), 6.39 (bs, 4H), 3.41 (bs, 8H), 2.50 (bs, 8H), 1.88 (s, 6H). $^{31}P\{^{1}H\}$ NMR (121 MHz, CD_2Cl_2): -12.9 (s). HRMS (CI+) calculated for monomer $C_{36}H_{37}CuNO_2P_2$ $[M + H]^+$ 640.16, found 639.15. LRMS (ESI) calculated for $C_{68}H_{66}ClCu_2N_2P_4$ 1197.24, found 1196.67. Hexanes were layered on a CH_2Cl_2 solution

of the product to obtain a crystal suitable for X-ray analysis Elemental Analysis: calculated for $C_{36}H_{36}CuNO_2P_2$ % C: 67.54, % H: 5.67, %N: .2.19; found % C: 64.96, % H: 4.90, %N: 1.92. Mp: 95°C.

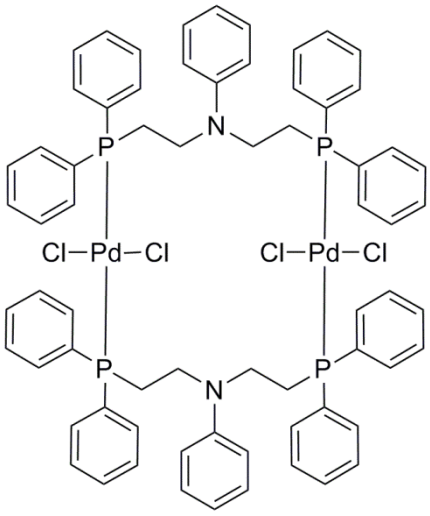

[PNP-PdCl$_2$]$_2$ [27]. Ligand **3** (0.200 g, 0.386 mmol) and bis-benzonitriledichloropalladium (II) (0.148 g, 0.386 mmol) were weighed into separate Schlenk flasks in the glove box, then connected to a Schlenk line. Dry benzene was cannula-transferred into both flasks, which were then stirred. The solution containing palladium was refluxed to obtain a light orange solution. The ligand solution was cannula-transferred into the refluxing metal solution. The reaction mixture was refluxed for 1 hour to obtain a yellow precipitate and an orange solution. The mixture was cooled to room temperature under N_2 while being stirred. The precipitate and the solution were separated by cannula filtering, and then both were dried under vacuum. The yellow precipitate was mostly insoluble, so it was not suitable for NMR. The dried orange solution was redissolved in CH_2Cl_2 and hexanes were layered to obtain large, prismatic dark yellow, X-ray quality crystals (65%, 0.1745 g, 0.251 mmol). ^{1}H NMR (300 MHz, CD_2Cl_2): 7.77 (bs, 16H), 7.50 – 7.40 (m, 24H), 6.84 (m, 4H), 6.46 (m, 2H), 5.71 (m,

4H), 3.64 (bs, 8H), 2.73 (bs, 8H). $^{31}P\{^{1}H\}$ NMR (121 MHz, CD_2Cl_2): 10.92 (s). HRMS (ESI) calculated for monomer $C_{34}H_{33}ClNP_2Pd$ $[M - Cl]^+$ 660.08, found 660.079. Elemental Analysis: calculated for $C_{34}H_{33}Cl_2NP_2Pd$ % C: 58.77, % H: 4.79, %N: 2.02; found % C: 58.52, % H: 4.02, %N: 1.88. Mp: decomposed around 165°C.

$PdCl_2$ was used as a second approach for the synthesis of **27**. 12 mL CH_2Cl_2 was added to $PdCl_2$ (0.030 g, 0.168 mmol). The mixture was stirred, but $PdCl_2$ was slightly soluble. Ligand **3** (0.087 g, 0.168 mmol) was added into the mixture, which was stirred for 3 hours in the glove box. The solvent was evaporated under a Schlenk line to afford a dirty orange residue. The residue was dissolved in CH_2Cl_2, and hexanes were layered to obtain large, prismatic, dark yellow crystals, which yielded the same crystal structure as the other method.

RESULTS AND DISCUSSION

Syntheses

The title complexes of **3** with platinum, palladium, silver, and copper were synthesized as outlined in **Scheme 7** and characterized. The ligand **3** was prepared according to the method reported by Kostas.[38] Complexes of **3** only with rhodium, rhenium, and palladium were reported [38, 62, 67] and we studied molybdenum complexes of **3** in chapter 2. In the syntheses of **23**–**27**, one equivalent of salt was reacted with one equivalent of **3**, to afford good yields of the products (65–94.2%); however, in the synthesis of **22**, the metal to ligand ratio was 0.5, to give a 57.4% yield of the product. Crystallization was used as the purification technique for all complexes. Characterizations of complexes were done by ^{1}H NMR, ^{31}P {^{1}H} NMR, MS, EA, and X-ray crystallography. Both ^{1}H NMR and ^{31}P{^{1}H} NMR signals of **22**–**27** show different patterns and chemical shifts with respect to those found for the free ligand **3**, confirming the existence of complexes in the solution.

Complex **22** was previously reported, but not crystallographically characterized. We have reproduced the complex and crystallized it as orange X-ray quality crystals. The attempt to make an electropolymerizable version of **22** for a heterogeneous catalyst application by using the ligand **14** (chapter 3) was not successful. In the syntheses of **22**–**27**, **22** is the only complex in which the metal has a zero oxidation state, and **23** is the only complex that is ionic. An oligomer has been reported with PNP-Pd coordination, in which dimeric and monomeric coordinations of Pd^{2+} are alternating.[40] The individual dimeric complexes were not prepared in that journal article. We have successfully synthesized the dimeric complex **27** and have obtained the crystal structure from large yellow prismatic crystals. Complexes **22** and **27** are both PNP-Pd complexes, yet Pd has different oxidation states and coordination modes. The synthesis of the monomeric

complex in which the oxidation state of palladium is +2 was not obtained, although an example was previously reported.[139] Different reaction conditions and Pd starting materials resulted in complex **27**. Complex **26**, which has two Cu (I) centers, is obtained by using a Cu (II) source. When the same reaction was tried by using $CuCH_3COO$ instead of $Cu(CH_3COO)_2$, the reaction was unsuccessful.

An exchange of the dba ligand of **22** was attempted with carbonyl ligands by bubbling CO (g) through a concentrated solution of **22** in a screw top NMR tube which was cooled to 0^oC to increase the solubility of the gas. The reaction was monitored by $^{31}P\{^1H\}$ NMR. Again, the identity of any resulting product is inconclusive, since the NMR spectrum of the complex was collapsed into a broad singlet, while $^{31}P\{^1H\}$ NMR spectrum of **22** shows a doublet.

Ligand **3** resulted in all different coordination modes with different metals, i.e. monomeric tridendate (PNP) as in **23**, monomeric bidentate (PP) as in **22**, dimeric bidentate (PP) as in **27**, and dimeric bidentate (PP) with two bridges as in **24**, **25**, and **26**. Bidentate versus tridentate coordination modes are determined by the donor strength of the hemilabile N atom of **3** as well as the anion. Donor strength of N can be tuned by attaching different R groups to it for applications such as catalysis and molecular materials.[40] A result of bridged (tetrahedral) versus square planar coordination mode is due to crystal-field stabilization energy of the metal complex. Especially for platinum and palladium, the observed geometry is square planar, because the crystal-field stabilization energy of a square planar geometry is the highest for platinum and palladium.[77] On the other hand, for silver and copper both tetrahedral and square planar geometries are observed in the literature, depending on the resulting crystal-field stabilization energy of the complex.[77]

Scheme 7. Synthesis of silver, copper, platinum, and palladium complexes of PNP ligand. a) Pd_2dba_3, dry THF, RT, under N_2, 12 hrs; b) $(PhCN)_2PtCl_2$, dry benzene, reflux, under N_2, 1.5 hrs; c) $AgCF_3COO$, dry THF, RT, under N_2, 3hrs, dark; d) $AgCH_3COO$, dry THF, RT, under N_2, 3 hrs, dark; e) $Cu(CH_3COO)_2$, dry THF, reflux, under N_2, 3 hrs; f) $(PhCN)_2PdCl_2$, dry benzene, reflux, under N_2, 1 hr, or $PdCl_2$, dry CH_2Cl_2, RT, under N_2, 3 hrs.

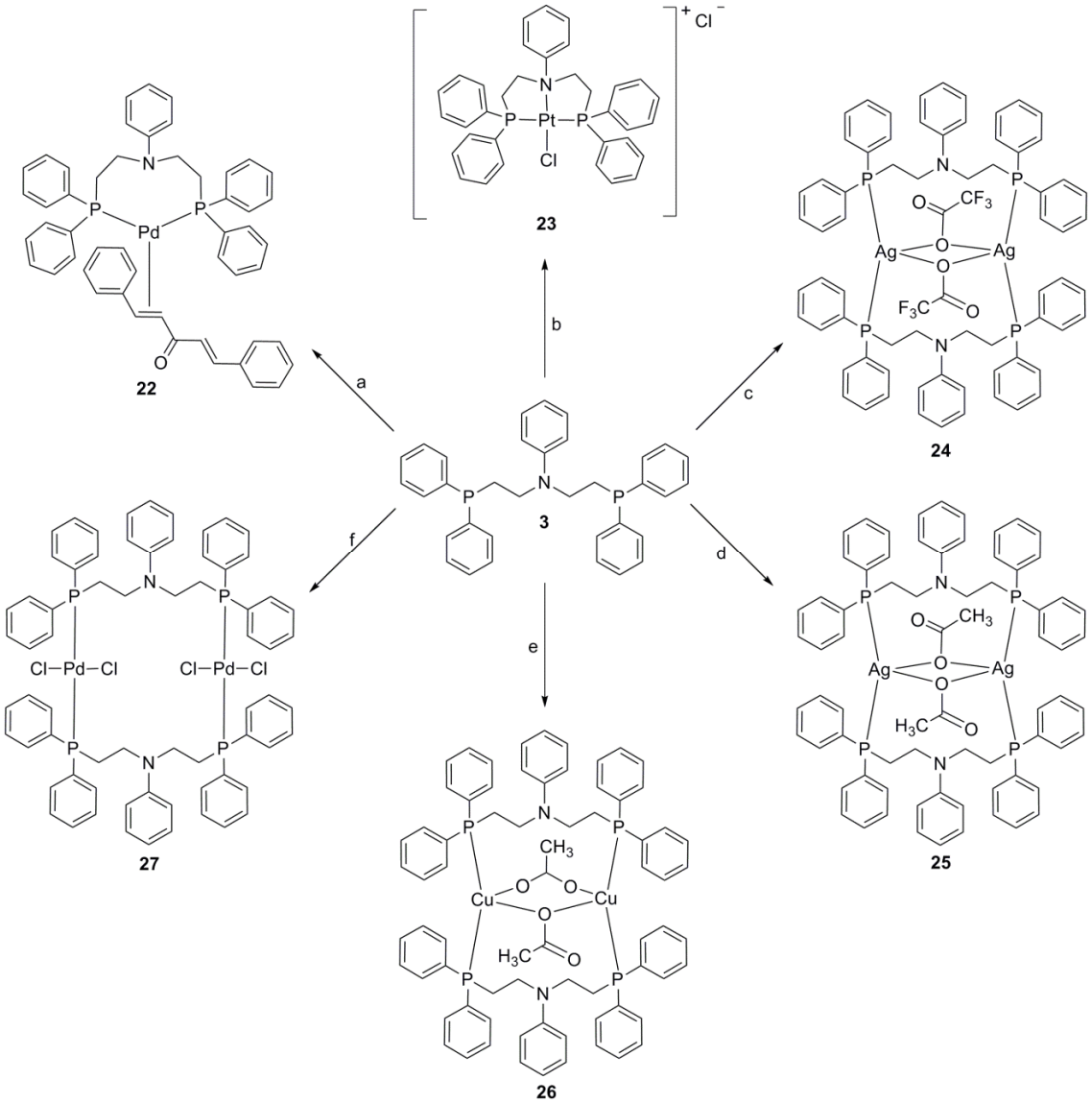

Oxidation of **3** upon exposure to air was tested both in solution and solid state; surprisingly phosphorus atoms were not oxidized, as traced by $^{31}P\{^{1}H\}$ NMR. On the other hand, during metallation reactions, phosphorus atoms of **3** oxidize; therefore metallation reactions were done in oxygen-free media, i.e. a glove box and a Schlenk line under nitrogen.

The synthesis of a PNP-Au complex both with Au (I) and Au (III) was not achieved. Syntheses of complexes containing Fe, Ru, Rh, Ir, Ni also were attempted, but the complexes were not isolated or identified (**Scheme 8-10**). PNP complexes of Fe(0) and Ru(0), which were dark green and orange respectively, were seen only in $^{31}P\{^{1}H\}$ NMR; reaction with iron resulted in a major peak at 56.67 ppm and a minor peak at 68.29 ppm, although the free ligand appears at –20 ppm. Reaction of **3** with $Ru_3(CO)_{12}$ resulted in 4 peaks: 40 ppm (main), 35 ppm, 28 ppm, and 23 ppm. Both Fe(0) and Ru(0) product mixtures were crystallized; unfortunately, crystal qualities were not suitable for X-ray diffraction studies. PNP complexes of rhodium and iridium resulted in many products that could not be isolated, which were observed in $^{31}P\{^{1}H\}$ NMR as separate peaks. Finally, the reaction with nickel resulted in a red compound. $NiCl_2.6H_2O$ is green; when the ligand solution was added to the solution of Ni^{2+}, an immediate color change occurred, which was promising, but the product could not be identified. ^{1}H NMR in which peaks were concentrated in the aliphatic region as big broad peaks may have been caused by a paramagnetic product; nonetheless, EPR did not show any peak. Surprisingly, no peak was observed in $^{31}P\{^{1}H\}$ NMR spectrum. Crystallization attempts did not result in any crystals suitable for X-ray diffraction. Therefore attempted syntheses of complexes of these metals remain inconclusive (**Scheme 9**).

Scheme 8. Proposed structures for iron (0) and ruthenium (0) complexes of **3**

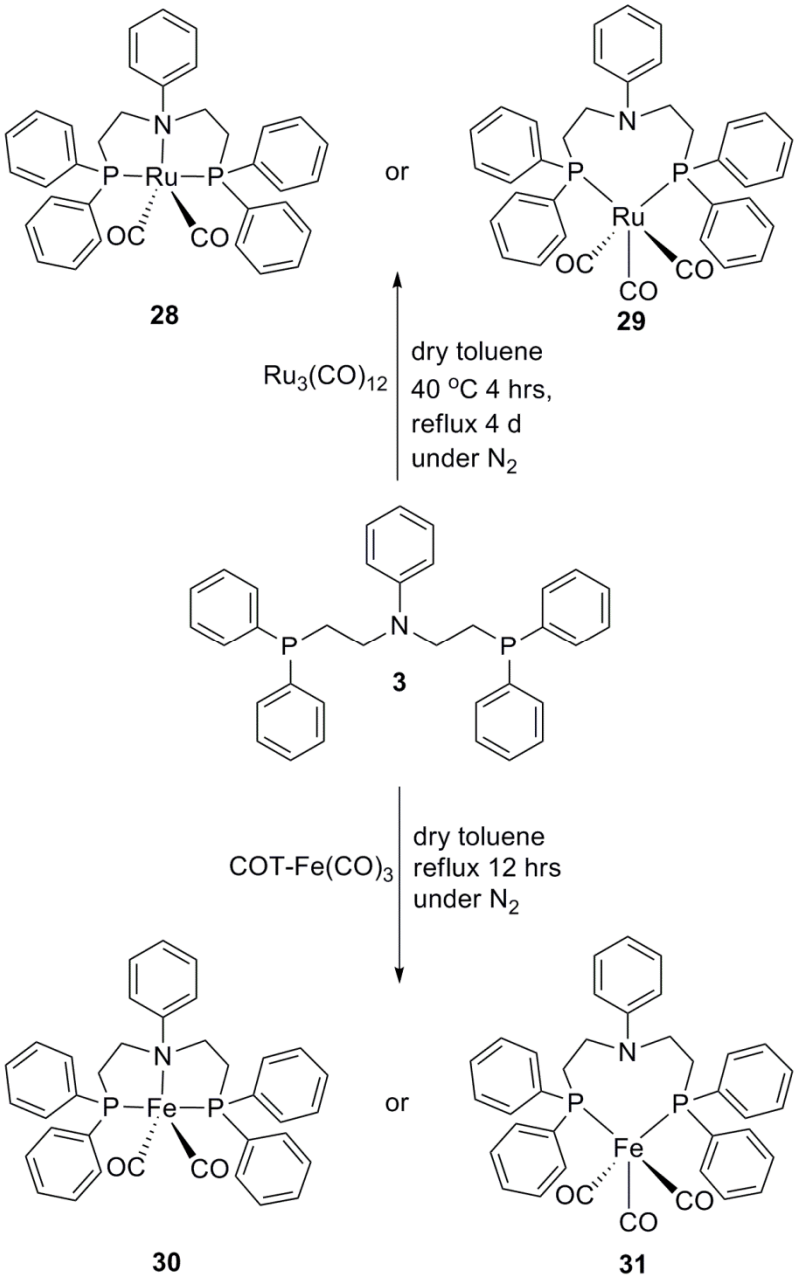

Scheme 9. Proposed structures for nickel (II) and ruthenium (II) complexes of **3**

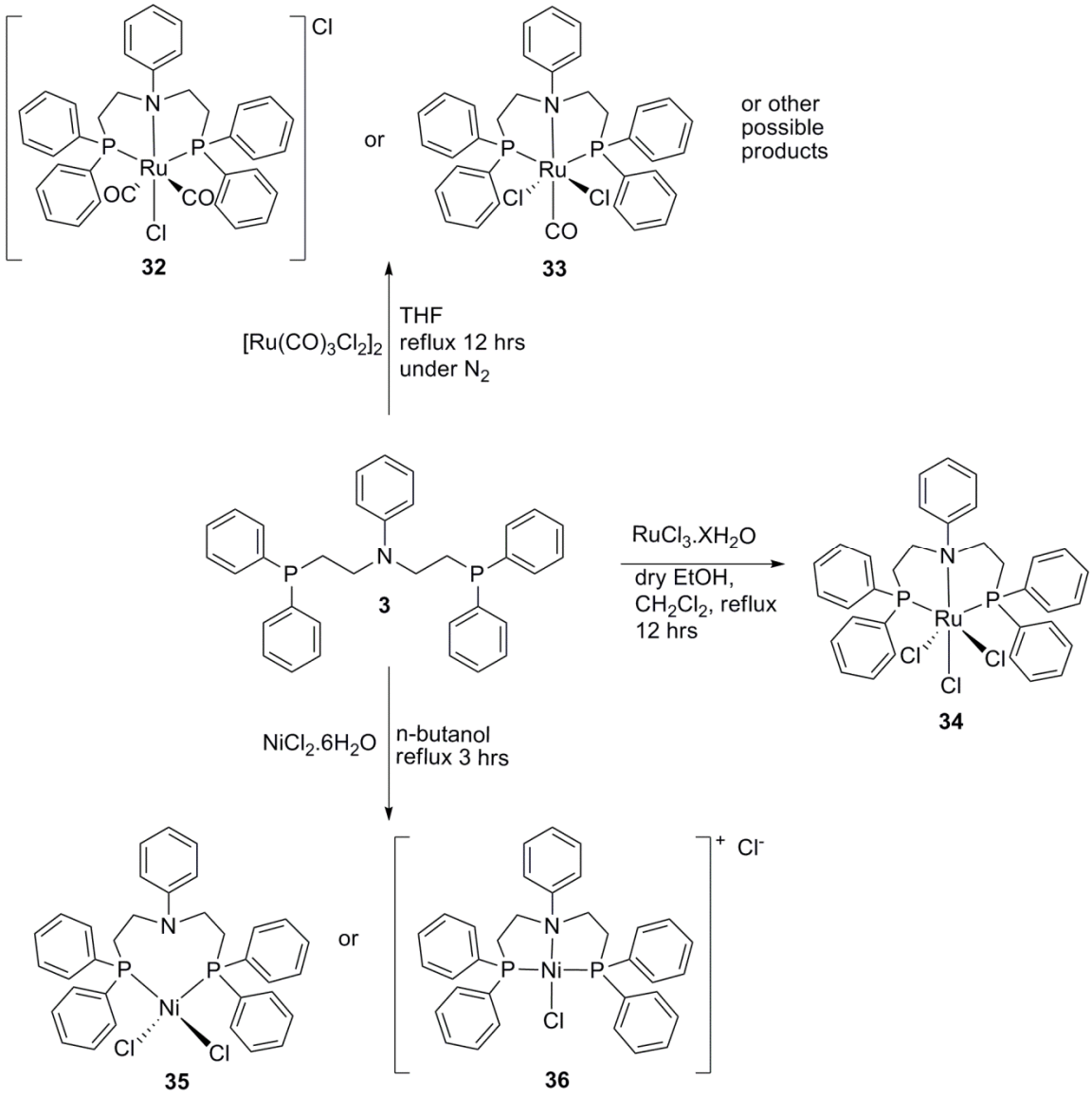

Scheme 10. Proposed structures for rhodium (I) and iridium (I) complexes of **3**

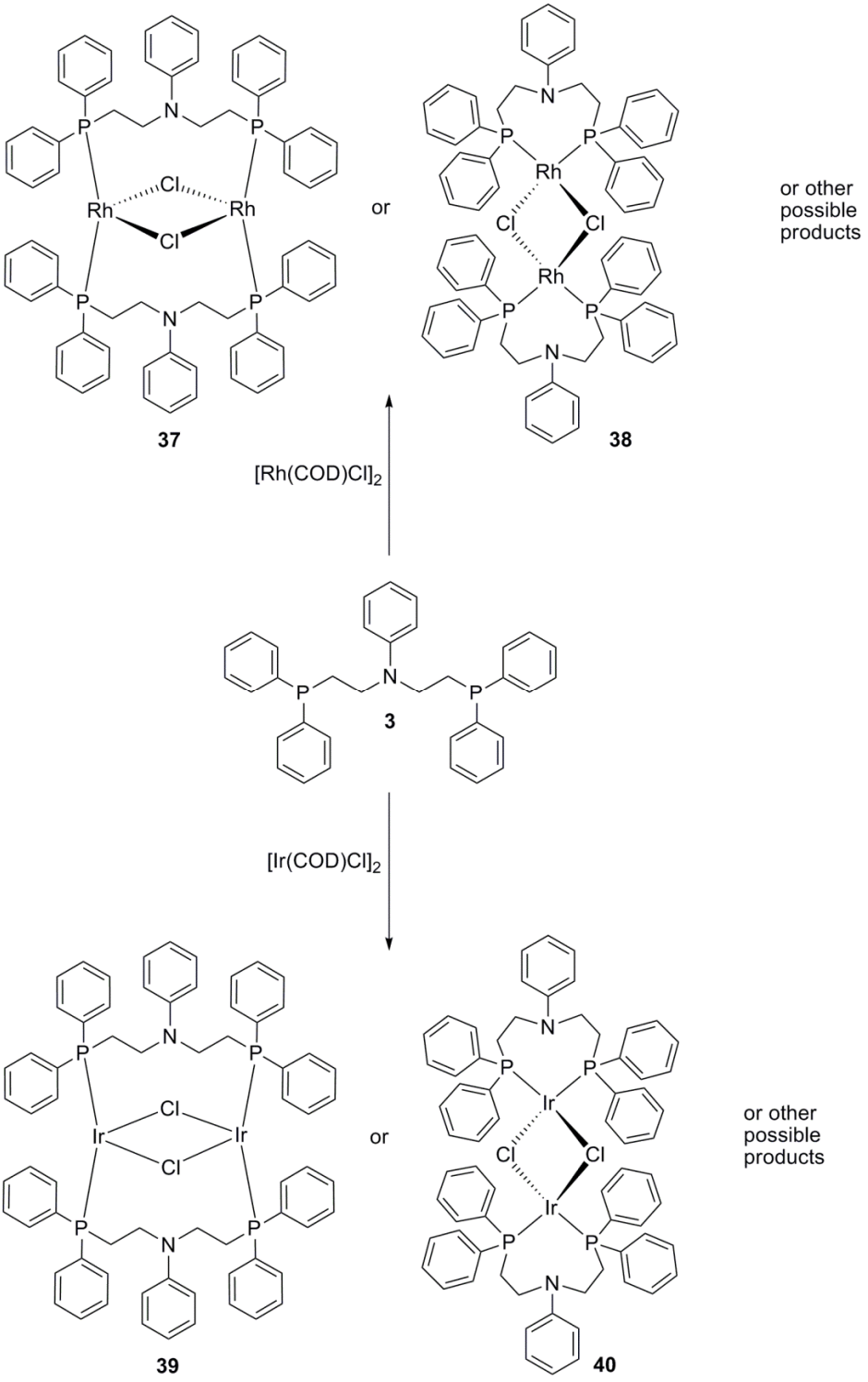

NMR Studies of Complexes with Silver

Two different PNP-Ag complexes have been synthesized, i.e. **24** and **25**. These complexes differ only in the anions, which are CF_3COO^- and CH_3COO^-, respectively. Chemical shifts and coupling constants are reported in the Experimental section. Both complexes crystallized in a bridged dimer structure. In **25** (**Figure 51b**), acetate anions were replaced by chloride anions, which probably occurred when the solution of **25** in CH_2Cl_2 was filtered through celite, prior to crystallization. HRMS and EA data of **25** prove that the compound has an acetate anion, and the $-CH_3$ group of the acetate was also observed in ^1H NMR.

The $^{31}P\{^1H\}$ NMR spectra of the two complexes are different at RT, as taken using a 300 MHz instrument. **24** has a doublet of doublets at 2.153 ppm at RT; however, **25** shows a broad singlet at -2.39 ppm (**Figure 48**). ^{31}P NMR of **24** support that the dinuclear structure is also stable in solution, and the ^{31}P-Ag coupling constant is in the range typical to $[Ag(P_2 - donor)]_2X_2$ or $[Ag(\mu\text{-}X)_2(P_2 - donor)]_2$ systems, where X is the anion.[152] Reports of similar complexes in the literature, in which the phosphorus donors are linked by $CH_2\text{-}(CH_2)_n\text{-}CH_2$ groups, have indicated that when the anion is a perchloro or trifluoromethanesulfonate derivative, the *J* (^{31}P, Ag) coupling constant is in the range of 420 –580 Hz, and the chemical shifts are greater than for the halide or pseudohalide analogues; these observations demonstrate that the counter anion has an effect on the strength of the Ag–P bond. When the anion is a halide or acetate, a broad singlet is always observed at room temperature in $^{31}P\{^1H\}$ NMR spectra, because the species are fluxional. Their low-temperature $^{31}P\{^1H\}$ NMR spectra resolve into a doublet or a doublet of doublets, which has coupling constants in the range of 350–450 Hz.[152] These findings are thoroughly consistent with our results.

When the $^{31}P\{^{1}H\}$ NMR spectrum of **25** was taken by using a 500 MHz instrument, a broad singlet was observed at RT; the spectrum displays a well-resolved doublet of doublets, with large *J* values of 493.729 Hz and 427.764 Hz at low temperature (–40°C). Coupling constants are smaller than $^{31}P\{^{1}H\}$ NMR of **24**, with *J* values of 520.257 and 450.516 Hz. When the same sample of **25** was cooled further to –80 °C, resolution of the peaks deteriorated and only a doublet was seen with a *J* value of 467.829 Hz (**Figure 49**). These large coupling constants and a coupling constant of **25** (X = CH_3COO^-) smaller than **24** (X = CF_3COO^-) are consistent with the literature.[152]

a) b)

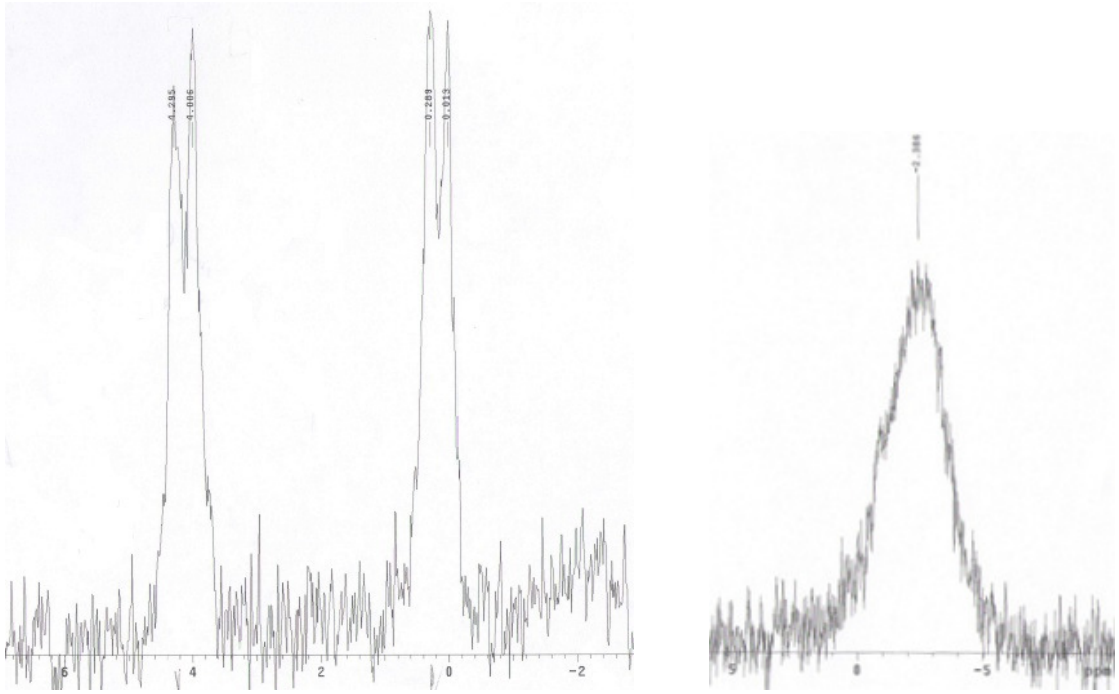

Figure 48. $^{31}P\{^{1}H\}$ NMR spectra of a) **24** b) **25** taken at RT using a 300 MHz instrument.

a)

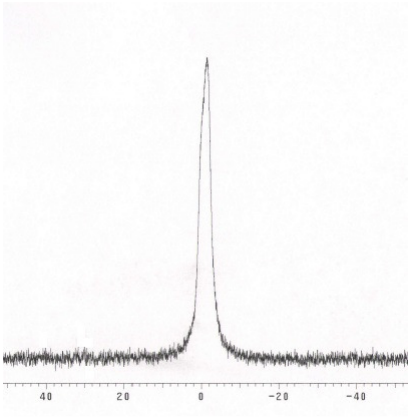

b)

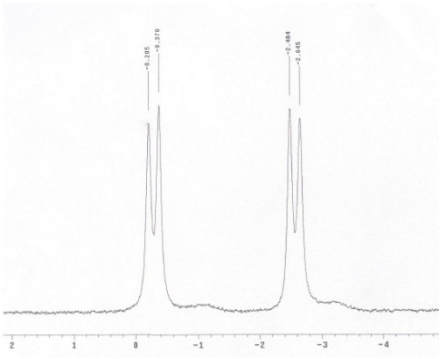

c)

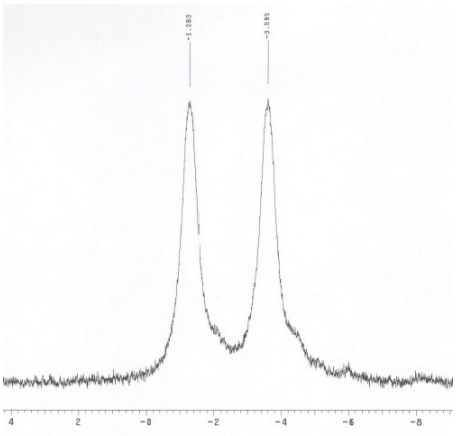

Figure 49. $^{31}P\{^{1}H\}$ NMR spectra of **25** a) at RT b) at -40^{o}C c) at -80^{o}C taken by using a 500 MHz instrument.

Mass Spectrometry of Complexes

The structure of dimers in the solution state was examined. Some journal articles reported similar structures as dimers in solution, identified by mass spectra as the main peak, but in our case, the m/z values of dimers did not correspond to the main peak. It is hard to prove with mass spectrometry whether or not the solution structure is a dimer, because dimers can certainly be split in the medium. For complex **24**, dimers split into monomers in MS medium, and the corresponding peak is dominant; the peak corresponding to the dimer exists, but is quite small. In addition, a peak at 1285.3 was observed, corresponding to a dimer in which two trifluoroacetate groups have been replaced by only one chloride. The chloride may come from the solvent CH_2Cl_2. For complex **25**, on the other hand, we observed a main peak that corresponds to a dimer that has lost only one acetate group. Complex **26** showed a main peak that corresponds to the monomer in the high resolution CI+ spectrum. The dimer that had lost two acetate groups and had two copper metals linked by a bridging chloride showed up in the LRMS (ESI). HRMS (ESI) of **27** showed that the dimer was split and had lost one of its chlorides. No trace of the dimer was observed for **27**.

Complex **22** was well observed in the MS medium. Complex **23** is a cationic complex with a non-coordinating chloride anion. Both LRMS and HRMS showed only the cation.

Crystal Structures of Complexes

The solid state structures of complexes **22–27** were determined by X-ray crystallographic structure determination, and the resulting ORTEP representation can be seen in **Figures 50–53**. All crystals were obtained by slow diffusion of hexanes into saturated solutions of **22–27** in CH_2Cl_2. Crystallographic and structural refinement data

are given in **Tables 14** and **15**, and selected bond angles and distances around the metal centers are given in **Tables 16–21**.

In complex **22**, the Pd(0) atom is coordinated in a trigonal planar geometry formed by two P atoms of ligand **3** and a C=C (η^2) bond involving the C atoms in the α,β positions relative to the central ketone of the dibenzylideneacetone ligand. The molecular structure of **22** is shown in **Figure 50a**. The angle between the Pd–P1–P2 and Pd–C41–C42 planes is 1.40°. Ligand **3** is in a monomeric (PP) binding mode in which the nitrogen atom of the ligand is not bound to the metal center (distance between N1 and Pd1 is 3.405 Å). The average Pd–P bond length is 2.326 Å, which is consistent with similar structures reported in the literature.[153, 154] Dibenzylideneacetone (dba) is bound to Pd via one of the carbon-carbon double bonds, with the C41=C42 bond (1.411 (3)Å) slightly elongated due to complexation when compared to C44=C45 (1.327 (3) Å), and the C41=C42 centroid-Pd distance is 2.044 Å. Similar Pd(0) coordination environments have been previously reported with chelating diphosphine and dba ligands, which also display the elongated carbon-carbon double bond (1.417 (3) Å).[153] This coordination mode is not surprising, since Pd_2dba_3 is the metal precursor used in the synthesis of **22** and includes two palladium atoms with each metal bound η^2 to the three dba ligands.

In complex **23**, the four-coordinate Pt(II) lies in the center of a slightly distorted square-planar environment. The coordination environment around the metal center is defined by two phosphorus atoms from the PNP ligand, one nitrogen atom from the same ligand, and a chloride anion as a monodentate ligand. The other chloride anion is not coordinated to platinum to give an ionic complex structure. Phosphorus atoms are *trans* to each other. Pt–P, Pt–N and Pt–Cl bonds are consistent with the reported values as well as the angles around the metal center.[155] The sole difference is that the literature complex has anionic nitrogen, so the Pt–N distance is shorter.

In complexes **24** and **25**, the four-coordinate Ag(I) centers form bridged structures through trifluoroacetate and chloride anions, respectively. Two acetate groups of **25** were replaced with two chloride anions during crystallization, probably from the solvent CH_2Cl_2 or from being filtered through celite. The geometries of Ag(I) centers are distorted tetrahedral. The coordination environment around the metal center is defined by two phosphorus atoms from the separate PNP ligands and two bridging trifluoroacetate anions for **24** or two bridging chloride anions for **25** (acetates were replaced by chlorides during crystallization) (**Figure 51**). In order to find whether or not the solid state powder structure of **24** is a dimer, powder X-ray data were examined together with the powder X-ray data predicted from the crystal structure. The fact that the two sets of data are matching is proof of a dimeric structure in the solid state. The bond distances and the angles around the Ag atoms are consistent with the reported values for a similar structure to **24**.[152] A literature complex similar to **25** has consistent values for bond distances, yet there are some differences in bond angles due to structural differences in the ligand, i.e. ferrocene.[156]

In complex **26**, the four-coordinate Cu(I) centers form bridged structures through acetate and/or chloride anions, i.e. a disorder in the crystal structure. The geometry of Cu(I) centers are distorted tetrahedral. The coordination environment around the metal center is defined by two phosphorus atoms from separate PNP ligands and two bridging acetate anions in bidentate and monodentate modes or a bridging chloride anion, such that half of the time one of the bridging ligands was seen as monodentate acetate, whereas half of the time it was seen as a bridging chloride (**Figure 52**). The bond distances and the angles around the Cu atoms are consistent with the reported values for the similar structures.[152, 157] In complex **27**, the four-coordinate Pd(II) centers form a dimeric structure without any bridging ligands. The geometries of Pd(II) centers are

distorted square planar, with a P(1)–Pd(1)–P(2) angle of 173.25(6)^{o}. The coordination environment around the metal center is defined by two phosphorus atoms from the separate PNP ligands and chloride anions. The phosphorus atoms are *trans* to each other as are the chlorides. The Pd–P and Pd–Cl distances are very close to the reported average value, but the P–Pd–P angle is wider by 7.47^{o} and the Cl–Pd–Cl angle is wider by 9.89^{o} than for the literature complex.[62]

a)

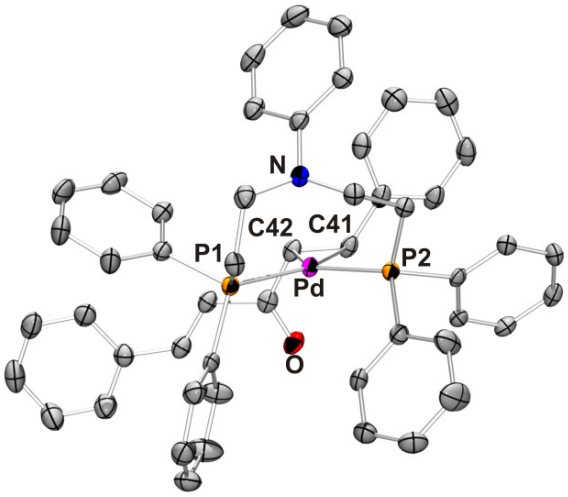

b)

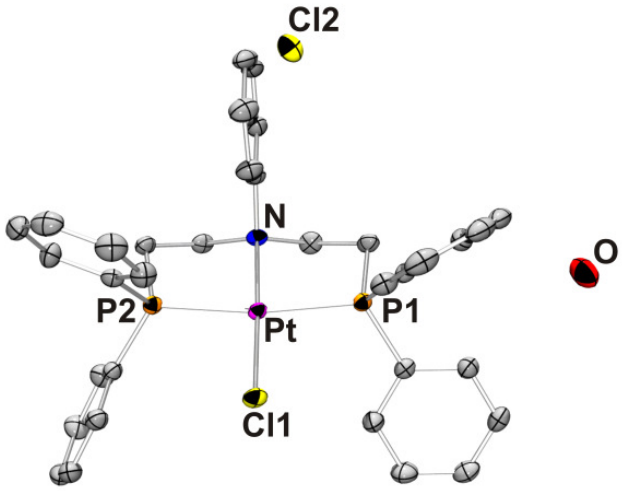

Figure 50. View of a) **22** b) **23** showing the labeling of selected atoms. Hydrogen atoms have been omitted for clarity. Displacement ellipsoids are scaled to the 50% probability level.

a)

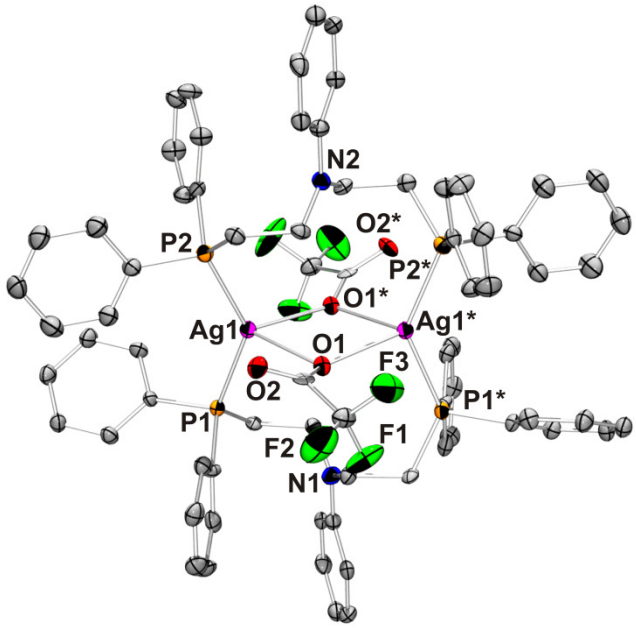

b)

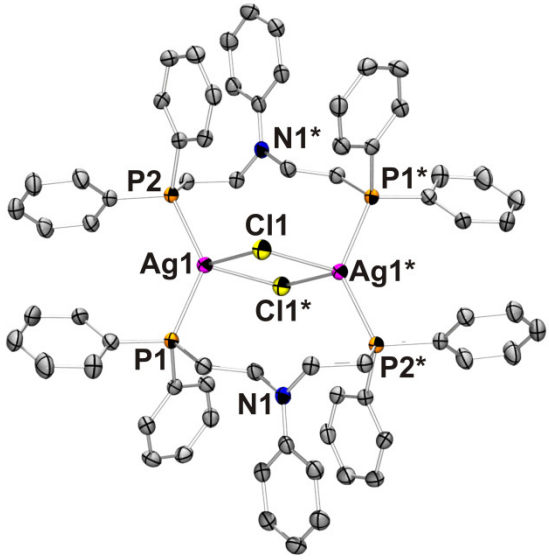

Figure 51. View of a) **24** b) **25** showing the labeling of selected atoms. Hydrogen atoms have been omitted for clarity. Displacement ellipsoids are scaled to the 50% probability level.

a)

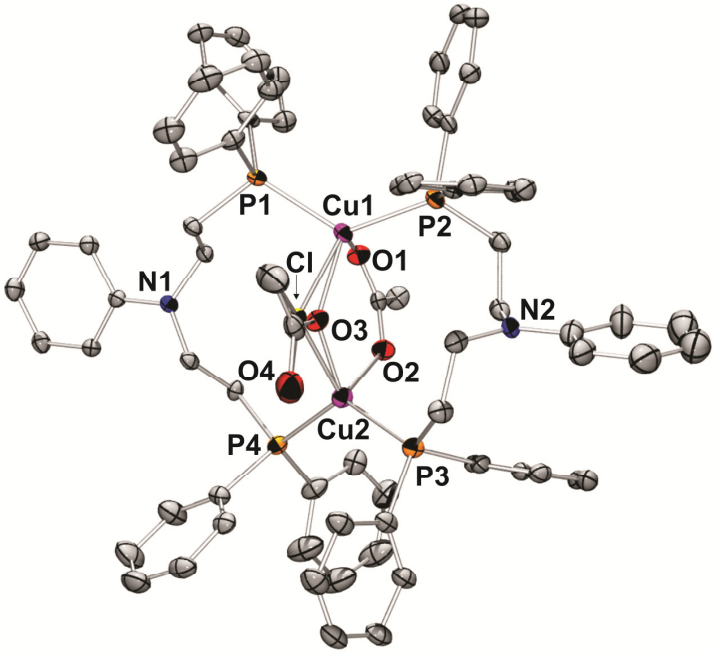

b)

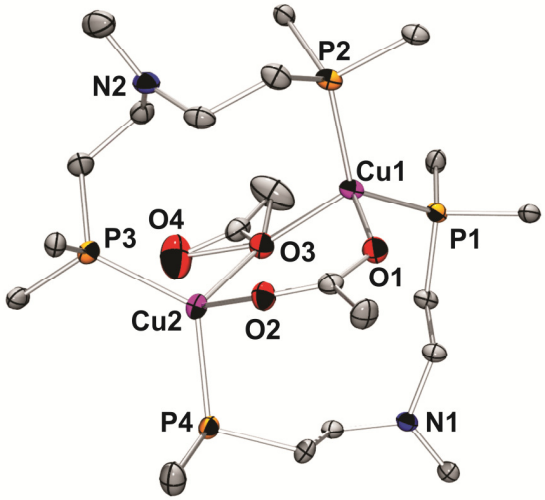

c)

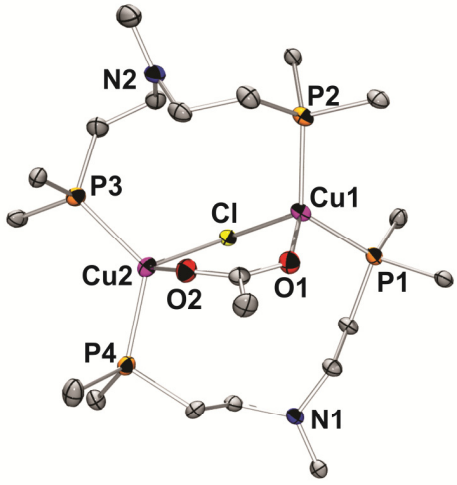

Figure 52. View of **26** showing the labeling of selected atoms. Hydrogen atoms have been omitted for clarity. a) whole structure with two acetate groups b) only coordination environment with two acetate groups c) only coordination environment with one acetate and one chloride. Displacement ellipsoids are scaled to the 50% probability level.

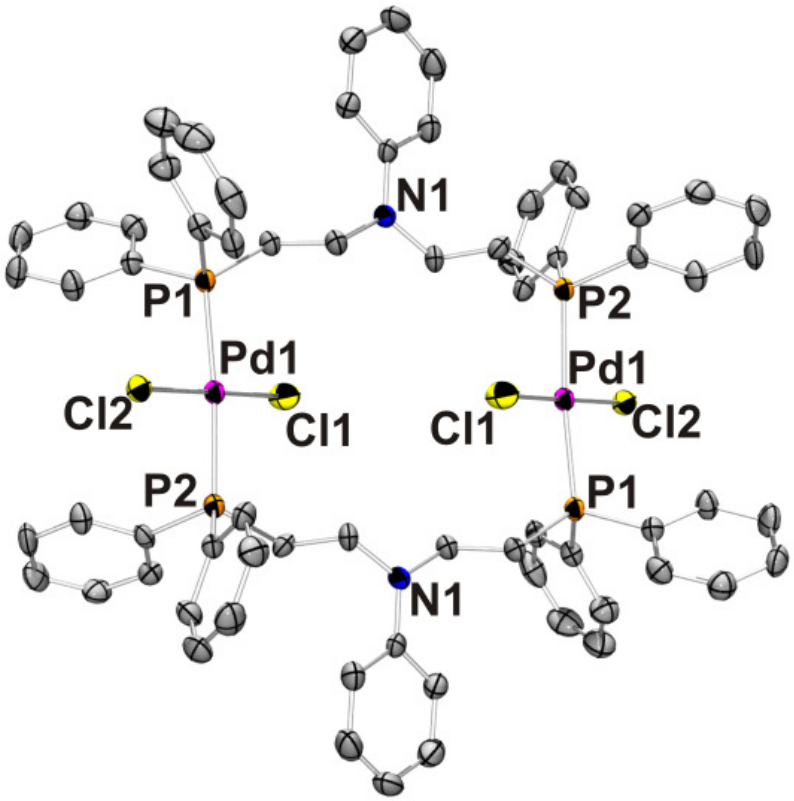

Figure 53. View of **27** showing the labeling of selected atoms. Hydrogen atoms have been omitted for clarity. Displacement ellipsoids are scaled to the 50% probability level.

Table 14. Crystal data and structure refinement of platinum and palladium complexes.

	22	**23**	**27**
Formula	$[Pd(C_{34}H_{33}NP_2)(C_{17}H_{14}O)]$	$C_{34}H_{33}Cl_2NOP_2Pt$	$C_{68}H_{66}Cl_4N_2P_4Pd_2.2CH_2Cl_2$
FW	858.24	799.54	1559.56
T (K)	153	233	150(2)
Crystal system	Triclinic	Monoclinic	Triclinic
Space group	*P -1*	$P2_1/c$	*P -1*
a (Å)	10.087 (2)	9.9989(7)	9.291(2)
b (Å)	11.974 (2)	20.0285(18)	14.571(2)
c (Å)	17.473 (4)	17.9269(13)	15.196(3)
α (deg)	86.34 (3)	90	62.071(4)
β (deg)	81.27 (2)	119.840(4)	89.684(8)
γ (deg)	83.15 (3)	90	82.932(4)
V (Å^3)	2068.8 (7)	3114.1(4)	1800.6(6)
Z	2	4	1
ρ (g/cm^3)	1.378	1.705	1.438
μ (mm^{-1})	0.57	4.809	0.926
F(000)	888	1576	792
Crystal size (mm)	0.27 x 0.14 x 0.12	0.20 × 0.20 × 0.20	0.26 x 0.10 x 0.10
θ (deg)	1.0 to 27.5	2.2810 to 27.5437	3.04 to 27.48
Index ranges	$-12 \le h \le 13$ $-14 \le k \le 15$ $-22 \le l \le 22$	$-12 \le h \le 12$ $-26 \le k \le 25$ $-23 \le l \le 23$	$-12 \le h \le 12$ $-16 \le k \le 18$ $0 \le l \le 19$
Absorption correction	Multi-scan	Multi-scan	Multi-scan
Max. and min. transmission	1.000 and 0.837	1.0000 and 0.6055	0.9147 and 0.7968
GOF on F^2	1.582	1.142	1.556
$R1$, $R2$ [$I > 2\sigma(I)$]	0.0414, 0.0887	0.0312, 0.0836	0.0727, 0.1858
$R1$, $R2$ (all data)	0.0563, 0.0851	0.0339, 0.0912	0.0966, 0.1925
Largest diff. peak and hole (e.Å^{-3})	1.56 and -0.67	2.071 and -2.556	1.419 and -1.700

Table 15. Crystal data and structure refinement of silver and copper complexes.

	24	**25**	**26**
Formula	$C_{72}H_{66}N_2O_4P_4F_6Ag_2$	$C_{35.38}H_{35.75}Cl_{3.75}AgNP_2$	$C_{71.10}H_{70.65}Cl_{0.45}Cu_2N_2O_{3.10}P_4$
FW	1476.89	777.65	1269.66
T (K)	100(2)	123(2)	123(2)
Crystal system	Orthorhombic	Monoclinic	Monoclinic
Space group	*Pbcn*	$P2_1/c$	$P2_1/c$
a (Å)	13.723(5)	14.318(4)	17.184(5)
b (Å)	22.778(5)	14.345(5)	14.854(5)
c (Å)	20.929(5)	17.993(6)	24.265(8)
α (deg)	90.000(5)	90	90
β (deg)	90.000(5)	105.375(4)	94.731(5)
γ (deg)	90.000(5)	90	90
V (Å^3)	6542(3)	3563(2)	6173(3)
Z	4	2	4
ρ (g/cm^3)	1.499	1.45	1.366
μ (mm^{-1})	0.77	0.96	0.86
F(000)	3008	1583	2647
Crystal size (mm)	0.12 × 0.07 × 0.06	0.24 × 0.18 × 0.05	0.12 × 0.09 × 0.05
θ (deg)	1.73 to 27.50	3.00 to 27.50	3.00 to 27.50
Index ranges	$-17 \le h \le 17$	$-13 \le h \le 18$	$-20 \le h \le 19$
	$-29 \le k \le 29$	$-18 \le k \le 18$	$-17 \le k \le 17$
	$-27 \le l \le 27$	$-23 \le l \le 23$	$-28 \le l \le 28$
Absorption correction	Multi-scan	Multi-scan	Multi-scan
Max. and min. transmission	0.9541 and 0.9145	1.000 and 0.772	1.000 and 0.777
GOF on $F2$	1.631	1.106	1.376
$R1$, $R2$ [I > 2σ (I)]	0.1139, 0.2042	0.0503, 0.1210	0.1171, 0.1668
$R1$, $R2$ (all data)	0.1140, 0.2042	0.0552, 0.1238	0.1383, 0.1739
Largest diff. peak and hole (e.Å^{-3})	0.71 and -0.99	1.27 and -0.85	0.62 and -0.46

Table 16. Selected bond lengths (Å) and angles (deg) of **22**.

Bond Lengths (Å)	
Pd – P(1)	2.3068(10)
Pd– P(2)	2.3441(9)
Pd– C(41)	2.155(2)
Pd – C(42)	2.170(2)
Bond Angles (^{o})	
P(1) – Pd – P(2)	106.54(3)
P(1) – Pd – C(41)	99.11(7)
P(1) – Pd – C(42)	137.21(7)
P(2) – Pd – C(41)	154.31(7)
P(2) – Pd – C(42)	116.24(7)
C(41) – Pd – C(42)	38.09(9)

Table 17. Selected bond lengths (Å) and angles (deg) of **23**.

Bond Lengths (Å)	
Pt – P(1)	2.299(1)
Pt – P(2)	2.291(1)
Pt – Cl(1)	2.2960(7)
Pt – N	2.100(2)
Bond Angles (^{o})	
P(1) – Pt – P(2)	170.68(3)
P(1) – Pt – Cl(1)	96.53(3)
P(1) – Pt – N	85.18(9)
P(2) – Pt – Cl(1)	92.67(3)
P(2) – Pt – N	85.67(9)
Cl(1) – Pt – N	177.61(9)

Table 18. Selected bond lengths (Å) and angles (deg) of **24**.

Bond Lengths (Å)	
Ag(1) – P(1)	2.454(2)
Ag(1) – P(2)	2.434(2)
Ag(1*) – P(1*)	2.454(2)
Ag(1*) – P(2*)	2.434(2)
Ag(1*) – O(1*)	2.441(5)
Ag(1) – O(1)	2.441(5)
Ag(1*) – O(1)	2.466(5)
Ag(1) – O(1*)	2.466(5)
Bond Angles (^{o})	
P(1) – Ag(1) – P(2)	136.28(7)
P(1*) – Ag(1*) – P(2*)	136.28(7)
P(1) – Ag(1) – O(1*)	102.9(1)
P(1*) – Ag(1*) – O(1*)	102.9(1)
P(1) – Ag(1) – O(1)	103.4(1)
P(1*) – Ag(1*) – O(1)	103.4(1)
P(2) – Ag(1) – O(1)	107.3(1)
P(2) – Ag(1) – O(1*)	114.5(1)
P(2*) – Ag(1*) – O(1)	114.5(1)
P(2*) – Ag(1*) – O(1*)	107.3(1)
O(1) – Ag(1) – O(1*)	75.2(2)
O(1) – Ag(1*) – O(1*)	75.2(2)
Ag(1) – O(1) – Ag(1*)	104.4(2)
Ag(1) – O(1*) – Ag(1*)	104.4(2)

Table 19. Selected bond lengths (Å) and angles (deg) of **25**.

Bond Lengths (Å)	
Ag(1)– P(1)	2.493(1)
Ag(1*) – P(1*)	2.493(1)
Ag(1) – P(2)	2.463(1)
Ag(1*) – P(2*)	2.463(1)
Ag(1*) – Cl(1)	2.690(1)
Ag(1) – Cl(1*)	2.690(1)
Ag(1) – Cl(1)	2.726(1)
Ag(1*)–Cl(1*)	2.726(1)
Bond Angles (^{o})	
P(1) – Ag(1) – P(2)	132.89(3)
P(1*) – Ag(1*) – P(2*)	132.89(3)
P(1) – Ag(1) – Cl(1*)	104.34(3)
P(1) – Ag(1) – Cl(1)	99.57(3)
P(1*) – Ag(1*) – Cl(1)	99.57(3)
P(1*) – Ag(1*) – Cl(1*)	104.34(3)
P(2) – Ag(1) – Cl(1)	111.79(3)
P(2*) – Ag(1*) – Cl(1)	112.85(3)
P(2*) – Ag(1*) – Cl(1*)	111.79(3)
P(2) – Ag(1) – Cl(1*)	112.85(3)
Cl(1) – Ag(1) – Cl(1*)	84.02(3)
Cl(1) – Ag(1*) – Cl(1*)	84.02(3)
Ag(1) – Cl(1) – Ag(1*)	95.98(3)
Ag(1) – Cl(1*) – Ag(1*)	95.98(3)

Table 20. Selected bond lengths (Å) and angles (deg) of **26**.

Bond Lengths (Å)	
Cu(1) – P(1)	2.264(2)
Cu(1) – P(2)	2.242(2)
Cu(2) – P(3)	2.258(2)
Cu(2) – P(4)	2.272 (2)
Cu(1) – Cl(1)	2.414(6)
Cu(2) – Cl(1)	2.430(7)
Cu(1) – O(1)	2.055(5)
Cu(2) – O(2)	2.172(5)
Bond Angles (^{o})	
P(1) – Cu(1) – P(2)	125.41(8)
P(1) – Cu(1) – O(1)	105.6(1)
P(1) – Cu(1) – Cl(1)	94.2(2)
P(2) – Cu(1) – O(1)	101.8(1)
P(2) – Cu(1) – Cl(1)	118.9(2)
O(1) – Cu(1) – Cl(1)	110.2(2)
P(3) – Cu(2) – O(2)	111.2(1)
P(4) – Cu(2) – O(2)	93.6(1)
O(2) – Cu(2) – Cl(1)	103.6(2)
P(3) – Cu(2) – P(4)	122.84(8)
P(3) – Cu(2) – Cl(1)	108.3(2)
P(4) – Cu(2) – Cl(1)	114.8(2)

Table 21. Selected bond lengths (Å) and angles (deg) of **27**.

Bond Lengths (Å)	
Pd(1) – P(1)	2.327(2)
Pd(1) – P(2)	2.326(2)
Pd– Cl(1)	2.301(2)
Pd – Cl(2)	2.307(2)
Bond Angles (^{o})	
P(1) – Pd(1) – P(2)	173.25(6)
P(1) – Pd(1) – Cl(1)	89.88(7)
P(1) – Pd(1) – Cl(2)	90.39(6)
P(2) – Pd(1) – Cl(1)	89.58(7)
P(2) – Pd(1) – Cl(2)	90.05(6)
Cl(1) – Pd(1) – Cl(2)	179.07(7)

UV-Vis and Luminescence Studies of Complexes and the Ligand

UV-Vis absorption spectra of complexes **23**–**27** and free ligand **3** were obtained (**Figure 54**). **3** has its absorption maximum at 257 nm with ε = 27437 $M^{-1}cm^{-1}$ for π–π^* transition. Complexes **24**, **25**, and **26** have their absorption maxima very close to the free ligand, observed at 254, 256, and 259 nm with ε values of 55806, 50000, and 75399 $M^{-1}cm^{-1}$, respectively. Since these three complexes are dimers, they absorb UV light to a greater extent than the ligand. Absorption maxima changed only a few nm upon complexation, most likely because the conformation of the ligand and the resulting complexes of **24**, **25** and **26** are similar. The biggest extinction coefficient value belongs to the copper complex **26**. The two silver complexes have values close to each other. When **26** is in solid form, it is very light green and colorless when dissolved in CH_2Cl_2. Complexes **23**, **25**, **26**, and ligand **3** are white both in solid state and in solution state. The only colored complex is **27** with its bright yellow color, and its absorption spectrum has an additional peak at 332 nm with an ε value of 29183 $M^{-1}cm^{-1}$ (**22** is orange, but its UV-Vis spectrum was not measured). For all the other complexes (**23**–**26**), neither MLCT nor LMCT in the visible region of the spectrum were observed. Complex **23** did not show any peak in the 235-800 nm range, but absorption was increasing toward the UV region. $\lambda_{cut-off}$ of the solvent CH_2Cl_2 was 235 nm. The only solvent with a considerably low value of $\lambda_{cut-off}$ = 190 nm was CH_3CN. On the other hand, CH_3CN should not be used for measuring the absorption spectrum of **23**, because a square-planar platinum complex **23** has open coordination sites and CH_3CN can coordinate to the complex. During complexation of **23**, the conformation of ligand **3** changed drastically; this affected the absorption maximum and caused shifting to lower wavelengths.

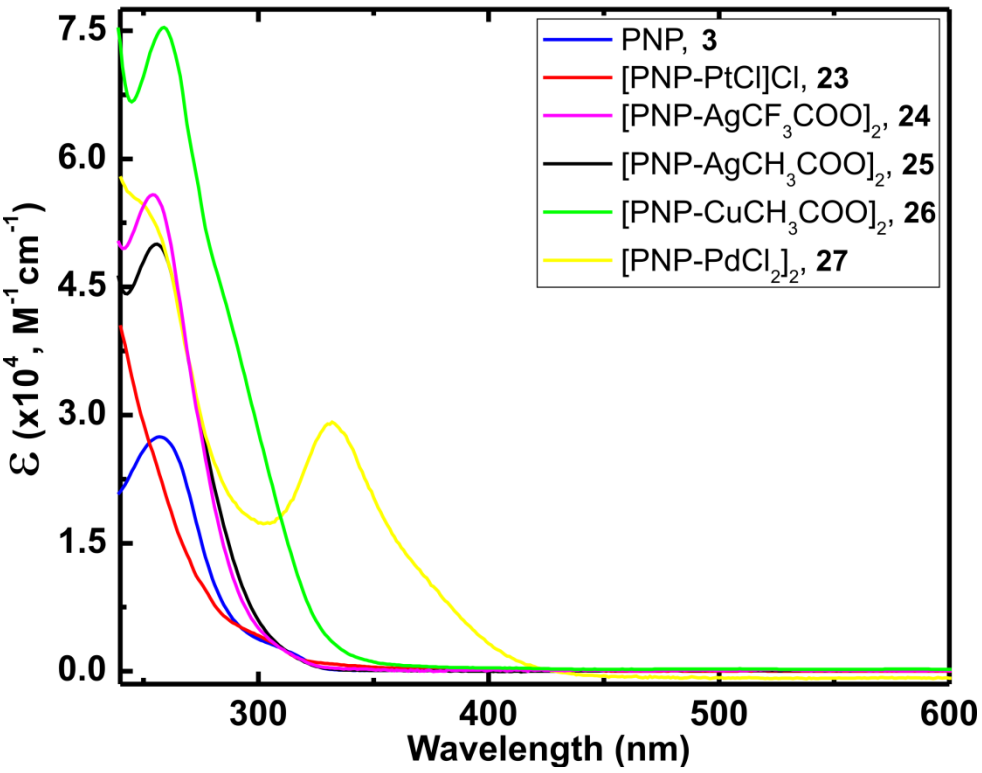

Figure 54. Absorption spectra of complexes **23**–**27**.

Luminescence measurements of complexes **23**–**27** and the ligand **3** were obtained. No ^{3}MLCT phosphorescence was observed; in addition, emission spectra of the complexes were similar to that of the free ligand. First, room temperature measurements were performed (**Figure 55**), and then samples were cooled to 77 K (**Figure 56**). The emission spectrum of ligand **3** showed two peaks. The first one is around ~300 nm, which is the ligand fluorescence due to π–π^* transition; the second peak is around 400 nm. The emission of the complexes coincides with either or both of those peaks. There are three possible causes for the formation of this peak in the ligand emission spectrum: charge transfer, excimer formation, and ligand phosphorescence. Because the concentrations of samples are in the range of 0.05 – 0.1 absorbance units, excimer formation is the least likely to occur. Excitation and emission spectra of **3** was obtained in EEET (ethyl

iodide/ether/ethanol/toluene, 2:2:1:1) solution to see if there was any change. The purpose of using EEET is that iodine, which is a heavy element, enhances any phosphorescence emission that occurs. Unfortunately, no change was observed. In order to see if the emission around 400 nm is caused by a charge transfer coming from the ligand, the emission spectra of the free ligand were taken in different solvents (different polarity); in other words, solvatochromism measurement was done. The solvents used were: CH_2Cl_2, DMF, 2-MeTHF, EtOH and isobutanol. The peak maxima of the ligand emission varied with the changing solvent polarity, i.e. positive solvatochromism was observed (**Figure 58**). This proves that the peak around ~ 400 nm results from a charge transfer (ILCT). There are differences of a few nanometers among peak maxima of the complexes. The reason for this variation could be the conformational differences upon complexation.

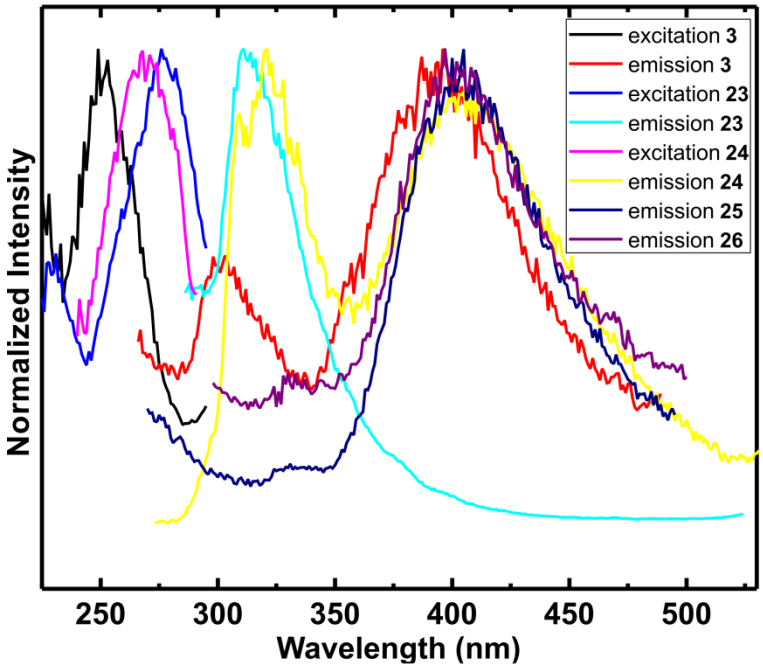

Figure 55. Excitation and emission spectra of ligand and metal complexes at RT.

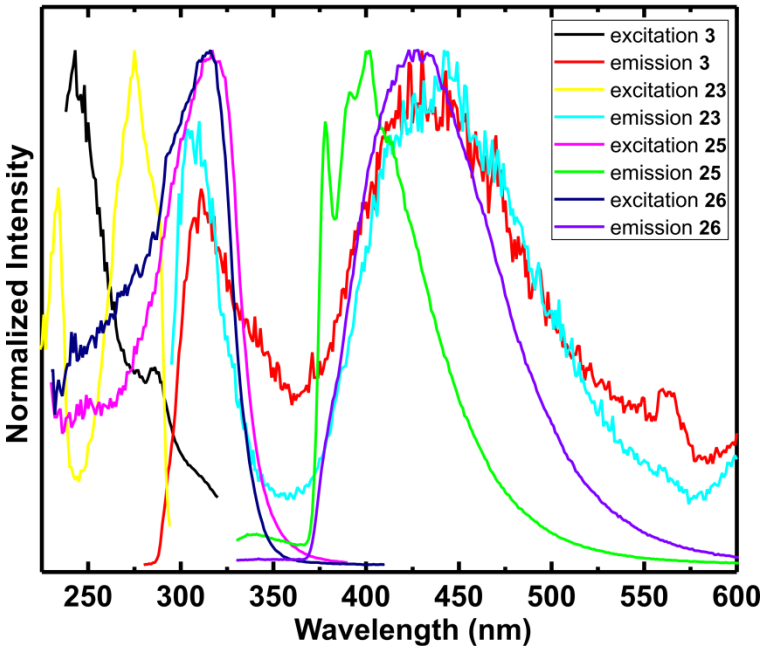

Figure 56. Excitation and emission spectra of ligand and metal complexes at 77 K.

Solid samples of complexes **23**–**26** were tested with a simple UV lamp for any phosphorescence. Unfortunately, no phosphorescence was observed. Solid state fluorescence spectra of **25** and **26** were also measured. Spectra of **25** did not show any peak; however, spectra of **26** resulted in ligand phosphorescence (**Figure 57**).

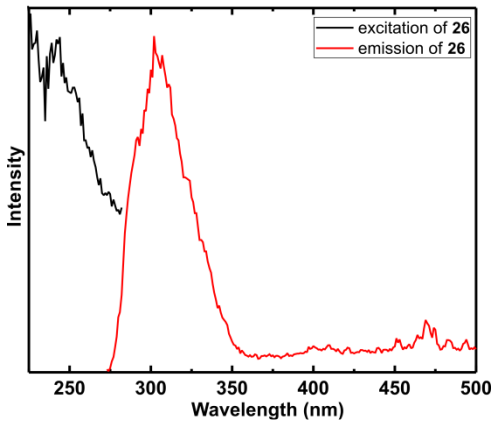

Figure 57. Solid state excitation and emission spectra of **26**.

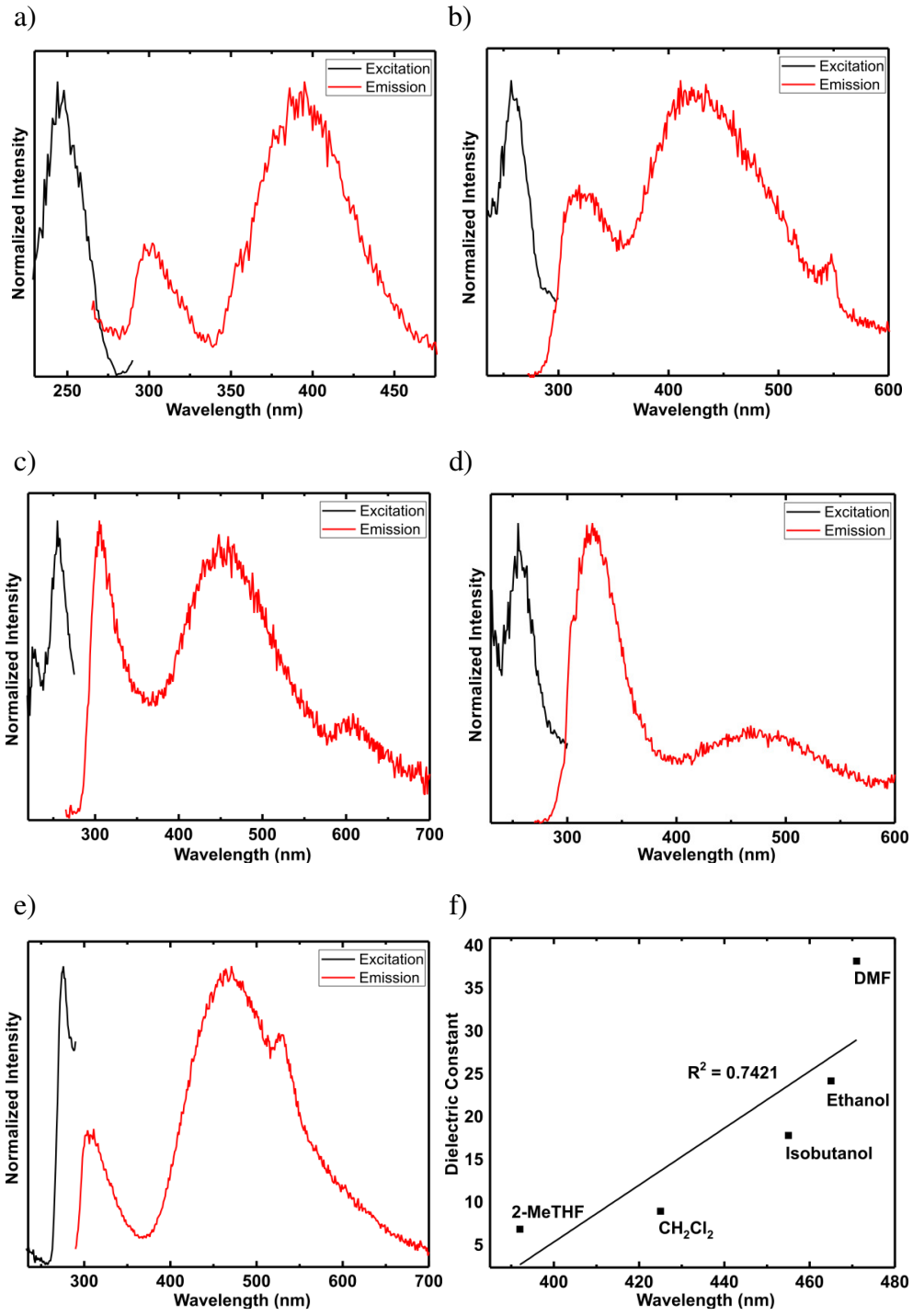

Figure 58. Excitation and emission spectra of ligand **3** in different solvents at RT (a-e). f) dielectric constant of the solvent vs wavelength of emission.

CONCLUSIONS

In summary, we report the synthesis, characterization, and fluorescence spectra of novel PNP complexes of copper, silver, palladium, and platinum. Ligand fluorescence was observed in all complexes around 300 nm due to π–π* transition. The peak around 400 nm, however, is caused by a charge transfer from the ligand, as proved by the positive solvatochromism experiment. Neither ^{3}MLCT nor ^{3}LC phosphorescence was observed in the luminescence measurements of the complexes. $^{31}P\{^{1}H\}$ NMR spectra of **24** and **25** are different at RT, showing that the counter anion has an effect on the strength of Ag–P bond.

The complexes have different coordination modes, i.e. bidentate monomeric (**22**), tridentate monomeric (**23**), bidentate dimeric with bridge (**24**–**26**), and bidentate dimeric (**27**). In all of the structures, the coordination number around the metal center is four, with either distorted tetrahedral or distorted square planar geometry; the only exception is **22**, with trigonal planar geometry involving a C=C (η^2) bond.

Future studies may focus on modification of the ligand and synthesis of corresponding complexes to obtain phosphorescence emission for photovoltaic and OLED applications; as well as synthesis of complexes with different coordination modes or preparation of heterobinuclear complexes.

Appendix A: SNS Ligands

The following SNS ligands (**41-44**) were synthesized and characterized by ^{1}H NMR and X-ray crystallography.

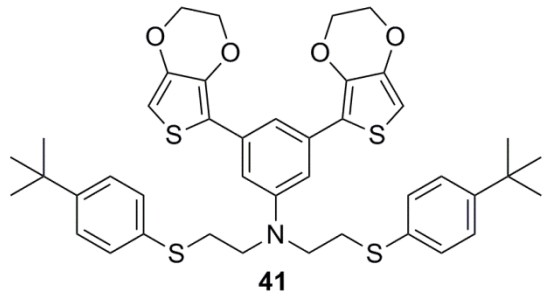

41

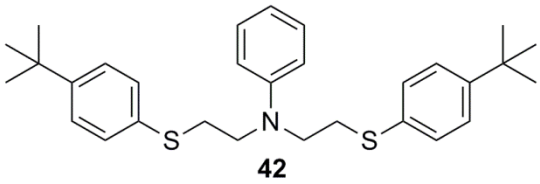

42

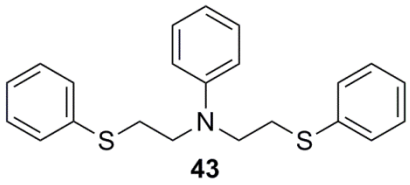

43

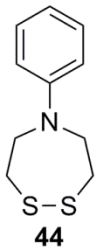

44

Figure A1. SNS ligands synthesized.

Syntheses

3,5-bis-EDOT-N,N-bis-[4-*tert*buthylthiophenylethyl]-aniline [41]. 4-tertbuthylthiophenol (0.02396 g) was dissolved in dry THF (~25 ml) and then cooled down to 0°C. NaH (0.0035 g) powder was added into the solution in small portions under Ar. Gas evolution was observed. The mixture was stirred under Ar for 1hr, then 3,5-bis-EDOT-N,N-bis-[2-chloroethyl]-aniline (0.0342 g) was dissolved by THF (~15 ml) in a vial and this solution was cannula transferred into the salt mixture. The reaction mixture was stirred at RT for overnight under Ar. The solvent was evaporated. The residue was extracted in between CH_2Cl_2 and H_2O. The organic phase was dried over $MgSO_4$, vacuum filtered, filtrate was evaporated. The residue was purified by a silica gel column in which the eluent was Hexanes:4/CH_2Cl_2:1. The yield was 65%. ^{1}H NMR (300 MHz, CD_2Cl_2): δ = 7.375 (s, 1H), 7.318 (s, 8H from thiophenol part), 6.943 (s, 2H, aromatic EDOT part), 4.241 (combined singlet, 8H, aliphatic EDOT part), 3.598 (t, *J* = 7.2 Hz, 4H), 3.142 (t, *J* = 7.2 Hz, 4H), 1.295 (s, 18H, tertbuthyl groups). ^{13}C{^{1}H} NMR (75 MHz, CD_2Cl_2): δ = 149.915, 147.381, 142.715, 138.724, 134.653, 132.589, 129.663, 126.478, 117.874, 113.139, 109.168, 97.646, 65.229, 64.954, 51.946, 34.702, 31.375, 30.052. LRMS (CI/CH_4): calculated for $C_{42}H_{47}NO_4S_4$ as 758.079, found as 759.

N,N-bis-[4-*tert*buthylthiophenylethyl]-aniline [42]. 4-*tert*buthylthiophenol (1.906 g, 11.5 mmol) was dissolved in dry THF (~ 25 ml). NaH (0.275g, 11.5 mmol) powder was added into the solution in small portions under Ar. Gas evolution was observed. After all NaH has been added, the reaction mixture was refluxed for 1 hr. Then the mixture was cooled down little bit. A solution of N,N-bis-[2-chloroethyl]aniline (1g, 4.58 mmol) in dry THF was added into the hot solution via a cannula and the mixture was refluxed for overnight. The solvent was evaporated. The residue was dissolved CH_2Cl_2 and extracted between CH_2Cl_2 and H_2O. The organic phase was dried over $MgSO_4$,

vacuum filtered, and the filtrate was evaporated. The residue was purified by a silica gel column in which the eluent was Hexanes:4/CH_2Cl_2:1. The yield was 95.53 %.

N,N-bis-[ethylphenylthioether]-aniline [43]. Thiophenol (0.2553 g, 2.317 mmol) was dissolved in dry THF (~25 ml). NaH (0.0585 g, 2.317 mmol) powder was added into the solution in small portions under Ar. Gas evolution was observed. After all NaH has been added, the reaction mixture was refluxed for 1 hr. Then the mixture was cooled down little bit. A solution of N,N-bis[2-(p-tolylsulfonyl)ethyl]aniline (0.4187 g, 0.855 mmol) (0.4187g, 0.855 mmol) in dry THF was added into the hot solution via a cannula and the mixture was refluxed for overnight. The solvent was evaporated. The residue was dissolved CH_2Cl_2 and extracted between CH_2Cl_2 and H_2O. The organic phase was dried over $MgSO_4$, vacuum filtered, and the filtrate was evaporated to afford a white solid in quantitative yields.

N,N-bis-[2-mercaptoethyl]-aniline [44]. $NaSH.H_2O$ (1.08 g, 14.78 mmol) was stirred in Ethanol under positive pressure of Ar for 1 hr. N,N-bis-[2-chloroethyl]aniline (0.5124 g, 2.35 mmol) was dissolved in ethanol under Ar and then transferred into $NaSH.H_2O$. The reaction mixture was refluxed for 24 hrs. Half of the solvent was pulled under Schlenk line and then degassed CH_2Cl_2 and degassed H_2O were added to extract the product under Ar. The organic phase was cannula transferred into a flask (with $MgSO_4$ in it) connected to the Schlenk line then it was cannula filtered into another flask and dried under vacuum to obtain the product with 83 % yield.

Crystal structures of SNS Ligands 42-44

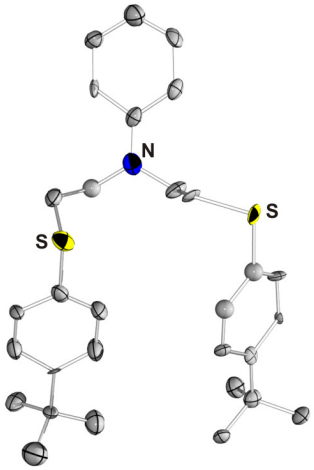

Figure A2. Structure of **42** showing the labeling of selected atoms. Hydrogen atoms have been omitted for clarity. Displacement ellipsoids are scaled to the 50% probability level.

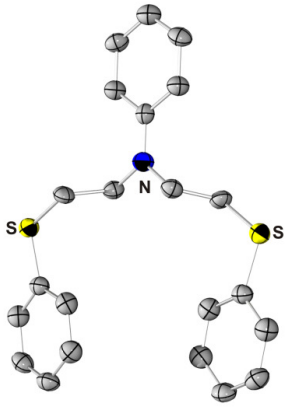

Figure A3. Structure of **43** showing the labeling of selected atoms. Hydrogen atoms have been omitted for clarity. Displacement ellipsoids are scaled to the 50% probability level.

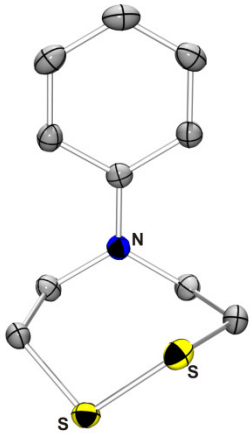

Figure A4. Structure of **44** showing the labeling of selected atoms. Hydrogen atoms have been omitted for clarity. Displacement ellipsoids are scaled to the 50% probability level.

Appendix B: Acknowledgements for the Measurements

X-ray crystallography data were acquired by a certain graduate student assigned by Prof. Bradley J. Holliday for the task of collecting all X-ray data for the entire research group, until they graduate. Then a new student takes the task. I grew all my own crystals; however, others loaded the crystals to the diffractometer and acquired the data. All XPS data were obtained by Mr. Travis Hesterberg after I prepared the samples.

Raman spectroscopy measurements in "Spectroscopy" section, page 31 was done by Ms. Sarah Stranahan in Willets research group.

"X-ray Crystal Structure Analysis" section, page 32 was done by Ms. Michelle Mejia and Ms. Julie Wilkerson.

The discussion on pages 43-48 "Structure of the Complexes" section were written by Seyma Keskin by using the data that Ms.Michelle Mejia and Ms. Julie Wilkerson acquired as a cif file.

All other characterizations and measurements were done by Seyma Keskin, i.e., ^{1}H NMR, ^{13}C NMR, ^{31}P NMR, IR (ATR-solid state and between KBr discs in solution state), UV-VIS spectroscopic measurements, fluorescence and phosphorescence measurements and calculations, electrochemistry, electropolymerizations, scan rate dependances and melting points of the compounds.

Figure 18, page 43: Raman spectra were acquired by Ms. Sarah Stranahan, ATR-IR spectra were acquired by Seyma Keskin.

Table 1, page 45: This data was acquired by Ms. Michelle Mejia (and later corrected by Ms. Julie Wilkerson).

Figure 19, page 49: This structure was generated from data that was acquired by Ms. Michelle Mejia (and later corrected by Ms. Julie Wilkerson).

Figure 20, page 50: This structure was generated from data that was acquired by Ms. Michelle Mejia (and later corrected by Ms. Julie Wilkerson).

Figure 21, page 51: This structure was generated from data that was acquired by Ms. Michelle Mejia (and later corrected by Ms. Julie Wilkerson).

Table 2, page 52: This table was generated by Seyma Keskin using the data acquired by Ms. Michelle Mejia and Ms. Julie Wilkerson.

Table 3, page 53: This table was generated by Seyma Keskin using the data acquired by Ms. Michelle Mejia and Ms. Julie Wilkerson.

Table 4, page 54: This table was generated by Seyma Keskin using the data acquired by Ms. Michelle Mejia and Ms. Julie Wilkerson.

Table 5, page 54: This table was generated by Seyma Keskin using the data acquired by Ms. Michelle Mejia and Ms. Julie Wilkerson.

Table 6, page 55: This table was generated by Seyma Keskin using the data acquired by Ms. Michelle Mejia and Ms. Julie Wilkerson.

Table 7, page 55: This table was generated by Seyma Keskin using the data acquired by Ms. Michelle Mejia and Ms. Julie Wilkerson.

Table 8, page 55: This table was generated by Seyma Keskin using the data acquired by Ms. Michelle Mejia and Ms. Julie Wilkerson.

"X-ray Crystal Structure Analysis" section, pages 65-66: This was done by Ms. Michelle Mejia (Ms. Julie Wilkerson corrected her data later).

"Structure of Complex **15**" section, pages 78-79: The section was written by Seyma Keskin using the data that Ms. Michelle Mejia acquired (Ms. Julie Wilkerson corrected her data later).

Table 11, page 79: This data was acquired by Ms. Michelle Mejia and then Julie Wilkerson has completed it.

Table 12, page 80: The table was generated by using data acquired by Ms. Michelle Mejia and Julie Wilkerson.

Figure 25, page 81: This structure was generated from data acquired by Ms. Michelle Mejia and Julie Wilkerson.

"Spectroscopic Properties of Polymers", page 89-90: Discussion is written by Seyma Keskin. Some part of it is based on specular reflectance IR measurements which were done by Nicholas Delone in Stevenson research group.

Figure 31, page 88: This data was acquired by Mr. Travis Hesterberg. Mr. Jeff McCarty taught me how to use the curve fitting analysis by using the computer program Casa-XPS. The curve-fittings were done by Seyma Keskin.

"X-ray Crystal Structure Analysis" section, pages 130-131: Ms. Michelle Mejia and Ms. Julie Wilkerson acquired data for complex **22**; Ms. Lauren Avery acquired data for complex **23**; Ms. Julie Wilkerson acquired data for complexes **24**-**26** and Ms. Julie Wilkerson and Ms. Lauren Avery acquired data for complex **27**.

"Crystal Structures of Complexes" section, pages 148-151: Discussion is based on the data acquired by Ms. Michelle Mejia, Ms. Julie Wilkerson and Ms. Lauren Avery.

Figure 50a, page 152: This structure was generated from data that was acquired by Ms. Michelle Mejia and Ms. Julie Wilkerson. Additionally, the structure was published in the literature as "Keskin, S. G.; Stanley, J. M.; Mejia, M. L.; Holliday, B. J., Acta Crystallographica Section E-Structure Reports Online 2011, 67, M1327-U248." This was referenced in the dissertation as reference #151.

Figure 50b, page 152: This structure was generated from data that was acquired by Ms. Lauren Avery.

Figure 51a, page 153: This structure was generated from data that was acquired by Ms. Julie Wilkerson.

Figure 51b, page 153: This structure was generated from data that was acquired by Ms. Julie Wilkerson.

Figure 52, page 154: These structures were generated from data that was acquired by Ms. Julie Wilkerson.

Figure 53, page 155: This structure was generated from data that was acquired by Ms. Julie Wilkerson and Ms. Lauren Avery.

Table 14, page 156: This data was acquired by Ms. Lauren Avery and Ms. Julie Wilkerson.

Table 15, page 157: This data was acquired by Ms. Julie Wilkerson.

Table 16, page 158: This data was acquired by Ms. Julie Wilkerson. Additionally, Me, Ms. Mejia, Ms. Wilkerson and Dr. Holliday published this structure as a literature article as "Keskin, S. G.; Stanley, J. M.; Mejia, M. L.; Holliday, B. J., Acta Crystallographica Section E-Structure Reports Online 2011, 67, M1327-U248." This was referenced in the dissertation as reference #151.

Table 17, page 158: This table was generated by using the data acquired by Ms. Lauren Avery.

Table 18, page 159: This table was generated by using the data acquired by Ms. Julie Wilkerson.

Table 19, page 160: This table was generated by using the data acquired by Ms. Julie Wilkerson.

Table 20, page 161: This table was generated by using the data acquired by Ms. Julie Wilkerson.

Table 21, page 162: This table was generated by using the data acquired by Ms. Julie Wilkerson.

Figure A2, page 172: This structure was generated from data acquired by Ms. Michelle Mejia.

Figure A3, page 172: This structure was generated from data acquired by Ms. Lauren Avery.

Figure A4, page 173: This structure was generated from data acquired by Ms. Michelle Mejia.

References

1. Chiang, C. K.; Fincher, C. R.; Park, Y. W.; Heeger, A. J.; Shirakawa, H.; Louis, E. J.; Gau, S. C.; Macdiarmid, A. G., *Physical Review Letters* **1977,** *39* (17), 1098-1101; Shirakawa, H.; Louis, E. J.; Macdiarmid, A. G.; Chiang, C. K.; Heeger, A. J., *Journal of the Chemical Society-Chemical Communications* **1977,** (16), 578-580.

2. Roncali, J., *Chemical Reviews* **1992,** *92*, 711-738.

3. Holliday, B. J.; Swager, T. M., *Chemical Communications* **2005,** (1), 23-36.

4. Wolf, M. O., *Journal of Inorganic and Organometallic Polymers and Materials* **2006,** *16* (3), 189-199.

5. Wolf, M. O., *Advanced Materials* **2001,** *13* (8), 545-553.

6. Skotheim, T. A.; Reynolds, J. R., *Handbook of Conducting Polymers*. 3rd ed.; CRC Press: Boka Raton, 2007; Vol. I.

7. Yamamoto, T.; Saitoh, Y.; Anzai, K.; Fukumoto, H.; Yasuda, T.; Fujiwara, Y.; Choi, B. K.; Kubota, K.; Miyamae, T., *Macromolecules* **2003,** *36* (18), 6722-6729.

8. Zhang, Y.; Xiong, Y.; Li, C.; Peng, J., *Chemistry Letters* **2008,** *37* (742 - 743).

9. Man, K. Y. K.; Wong, H. L.; Chan, W. K.; Kwong, C. Y.; Djurisic, A. B., *Chemistry of Materials* **2004,** *16* (3), 365-367.

10. Jaffe, H. H.; Miller, A. L., *Journal of Chemical Education* **1966,** *43* (9), 469-&.

11. Kasha, M., *Discussions of the Faraday Society* **1950,** *9*, 14 - 19.

12. Evans, R. C.; Douglas, P.; Winscom, C. J., *Coordination Chemistry Reviews* **2006,** *250* (15-16), 2093-2126.

13. Crosby, G. A., *Accounts of Chemical Research* **1975,** *8* (7), 231-238.

14. Yam, V. W. W., *Accounts of Chemical Research* **2002,** *35* (7), 555-563.

15. Holonyak, N. J., Lemelson-MIT Prize Winner. 2004.

16. Tang, C. W.; Vanslyke, S. A., *Applied Physics Letters* **1987,** *51* (12), 913-915.

17. Gustafsson, G.; Cao, Y.; Treacy, G. M.; Klavetter, F.; Colaneri, N.; Heeger, A. J., *Nature* **1992,** *357* (6378), 477-479.

18. Mikami, A.; Nishita, Y.; Iida, Y., High Efficiency Phosphorescent Organic Light-Emitting Devices Coupled with Lateral Color-Conversion Layer. In *SID Symposium Digest of Technical Papers*, 2006; Vol. 37, pp 1376-1379.

19. Sun, C. Lewis-acidic Triarylboranes: Optoelectronic Applications and Unusual Reactivities. Queen's University, Kingston, Ontario, Canada, 2012.

20. Tang, C. W., *Applied Physics Letters* **1986,** *48* (2), 183-185.

21. Kraft, A.; Grimsdale, A. C.; Holmes, A. B., *Angewandte Chemie-International Edition* **1998,** *37* (4), 402-428.

22. Shirota, Y.; Kageyama, H., *Chemical Reviews* **2007,** *107* (4), 953-1010.

23. Babel, A.; Jenekhe, S. A., *Journal of the American Chemical Society* **2003,** *125* (45), 13656-13657.

24. Entwistle, C. D.; Marder, T. B., *Chemistry of Materials* **2004,** *16* (23), 4574-4585.

25. Burroughes, J. H.; Bradley, D. D. C.; Brown, A. R.; Marks, R. N.; Mackay, K.; Friend, R. H.; Burns, P. L.; Holmes, A. B., *Nature* **1990,** *347* (6293), 539-541.

26. Forster, T., *Discussions of the Farada Society* **1959,** *27*, 7 - 17.

27. Dexter, D. L., *Journal of chemical Physics* **1953,** *21*, 836 - 850.

28. Baldo, M. A.; Thompson, M. E.; Forrest, S. R., *Pure and Applied Chemistry* **1999,** *71* (11), 2095-2106.

29. Kalinowski, J.; Fattori, V.; Cocchi, M.; Williams, J. A. G., *Coordination Chemistry Reviews* **2011,** *255* (21-22), 2401-2425.

30. Adachi, C.; Baldo, M. A.; Thompson, M. E.; Forrest, S. R., *Journal of Applied Physics* **2001,** *90* (10), 5048-5051.

31. Greenham, N. C.; Friend, R. H.; Bradley, D. D. C., *Advanced Materials* **1994,** *6* (6), 491-494.

32. Smith, R. C.; Tennyson, A. G.; Won, A. C.; Lippard, S. J., *Inorganic Chemistry* **2006,** *45* (23), 9367-9373.

33. Zhu, S. S.; Carroll, P. J.; Swager, T. M., *Journal of the American Chemical Society* **1996,** *118* (36), 8713-8714.

34. Shioya, T.; Swager, T. M., *Chemical Communications* **2002,** (13), 1364-1365.

35. Holliday, B. J.; Stanford, T. B.; Swager, T. M., *Chemistry of Materials* **2006,** *18* (24), 5649-5651.

36. Edelman, K. R.; Stevenson, K. J.; Holliday, B. J., *Macromolecular Rapid Communications* **2012,** *33* (6-7), 610-615.

37. Kingsborough, R. P.; Swager, T. M., *Chemistry of Materials* **2000,** *12* (4), 872-+.

38. Kostas, I. D., *Journal of Organometallic Chemistry* **2001,** *626* (1-2), 221-226.

39. Singleton, J. T., *Tetrahedron* **2003,** *59* (11), 1837-1857.

40. Zhao, C. Q.; Jennings, M. C.; Puddephatt, R. J., *Dalton Transactions* **2008,** (9), 1243-1250.

41. Adeloye, A. O.; Olomola, T. O.; Adebayo, A. I.; Ajibade, P. A., *International Journal of Molecular Sciences* **2012,** *13* (3), 3511-3526.

42. Berces, A., *Inorganic Chemistry* **1997,** *36* (21), 4831-4837.

43. Pellei, M.; Papini, G.; Lobbia, G. G.; Santini, C., *Current Bioactive Compounds* **2009,** *5*, 321 - 352.

44. Lee, S. J.; Jung, J. H.; Seo, J.; Yoon, I.; Park, K. M.; Lindoy, L. F.; Lee, S. S., *Organic Letters* **2006,** *8* (8), 1641-1643.

45. Milum, K. M.; Kim, Y. N.; Holliday, B. J., *Chemistry of Materials* **2010,** *22* (8), 2414-2416.

46. Aguila, D.; Escribano, E.; Speed, S.; Talancon, D.; Yerman, L.; Alvarez, S., *Dalton Transactions* **2009,** (33), 6610-6625.

47. Trofimenko, S., *Journal of the American Chemical Society* **1966,** *88* (8), 1842 - 1844.

48. Moulton, C. J.; Shaw, B. L., *Journal of the Chemical Society-Dalton Transactions* **1976,** (11), 1020-1024.

49. Albrecht, M.; Lindner, M. M., *Dalton Transactions* **2011,** *40* (35), 8733-8744.

50. Wolf, M. O.; Zhu, Y. B., *Advanced Materials* **2000,** *12* (8), 599-601.

51. Zhu, S. S.; Swager, T. M., *Advanced Materials* **1996,** *8* (6), 497-&; Zhu, S. S.; Kingsborough, R. P.; Swager, T. M., *Journal of Materials Chemistry* **1999,** *9* (9), 2123-2131.

52. Reddinger, J. L.; Reynolds, J. R., *Chemistry of Materials* **1998,** *10* (1), 3-5.

53. Juris, A.; Balzani, V.; Barigelletti, F.; Campagna, S.; Belser, P.; Von Zelewsky, A., *Coordination Chemistry Reviews* **1988,** *84*, 85 - 277.

54. Campagna, S.; Puntoriero, F.; Nastasi, F.; Bergamini, G.; Balzani, V., *Photochemistry and Photophysics of Coordination Compounds I* **2007,** *280*, 117-214.

55. Wong, C. T.; Chan, W. K., *Advanced Materials* **1999,** *11* (6), 455-+.

56. Chan, W. K., *Coordination Chemistry Reviews* **2007,** *251* (17-20), 2104-2118; Knapp, R.; Schott, A.; Rehahn, M., *Macromolecules* **1996,** *29* (1), 478-480; Kelch, S.; Rehahn, M., *Macromolecules* **1997,** *30* (20), 6185-6193.

57. Ng, P. K.; Gong, X.; Chan, S. H.; Lam, L. S. M.; Chan, W. K., *Chemistry-a European Journal* **2001,** *7* (20), 4358-4367.

58. Fernandeztrujillo, M. J.; Basallote, M. G.; Valerga, P.; Puerta, M. C.; Hughes, D. L., *Journal of the Chemical Society-Dalton Transactions* **1991,** (11), 3149-3151.

59. Mendel, R. R.; Bittner, F., *Biochimica Et Biophysica Acta-Molecular Cell Research* **2006,** *1763* (7), 621-635.

60. Enemark, J. H.; Cooney, J. J. A., *Chemical Reviews* **2004,** *104* (2), 1175-1200.

61. Maji, P.; Wang, W.; Greene, A. E.; Gimbert, Y., *Journal of Organometallic Chemistry* **2008,** *693* (10), 1841-1849.

62. Hii, K. K. M.; Thornton-Pett, M.; Jutand, A.; Tooze, R. P., *Organometallics* **1999,** *18* (10), 1887-1896.

63. Siclovan, O. P.; Angelici, R. J., *Inorganic Chemistry* **1998,** *37* (3), 432-444.

64. Hessler, A.; Kucken, S.; Stelzer, O.; Sheldrick, W. S., *Journal of Organometallic Chemistry* **1998,** *553* (1-2), 39-52.

65. Ballester, N. M. S.; Elsegood, M. R. J.; Smith, M. B.; Brown, G. M., *Acta Crystallographica Section E-Structure Reports Online* **2007,** *63*, m719-m721.

66. Mayer, H. A.; Kaska, W. C., *Chemical Reviews* **1994,** *94* (5), 1239-1272.

67. Michos, D.; Luo, X. L.; Crabtree, R. H., *Journal of the Chemical Society-Dalton Transactions* **1992,** (10), 1735-1738.

68. Higashi, T., ABSCOR. Rigaku Corporation: Tokyo, Japan., 2001.

69. Otwinowski, Z.; Minor, W., DENZO-SMN. (1997). Processing of X-ray Diffraction Data Collected in Oscillation Mode. In *Methods in Enzymology*, Carter, C. W. J.; Sweets, R. M., Eds. Academic Press: Vol. 276, pp 307 – 326.

70. Altomare, A.; Burla, M. C.; Camalli, M.; Cascarano, G. L.; Giacovazzo, C.; Guagliardi, A.; Moliterni, A. G. G.; Polidori, G.; Spagna, R., *Journal of Applied Crystallography* **1999,** *32*, 115 - 119.

71. Sheldrick, G. M. *SHELX 97, A software package for the solution and refinement of X-ray data*, University of Göttingen: Göttingen, Germany, 1997.

72. Cromer, D. T.; Waber, J. T., International Tables for X-Ray Crystallography. Kynoch Press: Birmingham, 1992.

73. Shi, Y. L.; Gao, Y. C.; Shi, Q. Z.; Kershner, D. L.; Basolo, F., *Organometallics* **1987,** *6* (7), 1528-1531.

74. Blower, P. J.; Jeffery, J. C.; Miller, J. R.; Salek, S. N.; Schmaljohann, D.; Smith, R. J.; Went, M. J., *Inorganic Chemistry* **1997,** *36* (8), 1578-1582.

75. Ainscough, E. W.; Brodie, A. M.; Buckley, P. D.; Burrell, A. K.; Kennedy, S. M. F.; Waters, J. M., *Journal of the Chemical Society-Dalton Transactions* **2000,** (16), 2663-2671.

76. Crabtree, R. H., *The Organometallic Chemistry of the Transition Metals*. 3 rd ed.; John Wiley and Sons: USA, 2001.

77. Cotton, F. A.; Wilkinson, G., *Advanced Inorganic Chemistry*. 5th ed.; WILEY: New York, 1988.

78. Manners, I., *Synthetic Metal-Containing Polymers*. Wiley-VCH: Weinheim, 2004.

79. Miller, T. M.; Ahmed, K. J.; Wrighton, M. S., *Inorganic Chemistry* **1989,** *28*, 2347 - 2355.

80. Poverenov, E.; Gandelman, M.; Shimon, L. J. W.; Rozenberg, H.; Ben-David, Y.; Milstein, D., *Organometallics* **2005,** *24* (6), 1082-1090.

81. Wolf, M. O.; Wrighton, M. S., *Chemistry of Materials* **1994,** *6* (9), 1526-1533.

82. Weinberger, D. A.; Higgins, T. B.; Mirkin, C. A.; Stern, C. L.; Liable-Sands, L. M.; Rheingold, A. L., *Journal of the American Chemical Society* **2001,** *123* (11), 2503-2516.

83. Angell, S. E.; Rogers, C. W.; Zhang, Y.; Wolf, M. O.; Jones, W. E., *Coordination Chemistry Reviews* **2006,** *250* (13-14), 1829-1841.

84. Allgeier, A. M.; Mirkin, C. A., *Angewandte Chemie-International Edition* **1998,** *37* (7), 894-908.

85. Khramov, D. M.; Rosen, E. L.; Lynch, V. M.; Bielawski, C. W., *Angewandte Chemie-International Edition* **2008,** *47* (12), 2267-2270.

86. Weinberger, D. A.; Higgins, T. B.; Mirkin, C. A.; Liable-Sands, L. M.; Rheingold, A. L., *Angewandte Chemie-International Edition* **1999,** *38* (17), 2565-2568; Higgins, T. B.; Mirkin, C. A., *Chemistry of Materials* **1998,** *10* (6), 1589-1595.

87. Boruah, J. J.; Kalita, D.; Das, S. P.; Paul, S.; Islam, N. S., *Inorganic Chemistry* **2011,** *50* (17), 8046-8062.

88. Moreno, J.; Iglesias, J.; Meleroa, J. A.; Sherringtonc, D. C., *Journal of Materials Chemistry* **2011,** *21*, 6725 - 6735.

89. Maurya, M. R.; Kumar, M.; Kumar, U., *Journal of Molecular Catalysis a-Chemical* **2007,** *273* (1-2), 133-143.

90. Dolman, S. J.; Hultzsch, K. C.; Pezet, F.; Teng, X.; Hoveyda, A. H.; Schrock, R. R., *Journal of the American Chemical Society* **2004,** *126* (35), 10945-10953.

91. Shultz, G. V.; Zakharov, L. N.; Tyler, D. R., *Macromolecules* **2008,** *41* (15), 5555-5558.

92. Chelebaeva, E.; Larionova, J.; Guari, Y.; Ferreira, R. A. S.; Carlos, L. D.; Paz, F. A. A.; Trifonov, A.; Guerin, C., *Inorganic Chemistry* **2011,** *50*, 9924 - 9926.

93. Matsumoto, T.; Chang, H. C.; Kobayashi, A.; Uosaki, K.; Kato, M., *Inorganic Chemistry* **2011,** *50* (7), 2859-2869.

94. Zhang, J.; Meng, S.; Song, Y.; Zhou, Y.; Cao, Y.; Li, J.; Zhao, H.; Hu, J.; Wu, J.; Humphrey, M. G.; Zhang, C., *Crystal Growth and Design* **2011,** *11*, 100 - 109.

95. Das, B.; Srilatha, M.; Veeranjaneyulu, B.; Kanth, B. S., *Helvetica Chimica Acta* **2011,** *94* (885 - 891).

96. Kim, D. H.; Kang, B. S.; Lim, S. M.; Bark, K.; Kim, B. G.; Shiro, M.; Shim, Y.; Shin, S. C., *Journal of the Chemical Society, Dalton Transactions* **1998**, 1893 - 1898.

97. *CrystalClear 1.40*, Rigaku Americas Corporation: The Woodlands, TX, 2008.

98. Zhu, S. S.; Swager, T. M., *Journal of the American Chemical Society* **1997,** *119* (51), 12568-12577.

99. ten Brink, G. J.; Vis, J. M.; Arends, I.; Sheldon, R. A., *Tetrahedron* **2002,** *58* (20), 3977-3983.

100. Berube, M.; Poirier, D., *Organic Letters* **2004,** *6* (18), 3127-3130.

101. Ball, C. R.; Wade, R., *Journal of the Chemical Society C-Organic* **1968,** (11), 1338-&.

102. Kvarnstrom, C.; Neugebauer, H.; Blomquist, S.; Ahonen, H. J.; Kankare, J.; Ivaska, A., *Electrochimica Acta* **1999,** *44* (16), 2739-2750.

103. Zaban, A.; Zinigrad, E.; Aurbach, D., *Journal of Physical Chemistry* **1996,** *100* (8), 3089-3101.

104. Hilgers, F.; Bruns, W.; Fiedler, J.; Kaim, W., *Journal of Organometallic Chemistry* **1996,** *511* (1-2), 273-280.

105. Castaneda, S. I.; Montero, I.; Ripalda, J. M.; Diaz, N.; Galan, L.; Rueda, F., *Journal of Applied Physics* **1999,** *85* (12), 8415-8418.

106. Wang, P. G.; Cai, B. T.; Taniguchi, N., *Nitric Oxide Donors for Pharmaceutical and Biological Applications*. WILEY-VCH Verlag GmbH & Co KGaA: Weinheim, 2005.

107. Broomhead, J. A.; Young, C. G., *Inorganic Syntheses* **1990,** *28*, 338-340.

108. Brandt, W. W.; Smith, G. F., *Analytical Chemistry* **1949,** *21*.

109. Burstall, F. H., *Journal of the Chemical Society* **1936**, 173 - 175.

110. Montalti, M.; Cedi, A.; Prodi, L.; Gandolfi, M. T., *Handbook of Photochemistry*. 3rd ed.; CRC press Taylor & Francis Group.: 6000 Broken Sound Prkway NW, Suite 200 Boca Raton FL, 2006.

111. Tokeltak.Ne; Hemingwa.Re; Bard, A. J., *Journal of the American Chemical Society* **1973,** *95* (20), 6582-6589.

112. Saji, T.; Aoyagui, S., *Journal of Electroanalytical Chemistry* **1975,** *58* (2), 401-410; Vlcek, A. A., *Coordination Chemistry Review* **1982,** *43*, 39; Dearmond, M. K.; Carlin, C. M., *Coordination Chemistry Reviews* **1981,** *36* (3), 325-355.

113. Bard, A. J.; Fox, M. A., *Accounts of Chemical Research* **1995,** *28* (3), 141-145.

114. Hara, M.; Waraksa, C. C.; Lean, J. T.; Lewis, B. A.; Mallouk, T. E., *Journal of Physical Chemistrty* **2000,** *22* (A 104), 5275–5280.

115. Crosby, G. A., *Advances in Chemistry Series* **1976,** (150), 149-159; Kober, E. M.; Meyer, T. J., *Inorganic Chemistry* **1982,** *21* (11), 3967-3977; Mandal, K.; Pearson, T. D. L.; Krug, W. P.; Demas, J. N., *Journal of the American Chemican Society* **1983,** *105*, pp 701–707.

116. Watts, R. J., *Journal of Chemical Education* **1983,** *60* (10), 834-842; Kalyanasundaram, K., *Coordination Chemistry Reviews* **1982,** *46* (OCT), 159-244; Seddon, E. A.; Seddon, K. R., In *The Chemistry of Ruthenium*, EIsevier, Amsterdam, 1984.

117. Demas, J. N., *Journal of Chemical Education* **1983,** *60* (10), 803-808.

118. Fleischauer, P. D.; Fleischauer, P., *Chemical Reviews* **1970,** *70* (2), 199-&.

119. Zhu, X. J.; Holliday, B. J., *Macromolecular Rapid Communications* **2010,** *31* (9-10), 904-909.

120. Hjelm, J.; Handel, R. W.; Hagfeldt, A.; Constable, E. C.; Housecroft, C. E.; Forster, R. J., *Inorganic Chemistry* **2005,** *44* (4), 1073-1081; Araki, K.; Endo, H.; Masuda, G.; Ogawa, T., *Chemistry-a European Journal* **2004,** *10* (13), 3331-3340; Hjelm, J.; Constable, E. C.; Figgemeier, E.; Hagfeldt, A.; Handel, R.; Housecroft, C. E.; Mukhtar, E.; Schofield, E., *Chemical Communications* **2002,** (3), 284-285; Jousselme, B.; Blanchard, P.; Ocafrain, M.; Allain, M.; Levillain, E.; Roncali, J., *Journal of*

Materials Chemistry **2004,** *14* (3), 421-427; Cameron, C. G.; Pickup, P. G., *Chemical Communications* **1997,** (3), 303-304; Cameron, C. G.; Pickup, P. G., *Journal of the American Chemical Society* **1999,** *121* (33), 7710-7711; Cameron, C. G.; Pittman, T. J.; Pickup, P. G., *Journal of Physical Chemistry B* **2001,** *105* (37), 8838-8844; Cameron, C. G.; Pickup, P. G., *Journal of the American Chemical Society* **1999,** *121* (50), 11773-11779; MacLean, B. J.; Pickup, P. G., *Journal of Physical Chemistry B* **2002,** *106* (18), 4658-4662.

121. Peng, Z. H.; Yu, L. P., *Journal of the American Chemical Society* **1996,** *118* (15), 3777-3778; Peng, Z. H.; Gharavi, A. R.; Yu, L. P., *Journal of the American Chemical Society* **1997,** *119* (20), 4622-4632.

122. Stanley, J. M.; Zhu, X.; Yang, X.; Holliday, B. J., *Inorganic Chemistry* **2010,** *49* (5), 2035-2037.

123. Jameson, D. L.; Goldsby, K. A., *Journal of Organic Chemistry* **1990,** *55* (17), 4992-4994.

124. Zoppellaro, G.; Baumgarten, M., *European Journal of Organic Chemistry* **2005,** (14), 2888-2892.

125. Pavlishchuk, V. V.; Addison, A. W., *Inorganica Chimica Acta* **2000,** *298* (1), 97-102.

126. Nakaramu, K., *Bulletin of the Chemical Society of Japan* **1982,** *55*, 2697-2705.

127. Armaroli, N.; Decola, L.; Balzani, V.; Sauvage, J. P.; Dietrichbuchecker, C. O.; Kern, J. M., *Journal of the Chemical Society-Faraday Transactions* **1992,** *88* (4), 553-556.

128. Bartecki, A.; Szoke, J.; Varsanyi, G.; Vizesy, M., *Absorption spectra in the ultraviolet and visible region*. Academic Press Inc.: New York, 1961; Vol. 2.

129. Stanley, J. M.; Chan, C. K.; Yang, X.; Jones, R. A.; Holliday, B. J., *Polyhedron* **2010,** *29* (12), 2511-2515.

130. De Silva, C. R.; Wang, R. Y.; Zheng, Z. P., *Polyhedron* **2006,** *25* (17), 3449-3455.

131. Chen, X. Y.; Yang, X.; Holliday, B. J., *Journal of the American Chemical Society* **2008,** *130* (5), 1546-+.

132. Crosby, G. A.; Elfring, W. H., *Journal of Physical Chemistry* **1976,** *80* (20), 2206-2211.

133. Lytwak, L. A.; Stanley, J. M.; Mejia, M. L.; Holliday, B. J., *Dalton Transactions* **2010,** *39* (33), 7692-7699.

134. Rusak, D. A.; James, W. H.; Ferzola, M. J.; Stefanski, M. J., *Journal of Chemical Education* **2006,** *83* (12), 1857-1859.

135. Kretschmer, C. B.; Nowakowska, J.; Wiebe, R., *Industrial and Engineering Chemistry* **1946,** *38* (5), 506 - 509.

136. Farley, S. J.; Rochester, D. L.; Thompson, A. L.; Howard, J. A. K.; Williams, J. A. G., *Inorganic Chemistry* **2005,** *44* (26), 9690-9703.

137. Sacconi, L.; Morassi, R., *Journal of the Chemical Society a -Inorganic Physical Theoretical* **1968,** (12), 2997-&; Morassi, R.; Sacconi, L., *Journal of the Chemical Society a -Inorganic Physical Theoretical* **1971,** (3), 492-&.

138. Garcia-Seijo, M. I.; Habtemariam, A.; Fernandez-Anca, D.; Parsons, S.; Garcia-Fernandez, M. E., *Zeitschrift Fur Anorganische Und Allgemeine Chemie* **2002,** *628* (5), 1075-1084; Janosi, L.; Kegl, T.; Hajba, L.; Berente, Z.; Kollar, L., *Inorganica Chimica Acta* **2001,** *316* (1-2), 135-139; Khan, M. M. T.; Paul, P.; Venkatasubramanian, K.; Purohit, S., *Inorganica Chimica Acta* **1991,** *183* (2), 229-237.

139. Muller, T. E.; Berger, M.; Grosche, M.; Herdtweck, E.; Schmidtchen, F. P., *Organometallics* **2001,** *20* (21), 4384-4393.

140. Liang, L. C., *Coordination Chemistry Reviews* **2006,** *250* (9-10), 1152-1177.

141. Zhang, J.-F.; Fu, W.-F.; Ganb, X.; Chenb, J.-H., *Dalton Transactions* **2008**, 3093–3100.

142. Yam, V. W. W.; Fung, W. K. M.; Wong, M. T., *Organometallics* **1997,** *16* (8), 1772-1778.

143. Harkins, S. B.; Peters, J. C., *Journal of the American Chemical Society* **2005,** *127* (7), 2030-2031.

144. Catalano, V. J.; Kar, H. M.; Bennett, B. L., *Inorganic Chemistry* **2000,** *39* (1), 121-127.

145. Jin, Q.-H.; Cui, L.-N.; Li, Z.-F.; Jiang, Y.-H.; Wu, M.-H.; Gao, S.; Zhang, C.-L., *Polyhedron* **2012**, 472 - 477.

146. Kato, M., *Bulletin of the Chemical Society of Japan* **2007,** *80* (2), 287-294.

147. Ramamurthy, V.; Schanze, K. Z., *Multimetallic and Macromolecular Inorganic Photochemistry*. M Dekker: New York, 1999.

148. Yam, V. W.-W.; Lo, K. K.-W.; Fung, W. K.-M.; Wang, C.-R., *Coordination Chemistry Reviews* **1998,** *171*, 17 - 41.

149. Ajjou, A. N.; Alper, H., *Journal of the American Chemical Society* **1998,** *120* (7), 1466-1468; Bianchini, C.; Farnetti, E.; Glendenning, L.; Graziani, M.; Nardin, G.; Peruzzini, M.; Rocchini, E.; Zanobini, F., *Organometallics* **1995,** *14* (3), 1489-1502; Nuzzo, R. G.; Haynie, S. L.; Wilson, M. E.; Whitesides, G. M., *Journal of Organic Chemistry* **1981,** *46* (14), 2861-2867.

150. *Inorganic Syntheses*. 1984; Vol. 26, p 345 - 346; *Inorganic Syntheses*. 1990; Vol. 28, p 60 - 63.

151. Keskin, S. G.; Stanley, J. M.; Mejia, M. L.; Holliday, B. J., *Acta Crystallographica Section E-Structure Reports Online* **2011,** *67*, M1327-U248.

152. Effendy; Nicola, C. D.; Fianchini, M.; Pettinari, C. S., Brian W.; Somers, N.; White, A. H., *Inorganica Chimica Acta* **2005,** *358*, 763 - 795.

153. Retboll, M. K.; Wenger, E.; Willis, A. C., *Acta Crystallographica Section E-Structure Reports Online* **2002,** *58*, M275-M277.

154. Goddard, R.; Hopp, G.; Jolly, P. W.; Kruger, C.; Mynott, R.; Wirtz, C., *Journal of Organometallic Chemistry* **1995,** *486* (1-2), 163-170.

155. Liang, L. C.; Lin, J. M.; Lee, W. Y., *Chemical Communications* **2005,** (19), 2462-2464.

156. Di Nicola, C.; Effendy; Pettinari, C.; Skelton, B. W.; Somers, N.; White, A. H., *Inorganica Chimica Acta* **2005,** *358* (3), 695-706.

157. Bowmaker, G. A.; Effendy; Hanna, J. V.; Healy, P. C.; King, S. P.; Pettinari, C.; Skelton, B. W.; White, A. H., *Dalton Transactions* **2011,** *40* (27), 7210-7218.

Vita

Şeyma (*nee* Gören) Keskin was born in Kahramanmaraş, Turkey. She has earned her B.S. degree in Chemistry with honors from Boğazici University, İstanbul in 1999. She worked in a research laboratory a national chemical manufacturing plant in Istanbul until 2001. Then, she earned her M.S. degree with honors in Biomedical Engineering from the Institute of Biomedical Engineering, Boğazici University, İstanbul in 2003. She started the graduate program in Chemistry at UT Austin in 2007 and completed the work on her M.A. in 2013.

Permanent email address: seyma.keskin@gmail.com

This thesis was typed by Şeyma Keskin